Lamb wave based active damage identification in adhesively bonded composite lap joints

By

Prateek Jolly

A Thesis
Submitted to the Faculty of
Mississippi State University
in Partial Fulfillment of the Requirements
for the Degree of Master of Science
in Aerospace Engineering
in the Department of Aerospace Engineering

Mississippi State University, Mississippi

May 2016

Lamb wave based active damage identification in adhesively bonded composite lap joints

By

Prateek Jolly

Approved:

Ratneshwar Jha
(Major Professor)

Thomas E. Lacy
(Committee Member)

Rani W. Sullivan
(Committee Member)

J. Mark Janus
(Graduate Coordinator)

Jason M. Keith
Dean
Bagley College of Engineering

Name: Prateek Jolly

Date of Degree: May 6, 2016

Institution: Mississippi State University

Major Field: Aerospace Engineering

Major Professor: Ratneshwar Jha

Title of Study: Lamb wave based active damage identification in adhesively bonded composite lap joints

Pages in Study: 117

Candidate for Degree of Master of Science

Bonding composite structures using adhesives offers several advantages over mechanical fastening such as better flow stress, weight saving, improved fatigue resistance and the ability to join dissimilar structures. The hesitation to adopt adhesively bonded composite joints stems from the lack of knowledge regarding damage initiation and propagation mechanisms within the joint. A means of overcoming this hesitation is to continuously monitor damage in the joint. This study proposes a methodology to conduct structural health monitoring (SHM) of an adhesively bonded composite lap joint using acoustic, guided Lamb waves by detecting, locating and predicting the size of damage. Finite element modeling of a joint in both 2D and 3D is used to test the feasibility of the proposed damage triangulation technique. Experimental validation of the methodology is conducted by detecting the presence, location and size of inflicted damage with the use of tuned guided Lamb waves.

ACKNOWLEDGEMENTS

I would like to thank my research adviser, Dr. Ratneshwar Jha, for providing me the opportunity to conduct research at the Raspet Flight Research Laboratory in pursuit of my master’s degree. His profound knowledge, constant encouragement and infinite patience have successfully guided me through these two and a half years. I also gratefully acknowledge the advice and support I got from my committee chairs, Prof. Lacy and Prof. Sullivan. I am indebted to Prof. Newman, Prof. Gullett and Mr. Walker for providing me with an excellent education in aerospace structures here at Mississippi State.

I am grateful to my lab mates Ashkan Khalili and Nimesh Akalanka for their constant guidance, discussions and friendship. I would like to thank Matt Fox, Rodney Lincoln, Clay Shires, Jo McKenzie and Edward Skinner for the practical education and for supporting me during my time in Mississippi. Thank you all for making my experience at Raspet a wonderful one.

I wish to express my deep gratitude to Profs. Arya, Sudhakar and Prahlad for providing me with an education in aviation. They have been excellent mentors and have inspired me to continue my education in aerospace engineering. I am also grateful to my school teachers Mr. Browne, Mr. Hart, Mr. Meakin, Ms. Nirmala, Mrs. Cabral and Dr. Rao for inciting in me a passion to learn about all things that fly.

To Aamir, Anuraj, Rahul, Kalyan and Piyush I offer my sincerest thanks for being my badminton partners. I would especially like to thank Prof. Thu Dinh for his altruistic coaching and instilling in me both a love, and discipline for the game.

Hamed, Sanchit, Anay, Savera, Marina, Anurag, Randhika and Abhimanyu, thank you for making Starkville a home away from home. Neel, Saanand, Mihir, Sweta, Prashanth, Shwetha, Prasanna and Gaurav, thank you for keeping my memories of home fresh and alive.

Lastly, I would like to thank my parents Rajkanwar Jolly and Satinder Jolly, and my brother Angad Jolly for making me who I am today.

This thesis is dedicated to all of you.

TABLE OF CONTENTS

CHAPTER

APPENDIX

LIST OF TABLES

LIST OF FIGURES

CHAPTER I

INTRODUCTION AND BACKGROUND

The percentage of composite materials employed in aircraft structures has been steadily increasing over the last 40 years. From the U.S. Army's XV-11A, an all-fiberglass short takeoff and landing airplane developed at the Raspet flight research laboratory (RFRL) at Mississippi State University in the 1960's (Raspet, 2015) to the Airbus A350 XWB which will be constructed out of 53% advanced composites. Prior to the 1980s, commercial aircraft designers employed composite materials primarily in secondary structures. Airbus introduced the A320 in 1988 which was the first production commercial aircraft with an all-composite horizontal tail and flaps (Airbus, 2013). As seen in Fig. 1.1, the extension of composites to wing and fuselage structures has increased the percentage of advanced composites in modern aircraft designs to more than 50% (Red, 2014). The extensive application of composite materials to the design and manufacture of the A350-XWB contributes to an almost 25% reduction in fuel consumption (Airbus, 2015).

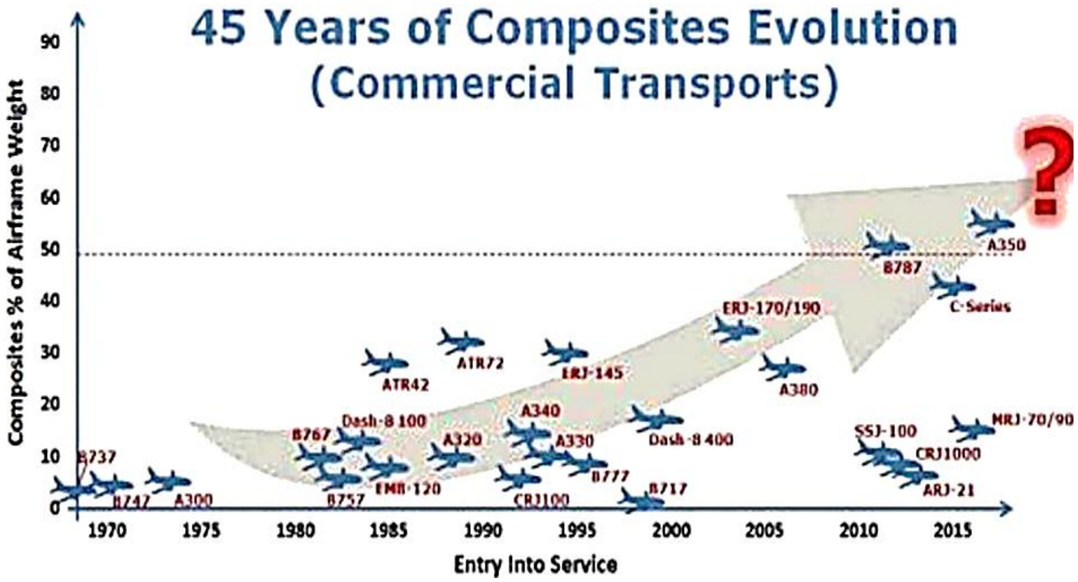

Figure 1.1 Steady increase in the use of advanced composites over the last three decades.

(Red, 2014)

The greatest advantage of using composite materials is their ability to be tailored to design requirements. The structure can be made stiffer in one direction and more flexible in another. This implies that the structure can be designed to be exactly as strong and stiff as it needs to be, leading to improved structural weight, aeroelasticity and ultimately fuel efficiency. The advantages of using composite materials over metals in aircraft go beyond just a reduction in fuel consumption. New applications and benefits of using advanced composites are being realized. For example, passengers travelling on-board the Boeing 787 are more comfortable because its composite fuselage is able to sustain higher cabin pressure and humidity levels. This is because of the increased corrosion and fatigue resistance of composite materials.

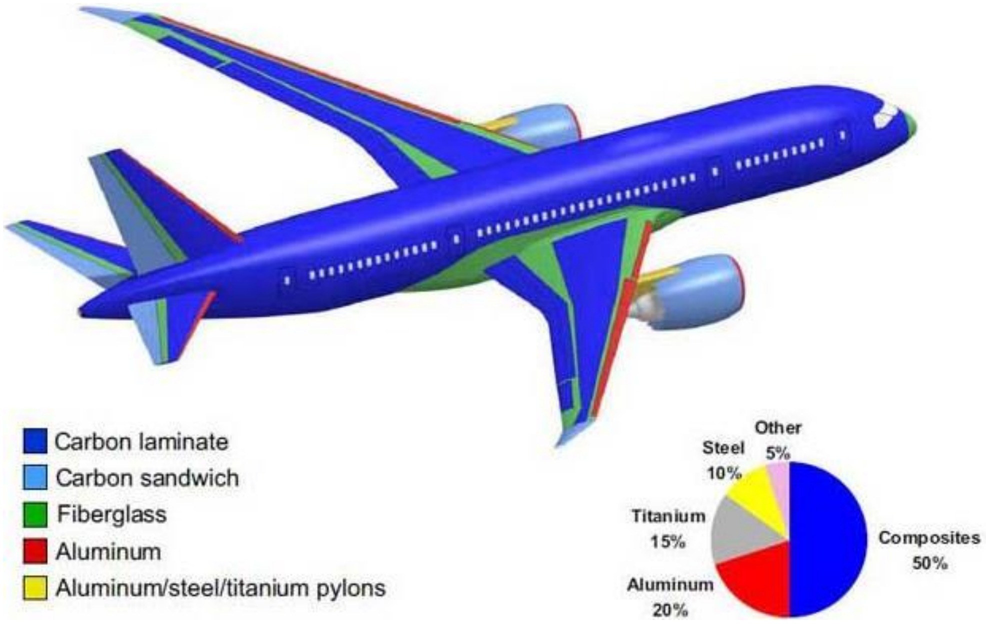

Figure 1.2 Material distribution on the Boeing 787.

About half the material used to create the aircraft is some form of an advanced composite. (Freissinet, 2011)

The use of composite materials has its downsides as well. One of the greatest disadvantages of using composite materials is the difficulty in characterizing damage. During the certification stage of the Boeing 787, the Government Accountability Office published a report that encapsulated their safety concerns in four major points (GAO, 2011).

- The limited knowledge and database on the behavior of composite structures. This concern was also partially due to the lack of experience of in-flight behavior of large composite structures and how damage would propagate in them. The damage initiation and propagation mechanisms in composite structures are very different from those in metallic structures. Damage mechanisms such as delaminations between plies, fiber breakage, matrix cracking and fiber-matrix disbonding initiate, propagate and fail very differently from traditional aerospace materials such as aluminum and titanium. This would lead to the design and certification requirements for composite structures being more complex and conservative than for metallic structures (Harris, Starnes Jr., & Shuart, 2002).

- Detecting damage was found to be extremely challenging. Internal defects and damage such as delaminations occur below the surface and may go unnoticed by mere visual inspection. Therefore a composite structure that looks visually undamaged on the surface may actually be severely compromised. Currently, approximately 80% of nondestructive evaluation of aircraft between major inspections is based on visual inspection (Hunter, et al., 2013). The introduction of composite structures would thus make this reliable and fast NDE technique for metals, obsolete. Other non-destructive inspection techniques often involve removing parts of the aircraft to gain access to both sides of the structure. This makes damage inspections much more expensive in terms of aircraft downtime.
- Limited standardization of composite materials and repair techniques compared to metals.
- The level of training and awareness required for inspectors and repair crew.

Thus, a reliable, accurate and quick damage detection methodology would allay concerns regarding the detection of damage in in-service composite structures. Current non-destructive techniques developed for use with composite structures are either insufficient or too costly in terms of time. Vision based NDE, as previously mentioned is not sufficient to conduct composite material inspections.

Ultrasonic and X-ray based methods (Bar-Cohen, 2000) are some of the most commonly implemented NDE techniques. Tests consist of a transmitter and receiver moving in tandem on either side of the structure. Variations in material density are sensed to detect damage. Both technologies have been widely accepted in the aviation industry since they can relatively easily and quickly scan a large area of structure. The largest disadvantage of these methods is that they require access to both sides of the structure which is time-expensive and sometimes not feasible. Single sided ultrasonic sensors are under development, but are still not reliable enough for deployment in aircraft inspection. Vibration based methods sense the modal response of the structure to a predetermined excitation from an external shaker or embedded actuators. A change in natural frequencies can be correlated to a change in stiffness and comparison with historical or analytical data can be used to triangulate the damage location. These methods are very easy to implement, but require a lot of complex signal processing.

The problem inherent with all these non-destructive techniques is that they are conducted only at discrete, fixed length and extremely conservative time intervals. They require bulky equipment to conduct damage assessment. They are also either not sufficient (as in the case of visual inspections) or are extremely expensive in terms of time and effort (as in the case of X-ray and ultrasonic NDE). A means to overcome the shortcomings of NDE based techniques is to conduct a continuous health assessment of the global structure.

1.1 Structural Health Monitoring

Structural health monitoring (SHM) is the process of implementing a damage identification strategy in a structure, where damage is defined as a change to material or physical properties of the system (Farrar & Worden, 2007). It involves the observation of a structure by embedding, or surface bonding actuators and sensors to continuously and remotely monitor damage with minimum human intervention. The primary goal of SHM is to detect and characterize damage in a structure that is operating in a noisy real-world environment. To this effect, SHM has been subdivided into five levels based on the sophistication and prediction capability of the system (Rytter, 1993). These five subdivisions are:

- Detect the presence of damage
- Locate the damage
- Predict the size and extent of damage
- Predict the kind of damage (delamination/fatigue/fiber breaks)
- Predict remaining useful life of the structure.

The implementation of a SHM system thus provides an estimate of the state of damage and remaining useful life of the structure on a continuous basis. The greatest advantage of employing a SHM system is the shift from regularly scheduled maintenance to potentially cost saving condition based maintenance. Condition based maintenance employs a SHM system that monitors the structure for damage, and warns the operator if damage has been detected. A SHM system capable of diagnosing damage and offering a prognosis on-demand is predicted to have a 25-33% total life cycle cost benefit (Ng, 1999). This confidence in the health of the structure would also lead to designers being able to relax current overly conservative factors of safety and thus take advantage of the weight savings potential of composite materials.

The greatest challenge posed by this system is that the reliability of the component now depends entirely on the reliability and accuracy of the SHM system. Since damage development is normally a highly localized phenomenon, trying to conduct SHM globally might require a highly dense sensor network. A fundamental challenge is also the development of a non-supervised system that reliably monitors structural health with little human intervention. Making the system reliable also requires that the sensor network be fail-safe. The network should continue to be operational even in the event of loss of one or more sensors. New military fighters such as the Eurofighter Typhoon continuously collect and analyze structural data just like a SHM system, but do not rely on it for their maintenance schedules, instead storing this data in ‘black boxes’ for investigating in-service failures. (Neumair, 1998).

SHM of composite structures has been conducted using multiple techniques and sensor technologies. The earliest methods employed to conduct SHM were vibration based techniques developed in parallel with the space shuttle program in the 1970s (Farrar & Worden, 2007). Damage causes a localized change in the stiffness of the structure. This localized change of stiffness causes a change in the modal response of the structure to a predetermined disturbance, and a correlation between the modal responses of an analytical model, the original structure and current structure can be used to detect and classify the damage. Vibration based techniques are considered more of a global monitoring solution rather than a local damage detection method which are more sensitive in nature (Fritzen, 2005).

Lamb wave based SHM is a relatively modern technique to identify damage. Lamb waves are high frequency acoustic waves that travel in thin plates. This makes them ideal for damage detection in thin composite structures like wing skins and fuel tanks. Lamb waves, generated by exciting an actuator at very high frequencies are bound to the structure and suffer very little attenuation when they come in contact with fluid mediums such as air, and instead reflect back into the structure. Reflections from a change or creation of a material boundary around the damage site are isolated and can be processed to identify damage. The advantage of using Lamb wave based techniques to conduct SHM in composite structures is that they have the potential to identify multiple kinds and sizes of damage (Giurgiutiu, 2008). Methods have been developed to detect the existence of damage (Crider, 2007), locate damage sites (Balasubramaniam, Vishnuvardhan, Muralidharan, & Krishnamurthy, 2009) and predict the extent of damage (Jha & Watkins, 2012) using these acoustic waves. New actuator and sensor technologies such as piezoelectric lead titanate zirconate (PZT) actuators and fiber Bragg grating (FBG) optic fiber based SHM (Guo, Xiao, Mrad, & Yao, 2011) have also greatly advanced the capabilities of Lamb wave based SHM by an increase in the sensitivity and sampling rate, and a decrease in size and weight.

1.2 SHM of Adhesively Bonded Composite Joints

The use of adhesively bonded composite structures has gained momentum in recent years due to a number of advantages over mechanically fastened structures. Adhesively bonded composite lap joints provide a more uniform stress distribution than mechanically fastened (riveted) joints leading to an increase in fatigue life. Other advantages of using adhesive bonding are the weight savings and the ability to join dissimilar components since there is no galvanic corrosion.

The requirement for a SHM system in adhesively bonded composite joints is primarily because predicting crack formation, propagation and ultimately failure is extremely difficult to model analytically. Li and Gaitonde (1998) showed that while it was possible to predict bond strengths of single lap joints, more complex structures required simplifications and assumptions to be made for correlations between analytical and experimental results. This lack of a comprehensive analytical method that is applicable to all joints leads to challenges in obtaining structural certification, resulting in either overdesign or abandonment of the use of composites as in the case of Mitsubishi's Medium Range Jet (Reade, 2010). Implementing a sensor network to track the health of the joint would significantly improve the confidence in adhesively bonded joints.

Lamb wave based ultrasonic SHM techniques are considered to be the most suitable methods to interrogate adhesively bonded joints due to their high sensitivity to small and varied damage types. Numerical finite element studies of ultrasonic wave based SHM in adhesively bonded joints (Zair, 2011) show that lamb wave based SHM can detect disbonds as well as impact damage, and that the structural response can be used to locate the damage site. Experimental studies by Quaegebeur, Micheau and Masson (2011) employed a Lamb wave based SHM system to detect disbonds in an adhesively bonded composite lap joint. The technique detected the size of the disbond in the joint by relating the strength of transmission of Lamb waves through the joint. Experimental studies on tracking of fatigue damage in adhesively bonded composite lap joints by Karpenko (2014) revealed that guided Lamb wave were capable of predicting the loss in stiffness of the joint. Studies to observe the effect of embedding thin sensors such as piezoelectric PZT elements and optic fiber based FBGs in a composite joint (Haq, Khomenko, Udpa, & Udpa, 2013), show that they are non-obtrusive and do not significantly alter the stress distribution and strength of the joint (Michaud, et al., 2014).

Triangulation is the process of determining the most likely location of damage based on sensory information obtained from multiple points. There a number of ways to conduct triangulation. Betz, Thursby and Staszewski (2007) successfully used directionally sensitive fiber Bragg grating sensors arranged in a rosette to obtain information about the direction of impact. Chang and Seydel (2000) were successful in triangulating damage in a plate by comparing wave propagation in an analytical model to experiment based sensory information. Purekar and Pines (2001) successfully demonstrated the use of phased arrays of piezoelectric transducers to create directional Lamb waves. The reflections from these directional waves were analyzed to locate damage. Balasubramaniam and Krishnamurthy (2009) successfully employed a “single transmitter multiple receiver” piezoelectric circular array employing the ‘time of flight’ methodology to locate damage in composite plates. Gangadharan and Gopalakrishnan (2010) developed a geodesic-based damage triangulation technique that employs a wavelet transform to identify features related to the ‘time of flight’ of the Lamb wave to-and-from the damage in metal plates. They also developed a complex weighting function so that the system could be adopted for composite materials.

1.3 Contributions

This study proposes a methodology to conduct SHM of an adhesively bonded composite lap joint using acoustic, guided Lamb waves. The proposed SHM system is capable of detecting the presence of damage, locating it and predicting the extent of damage. Lamb waves are excited on the structure using a PZT element. The response of the structure to the propagation of Lamb waves in the plates and adhesive layer is recorded using a laser vibrometer.

SHM is an inverse problem, that is, it compares a previous historical baseline which is considered healthy, to the current response. Any difference between the baseline structural response and the current structural response is an indication of a change in the material boundaries of the structure, thus indicating damage. The first instance of deviation between the healthy and current responses indicates the total time of flight of the excited Lamb wave from the PZT, to the new damage site and a reflected wave from the damage site back to the vibrometer sensor point. This time of flight determination, along with material properties of the laminate and the layout of the sensors with respect to the PZT, is used to create a locus of points along which damage is predicted to lie. The time of flight evaluated at multiple sensor points is used to generate multiple damage loci to triangulate the location of damage. A damage index variable is defined to visualize the predicted damage location. The extent of damage is evaluated by considering the strength of the wave that is transmitted through the joint. A secondary damage index variable is defined to quantify the extent of attenuation of the signal transmission as damage increases.

Finite element modeling of a joint in both 2D and 3D using ABAQUS, a commercially available FEA software, is used to study the effectiveness of the damage triangulation technique. The 2D simulation evaluates Lamb wave propagation in the cross-section of the joint. Plain strain linear quadrilateral elements are used for 2D model of the joint. The dynamic explicit simulations show Lamb waves as they propagate through the structure. The simulation is also capable of evaluating the time of flight of the wave. The 3D simulations are used to test the entire damage triangulation methodology. The plates are modeled using linear quadrilateral shell elements, and the PZT and adhesive layer are modeled using linear 3D stress elements. The dynamic explicit simulation is used to triangulate damage using three sensor points around the PZT. The damage triangulation from the numerical results shows good correlation between the predicted and actual damage locations.

Experimental validation of the methodology is conducted on two $[0/90/0/90]_s$ composite laminates joined using an epoxy based adhesive. The Lamb wave is mode tuned to provide maximum signal-to-noise ratio. Damage is caused in the lap joint using a drop tower. The experimental setup is able to determine time of flights at three sensor locations and thus triangulate damage. The difference between the predicted and actual damage sites is very small (less than 5% of the length of the structure). Experiments also show good reciprocity between the damage index and the number of impacts on the lap joint, thus validating the ability of the methodology to detect an increase in the size of damage. The experimental study covers three levels of SHM sophistication by detecting the presence of damage, locating it and judging its size with the aid of a damage index.

CHAPTER II

LAMB WAVE BASED DAMAGE DETECTION METHODOLOGY

This chapter comprises of the theoretical basis of the proposed SHM system that employs acoustic Lamb waves to identify damage in adhesively bonded composite lap joints. It offers an introduction to acoustic waves, and describes Lamb wave propagation. It then describes how the wave packets generated by using a tone burst signal can be analyzed in the time domain to obtain the time-of-flight of a wave that has reflected off the damage, and proposes how the time-of-flight of the wave can be used to locate damage in a composite lap joint.

2.1 Acoustic Waves

One of the most popular methods of conducting SHM in thin structures is by studying the propagation of acoustic waves in the structure. In solids, an acoustic wave can propagate in four fundamental oscillatory motions.

2.1.1 Longitudinal Waves

In longitudinal waves, the oscillations occur in the direction of wave propagation. As seen in Fig. 2.1, particles in the medium oscillate along a line about their equilibrium position, creating regions of compression and rarefaction. The wave is visualized as collective motion of the compressed region.

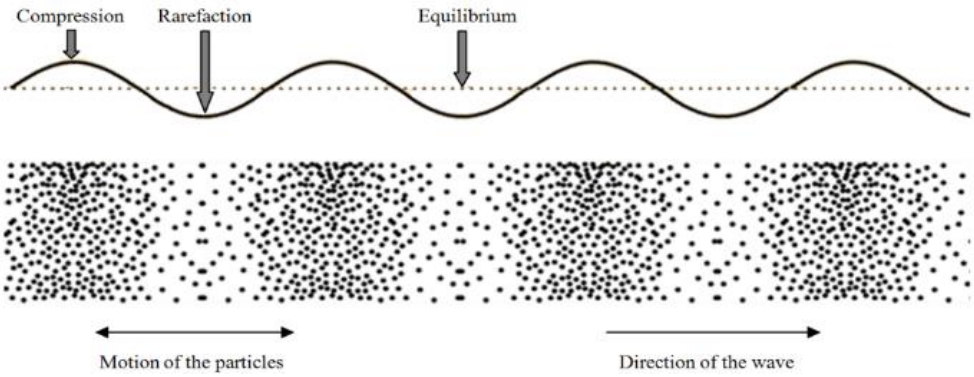

Figure 2.1 Motion of longitudinal waves

(NDT, 2015)

2.1.2 Shear Waves

Particles in transverse or shear waves move perpendicular to the direction of wave propagation as seen in Fig. 2.2. Just like longitudinal waves, particles in shear waves oscillate along a line about their equilibrium position. NDE technologies such as A-scan and C-scan ultrasonic scanners employ longitudinal and shear wave technologies to detect internal damage in structures, since these waves can penetrate thick sections such as welds and thick plates.

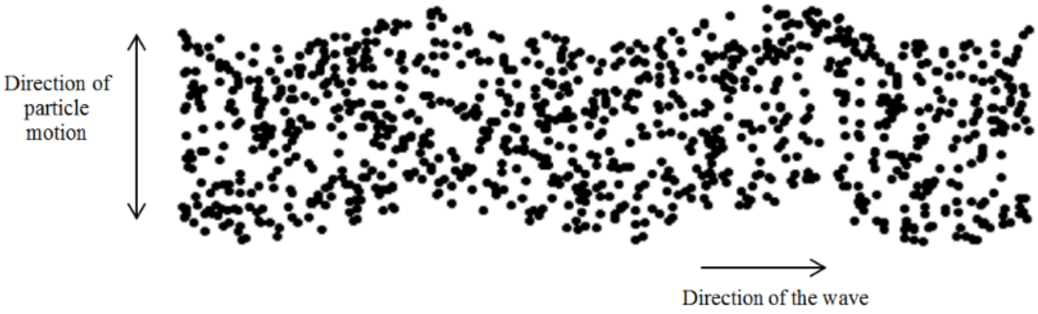

Figure 2.2 Particle motion in shear waves

(NDT, 2015)

2.1.3 Guided Rayleigh Waves

Guided waves are low impedance acoustic waves that are confined between material boundaries of a solid. They can travel large distances and inside curved surfaces resulting in relatively greater coverage area, while using fewer sensor-actuator pairs. They are hence, ideal for ultrasonic SHM of thin plates (Thomson & Chimenti, 2002).

Rayleigh waves are a class of guided waves that propagate on free surfaces of solids. They penetrate approximately one wavelength deep into the structure. The particle motion is elliptical, with the major axis of the ellipse perpendicular to the wave propagation direction. The particles that lay up to 20% of the wavelength depth rotate in one direction and the lower particles rotate in the other, i.e., as seen in Fig. 2.3 if the surface particles rotate in the clockwise direction, the internal particles rotate in the counter-clockwise direction.

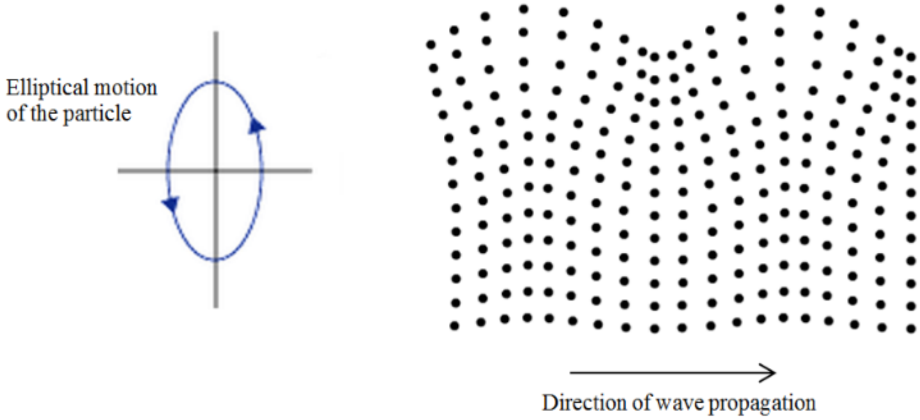

Figure 2.3 Particle motion of Rayleigh waves

(NDT, 2015)

2.1.4 Guided Lamb Waves

The existence and mathematical formulation of stress waves traveling in 2D elastic plates was first postulated by Prof. Horace Lamb and Lord Rayleigh in 1917 (Lamb, 1917). They found that the shape and velocity of these waves depended only on the thickness and Young's Modulus of the structure. The particle vibration velocity (phase velocity) and the velocity of the wave packet (multiple waves of varying frequencies travelling together – group velocity) are both derivable from material properties of the plate, its thickness and the wave's frequency. A sample dispersion curve showing the variation of group velocity with frequency for a 1.22mm thick AS4/8552 [0/90/0/90]s laminate is plotted in Fig. 2.4. The data to plot the curves was generated using DISPERSE (Lowe & Pavlakovic, 2013); a commercially available software to generate dispersion curves for multilayered structures.

The motion of the particles in a thin plate when a Lamb wave passes through them can either be symmetric (S wave) or anti-symmetric (A wave), and are referred to as modes of the Lamb wave. The dominant waves at low frequencies are referred to as the S_0 and A_0 modes, while higher modes such as A_1, S_1, A_2, S_2 etc. begin to dominate at higher frequencies as seen in Fig. 2.4. The figure also reveals that multiple modes can exist at a given frequency.

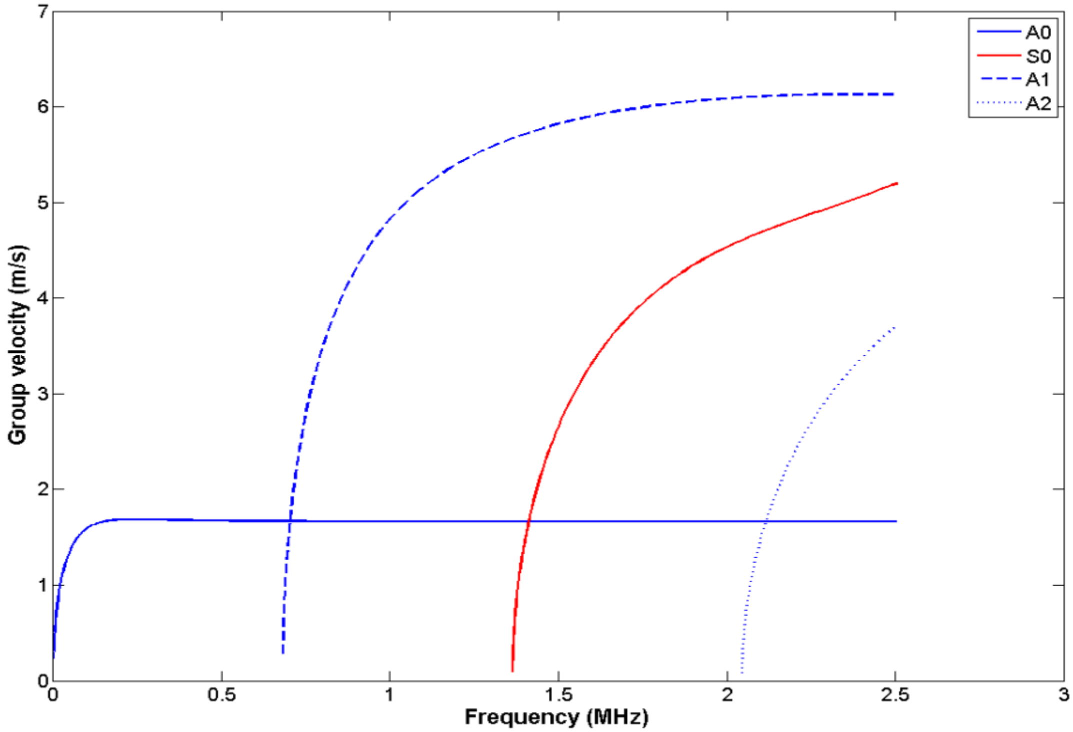

Figure 2.4 Lamb wave group velocity dispersion curve

Dispersion curves generated for a 1.22mm thick AS4/8552 $[0/90/0/90]_s$ laminate generated using DISPERSE

At low frequencies, the displacement field of a S_0 wave is identical to that of an axial wave (Giurgiutiu, 2008). Therefore, at low frequencies an axial excitation of the structure produces high amplitude symmetric Lamb waves. Similarly, the displacement field of an A_0 wave closely resembles that of a flexural wave. Fig. 2.5 shows the shape of a S_0 and an A_0 wave. A transducer that excites the surface of the plate in the normal direction at low frequencies will create dominant, high amplitude A_0 Lamb waves (Gaso, March-Iborra, Montoya-Baides, & Arnau-Vives, 2009).

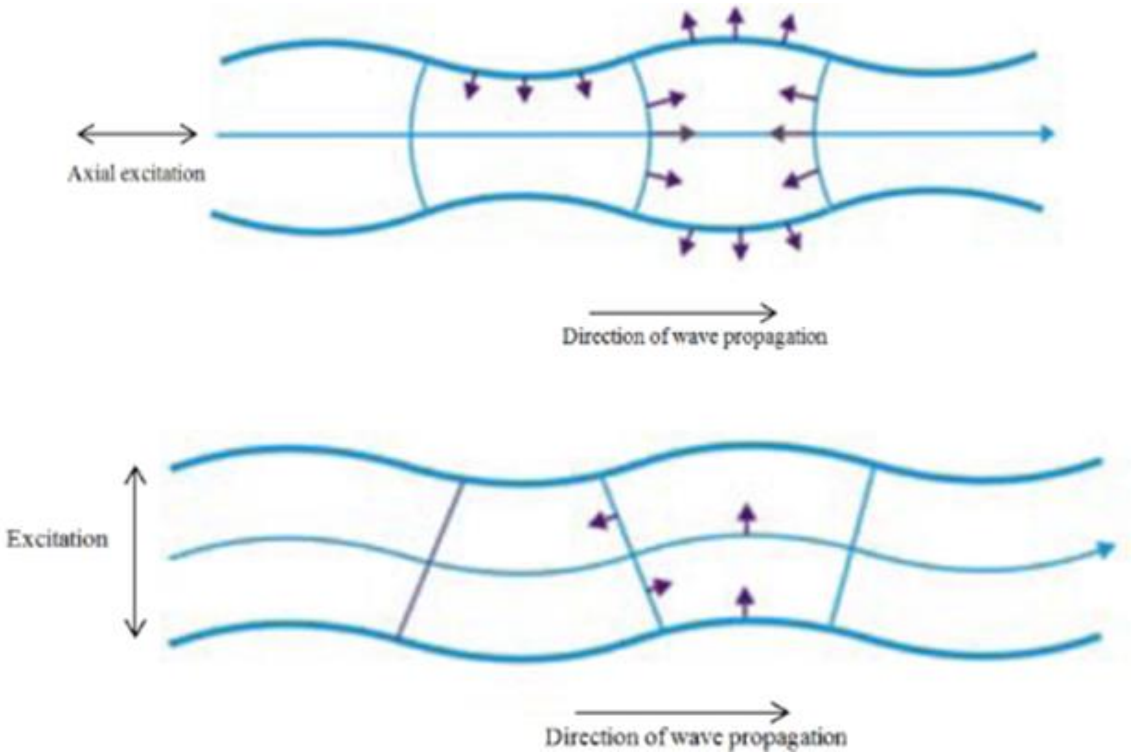

Figure 2.5 Lamb wave symmetric and anti symmetric modes

(top) Axial excitation of a plate leading to symmetric waves and (bottom) transverse excitation leading to the formation of anti-symmetric waves (Gaso, March-Iborra, Montoya-Baides, & Arnau-Vives, 2009)

2.2 Excitation Signal

The speed of a wave in a composite material is dependent on the stiffness, density, thickness and the frequency of the wave. The dependence of wave velocity on the wave frequency is known as the dispersive nature of wave propagation. The greater the number of frequencies associated with the wave, the more it distorts and elongates. A tone burst is the combination of a single frequency sinusoidal wave and a signal modulation algorithm such as a hanning window or a Gaussian window. Fig. 2.6 shows how a hanning window modulation is used to generate a 5.5 cycle tone burst. The advantage of using a tone burst as opposed to a sinusoidal excitation signal to generate the wave is that even though the frequency response of a sinusoidal waveform displays a dominant frequency, it also has a large amplitude response to neighboring frequencies in the form of secondary peaks as seen in Fig. 2.7. A tone burst has one dominant peak in the frequency response and insignificant secondary peaks.

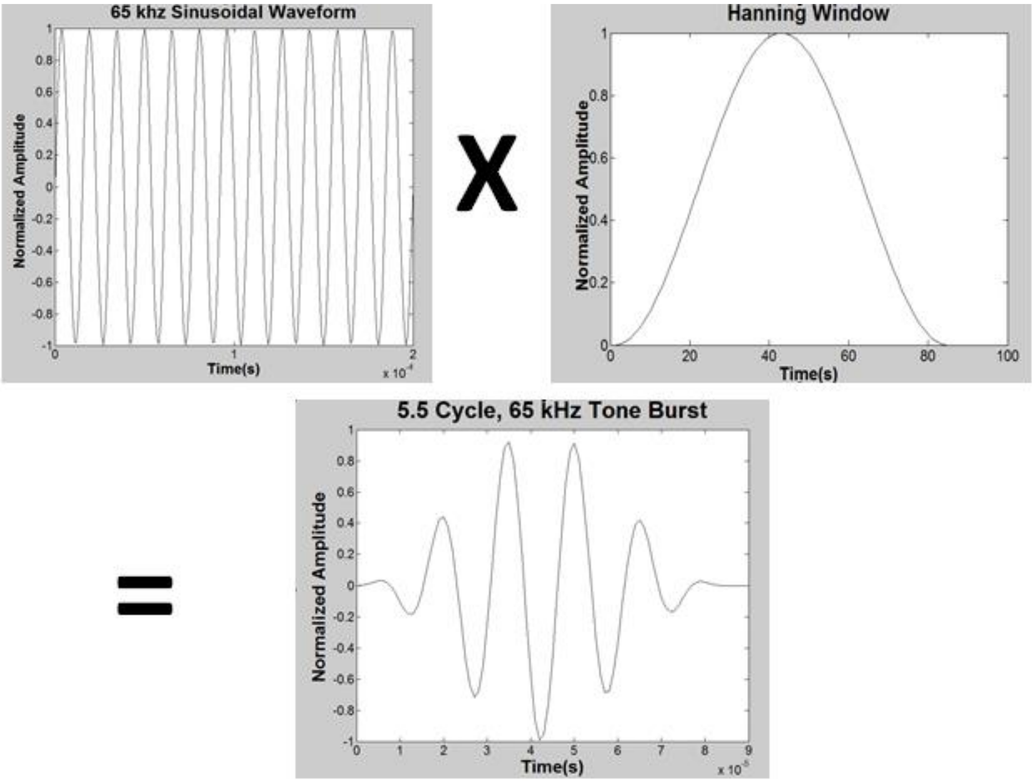
65 khz Sinusoidal Waveform

Hanning Window

5.5 Cycle, 65 kHz Tone Burst

Figure 2.6 The generation of a 65kHz 5.5 cycle tone burst

The tone burst (bottom) is created from the product of a 65kHz sinusoidal wave (left) and a hanning window (right)

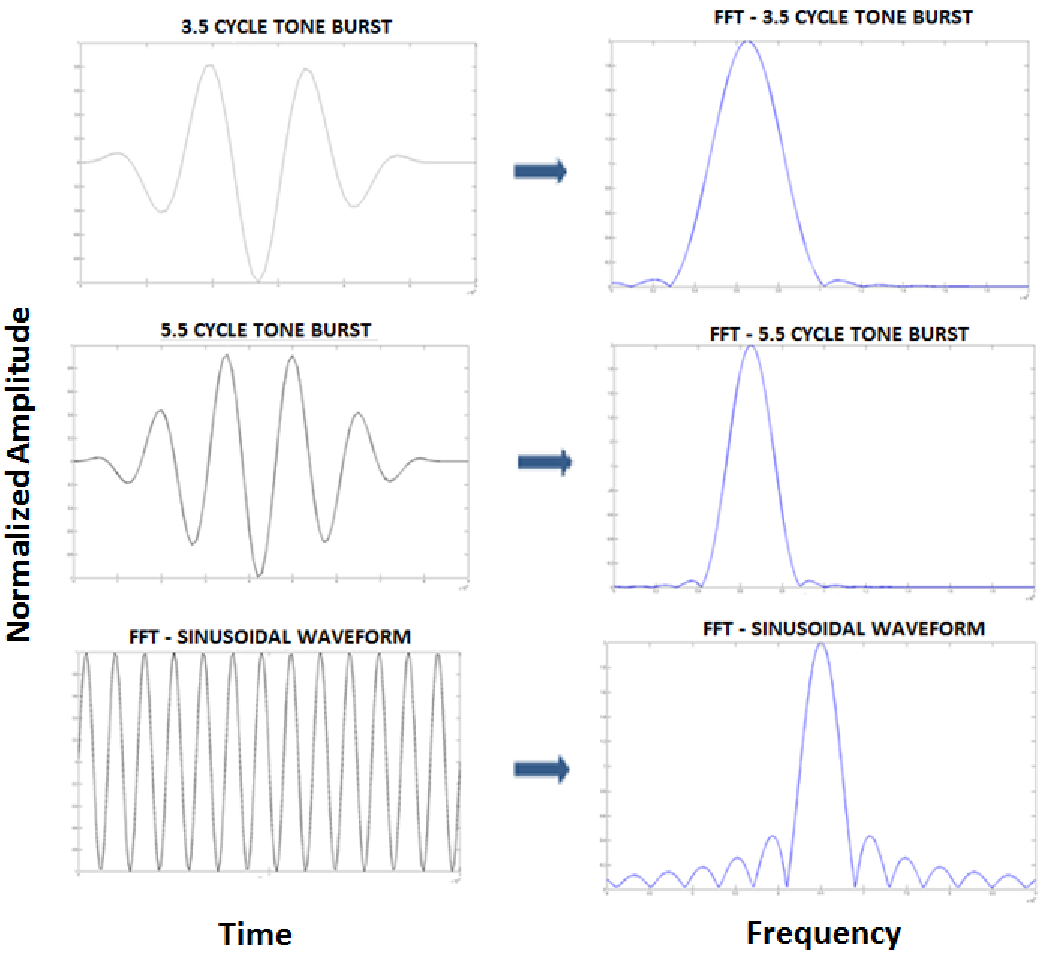

Figure 2.7 Comparison of frequency responses

The three signals compared are (top) a 3.5 cycle tone burst; (middle) a 5.5 cycle tone burst and (bottom) a raw sinusoidal excitation. The tone bursts, as opposed to the sinusoidal signal, have a single Gaussian distribution of frequencies centered on the dominant frequency. The FFTs of the two tone bursts also indicates that the greater the number of cycles in the tone burst, the narrower the bandwidth of the Gaussian distribution. Data generated using signal analysis toolbox in MATLAB.

2.3 Piezoelectric Transducers

The piezoelectric effect is the ability of certain materials to generate an electric field when subjected to mechanical strain (direct), and conversely to undergo mechanical strain when subjected to electrical charge. The direct effect makes it applicable as a strain sensor, and the converse effect makes it useful as a small-strain actuator. This effect is seen in both naturally occurring materials such as quartz, topaz, cane sugar and bone ('*piezoelectricity of bone is thought to act as a biological force sensor and aid in its growth and regeneration*') (Singh & Saha, 1984) and in man-made materials such as barium titanate and lead zirconate titanate (PZT). Fig. 2.8 shows a circular PZT mounted on an aluminum plate to generate Lamb waves.

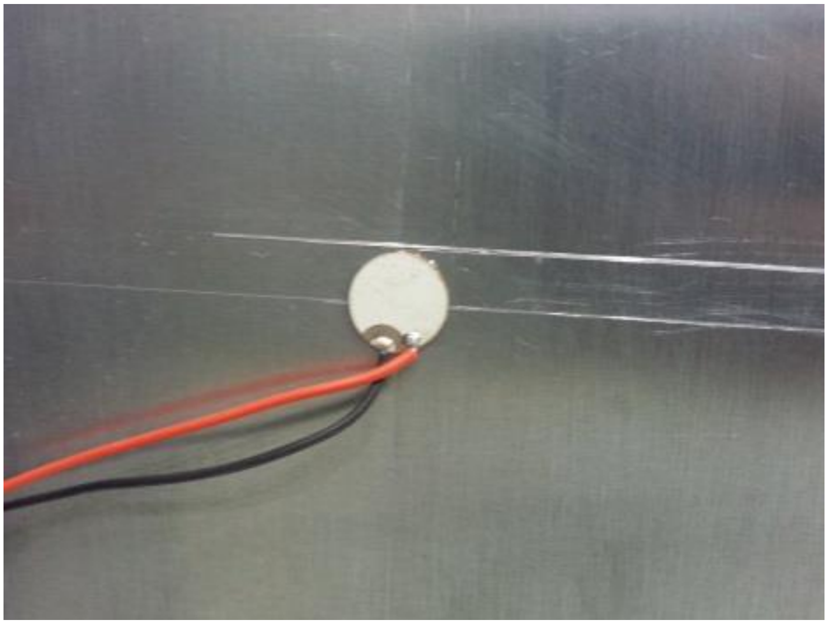

Figure 2.8 PZT mounted on an aluminum panel using an epoxy based adhesive. The red and black wires transfer the signal voltage across the upper and lower surfaces of the PZT.

PZT actuators have become one of the most popular Lamb wave generators due to a number of advantages they have over traditional ultrasonic actuators. Traditional actuators are generally weakly coupled to the structure's surface using a gel or water. Since actuators induce waves by striking the surface, this weak coupling leads to signal attenuation and distortion. By contrast, the strong adhesive bond between PZTs and the surface that they are mounted to, induce waves by coupling the particle motion at the interface of the PZT and the structure. This makes them more efficient than traditional actuators at both inducing and sensing Lamb waves. They also have a considerably larger bandwidth of excitation frequencies (Giurgiutiu, 2008).

PZTs are minimally invasive. The PZT elements used in our experiments weighed 3gm and were 1mm thick. It can thus be mounted to the surface or embedded within plate structures or lap joints, without significantly altering the mechanical properties of the structure (Michaud, et al., 2014). In contrast a conventional ultrasonic transducer weighs 50gm and is 1.6cm thick (Piezo, 2015). PZTs are also comparatively many times less expensive, can be designed to be omni-directional or uni-directional, and can be quickly and easily cut into any desired geometry.

2.4 PZT Mode Tuning

PZTs have been used to generate and sense Lamb waves in both metals (Nieuwenhuis & Neumann, 2005) and composite materials (Kessler, Spearing, & Soutis, 2002). Depending on the shape and size of the PZT, the amplitude of the Lamb wave modes vary with the excitation frequency. At very low frequencies the amplitude of the A_0 wave generated by the PZT is dominant, whereas the amplitude of the S_0 wave is almost negligible in comparison. As the frequency increases the amplitudes of the S_0 and A0 modes increase, reach a peak, and then begin to decrease. Fig. 2.9 shows a sample Lamb wave tuning plot generated using experiments performed at RFRL.

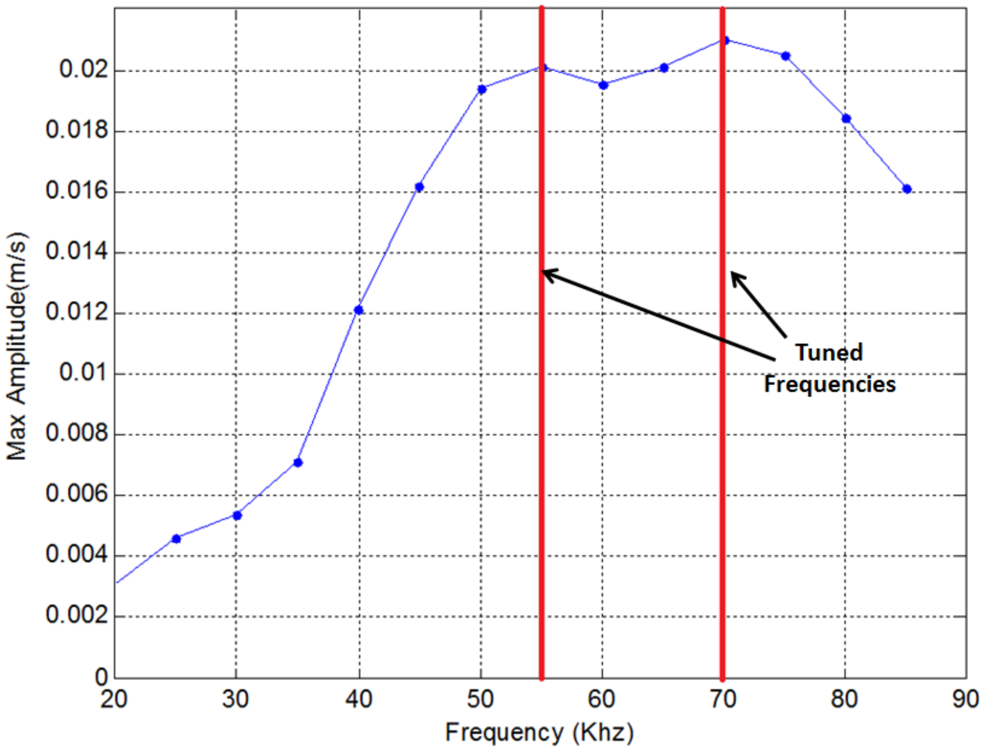

Figure 2.9 Determination of tuned frequencies.

Maximum amplitude of the structural response plotted against the excitation frequency of the PZT. The response of the A_0 mode peaks twice, once at 55 kHz and once at 70 kHz.

The frequencies at which the A_0 and S_0 modes peak, are considered tuned frequencies or ‘sweet spots’, and these tuned modes can be used to detect specific kinds of damage. The anti-symmetric modes are more sensitive to in-plane damage such as delaminations and disbonds, whereas the symmetric modes are more sensitive to through-thickness damage (Giurgiutiu, Bao, & Zhao, 2003).

2.5 Damage Detection Using Acoustic Waves

A boundary is defined as a line, on either side of which, neighboring particles have different properties. The edges of plate for example are defined as a material boundary because at the edge, one side displays properties of the plate material and the other displays properties of the immersion media (air/water/vacuum). A discontinuity or damage in composite materials significantly alters the local material properties of the composite so that the interface between the healthy and damaged sections too, behaves like a material boundary. When a wave is incident on a boundary, a part of the energy of the wave is reflected back into the incident material, and the remaining is transmitted through the boundary in to the second material. Lamb waves are ideally suited for acoustic damage detection because the energy transmitted through the material boundary is very low. Thus, at a material interface such as with air or water, almost the entire energy of the incident wave is reflected back into the material. The amount of energy transmitted through the material interface can also be used to assess the size of damage. As the difference between material properties across the boundary increases, the amount of energy reflected back towards the source of the incident Lamb wave increases. Thus as damage increases, the strength of the reflected wave increases and strength of the transmitted wave decreases.

The most common Lamb wave based ultrasonic methods for damage detection are the pitch-catch and pulse echo techniques. The pulse-echo technique uses the same PZT to both excite the structure and to detect its response from the excitation. The pitch-catch technique uses separate elements, one to excite the structure and the other to measure the acoustic response. Fig. 2.10 shows the principle of operation of the pitch-catch technique. The pitch-catch technique was implemented in our methodology and experiments because of the simplicity and accuracy in measurement achieved by using a laser vibrometer as the sensor element. This was because of a number of advantages that the vibrometer offers over the PZT

- The vibrometer, unlike a PZT element, was not susceptible to electro-magnetic interference.
- The vibrometer was also suitable to the damage detection since it required sensing at multiple locations for triangulation of the damage site. Therefore the only weight addition to the structure to conduct experiments was the one excitation PZT.
- Piezo sensors needed to be mounted permanently to the structure, whereas the vibrometer could just be pointed to a different location to sense its response.

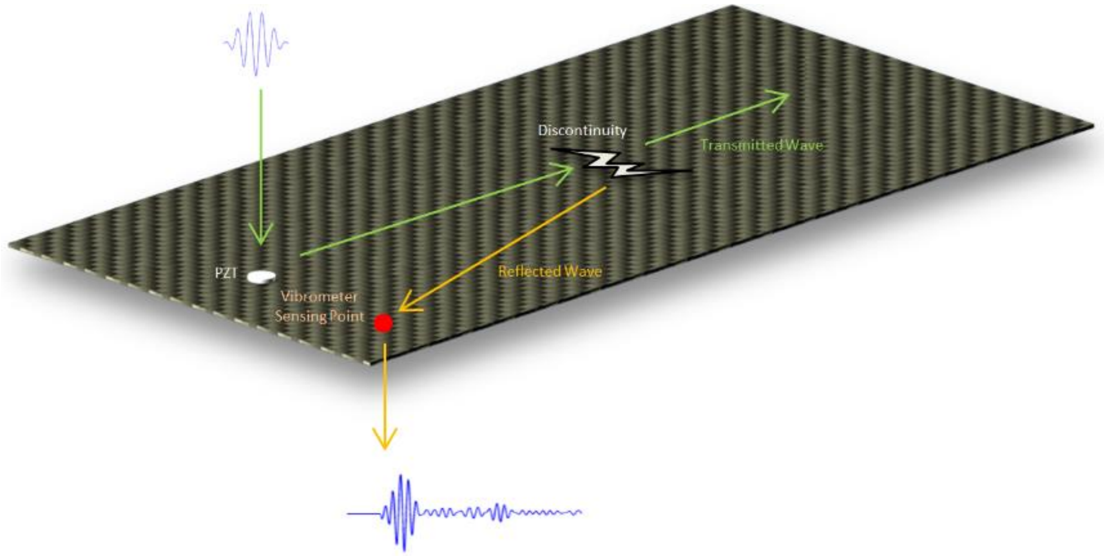

Figure 2.10 Principle of operation of pitch-catch based Lamb wave SHM.

The waves travel from the excited PZT in all directions. When a component of the wave hits a discontinuity, a part of the energy of the wave is reflected and the rest is transmitted through. The reflected wave is sensed by the vibrometer.

2.6 Time of Flight

This methodology works by comparing the response of the structure to a tuned, PZT excited tone burst in its baseline healthy form to its current damaged form. The tuned Lamb waves emitted by the PZT element propagate through the structure. The vibrometer captures the structure's response to the Lamb wave propagation in the form of the out-of-plane velocity. The resulting waveform contains the velocity profile of the Lamb wave when it passes through the sensing point along with profiles of subsequent reflections from material boundaries such as the physical edges of the plates, the edges of the lap joint and pre-existing damage. When the plate is damaged, the damage site behaves like a new material boundary causing Lamb waves to reflect from it. These reflections either constructively or destructively interfere with the baseline waveform. This altered waveform is compared to the response of the original baseline structure. The time instant at which the 'damaged waveform' begins to deviate from the 'baseline waveform' is considered to be the time of flight of the wave to travel to, reflect off and be sensed by the vibrometer.

2.7 Velocity of Lamb Waves

Since the propagation of the wave is dispersive, each component of the wave that is associated with a certain frequency travels with a different velocity. The velocity of individual components is referred to as the 'phase velocity'. Due to the variation in phase velocity, the wave packet deforms into an elongated shape, and the wave packet as whole has another velocity associated with it called the 'group velocity'. Fig 2.4 shows the dispersive nature of the symmetric and anti-symmetric waves in terms of group velocity. The distance to the damage is a function of both time of flight and the velocity of the wave. The velocity considered to obtain the distance to damage is the velocity of the entire wave packet (group velocity).

2.7.1 Isotropic Material

The group velocity of a wave in a plate is a function of thickness, density, and elastic moduli. For a plate of uniform thickness made of an isotropic material, the group velocity is a constant in all directions. Therefore the wave propagation from a circular shaped PZT is circular, since the wave is travelling at the same group velocity in all directions as shown in Fig. 2.11. The data for these plots was obtained using ABAQUS.

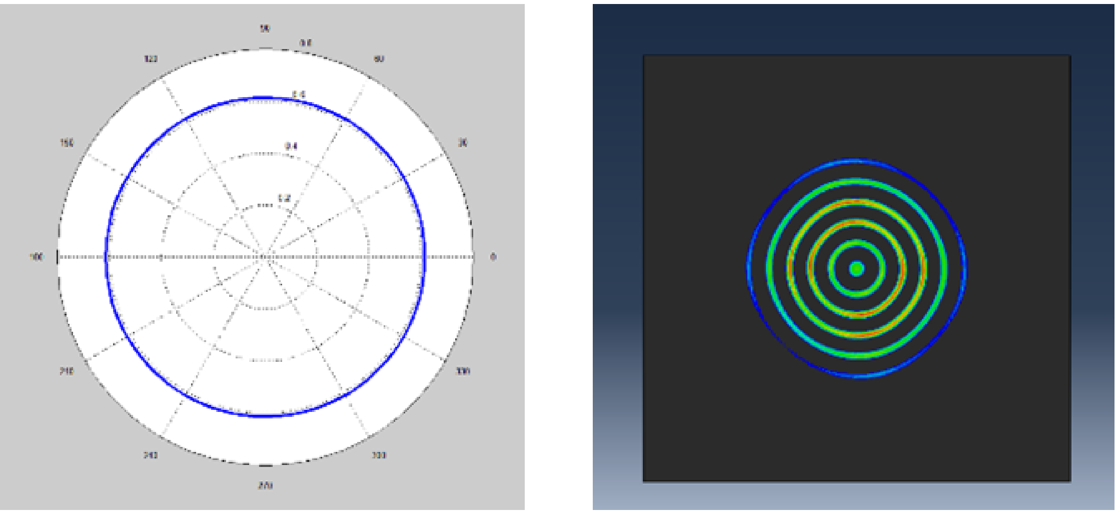

Figure 2.11 Velocity profile of Lamb waves propagating in an isotropic plate

The velocity profile of a 1.2mm thick aluminum plate (left) and a FEA simulation (right) plotting the of the out-of-plane velocity in a plate. The simulation demonstrated circular crested Lamb waves propagating in an aluminum plate

2.7.2 Composite Materials

Due to the anisotropic nature of composite materials, the elastic moduli of laminae vary depending on their orientation. This implies that the velocity of the wave in the laminate is also a function of the propagation angle. The velocity profile is hence not a perfect circle. The velocity profile generated for a 1.2mm thick AS4/8552 prepreg $[0,90,0,90]_s$ laminate shows high velocity in the 0° and 90° direction and low velocity between 30° and 70°. This dependence of group velocity on wave propagation angle makes predicting distance to damage challenging as the wave propagating from the PZT to the damage site and the wave propagating from the damage site to the vibrometer sensing point are not parallel. The excitation and the reflected waves not propagating along the same orientation imply that their group velocities are not the same. Fig. 2.12 shows the case of directionally affected Lamb waves generated in an anisotropic material. The data for these plots was obtained using ABAQUS.

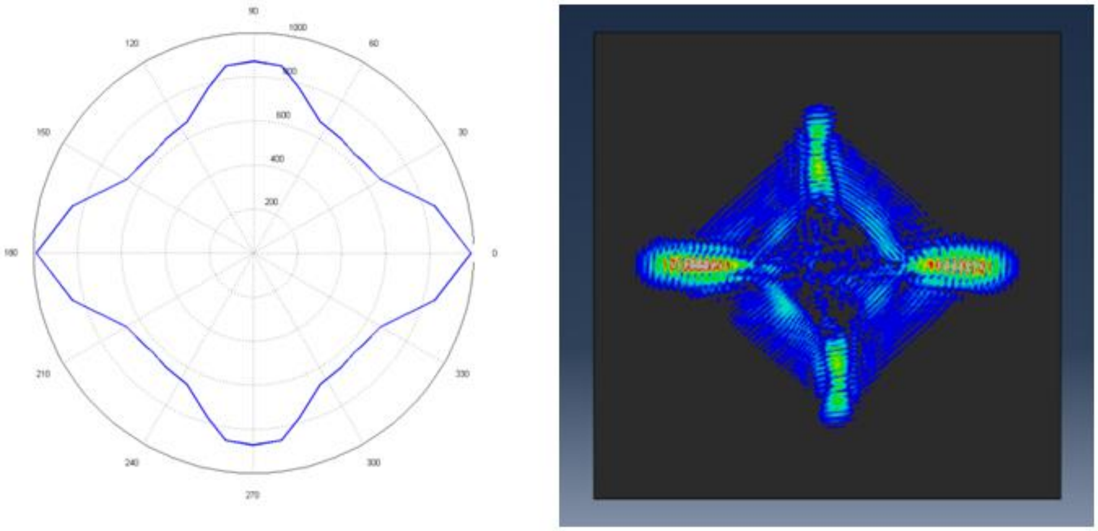

Figure 2.12 Velocity profile of Lamb waves propagating in a composite plate

The velocity profile of a 1.2mm thick AS4 8552 prepreg laminate $[0,90,0,90]_s$ (left) and a FEA simulation plotting the of the out-of-plane velocity in a plate. The simulation demonstrated wave propagation in the composite laminate (right) and showed the dependence of in-plane Lamb wave velocity to propagation direction.

2.8 Triangulation

Triangulation is the process of determining the most likely location of damage based on sensory information obtained from multiple points. The method described below uses the time of flight of the wave as it propagates from the PZT to the damage and then to the sensor, along with the slowness properties of the composite laminate to create a locus of the possible points of damage. The region in which these loci approached each other the closest indicated a high probability of damage. A damage index algorithm was developed to create a visual representation of the plate and the predicted damage location.

2.8.1 Locus of Points of Damage

The only information available to predict damage location from the experiment was the total time of flight of the wave (from the PZT to the sensory location after reflection from the damage) and the velocity profile (Fig. 2.12). The aim is to create a radial locus of points along which the damage could lie using just this information. Fig. 2.13 shows a flow chart depicting the algorithm used to create the damage prediction locus. The aim of the algorithm is to minimize the error between the estimated and actual sensor position. t_1 is the time of flight of the wave from the PZT to the estimated damage. Similarly V_1 is the velocity of the Lamb wave propagating at an angle θ_1, and d_1 is the distance between the PZT and the estimated damage. t_2, V_2, θ_2 and d_2 are the time of flight, wave velocity, wave propagation angle and distance between the estimated damage and the predicted vibrometer sensor position. As can be seen in Fig. 2.14, if t_1 was estimated too low, the algorithm over predicted d_2 and vice versa. The correct prediction of d_2 results in one point at which damage is predicted to lie. As θ_1 is varied from 0° to 360°, the algorithm results in a locus of points along which damage is predicted to lie, as seen in Fig. 2.15.

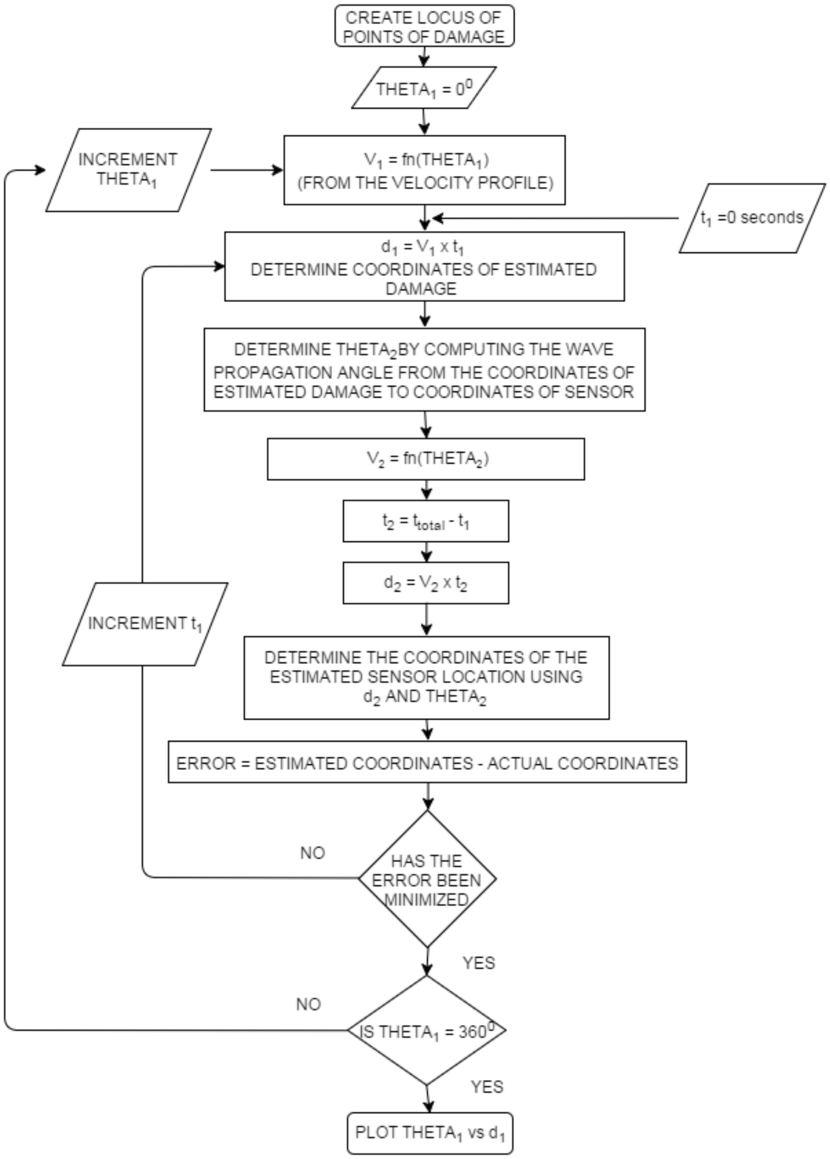

Figure 2.13 Flowchart of the triangulation algorithm.

The algorithm is used to create the damage locus. Each point on the locus is created by minimizing the error between the estimated and actual coordinates of the sensor location

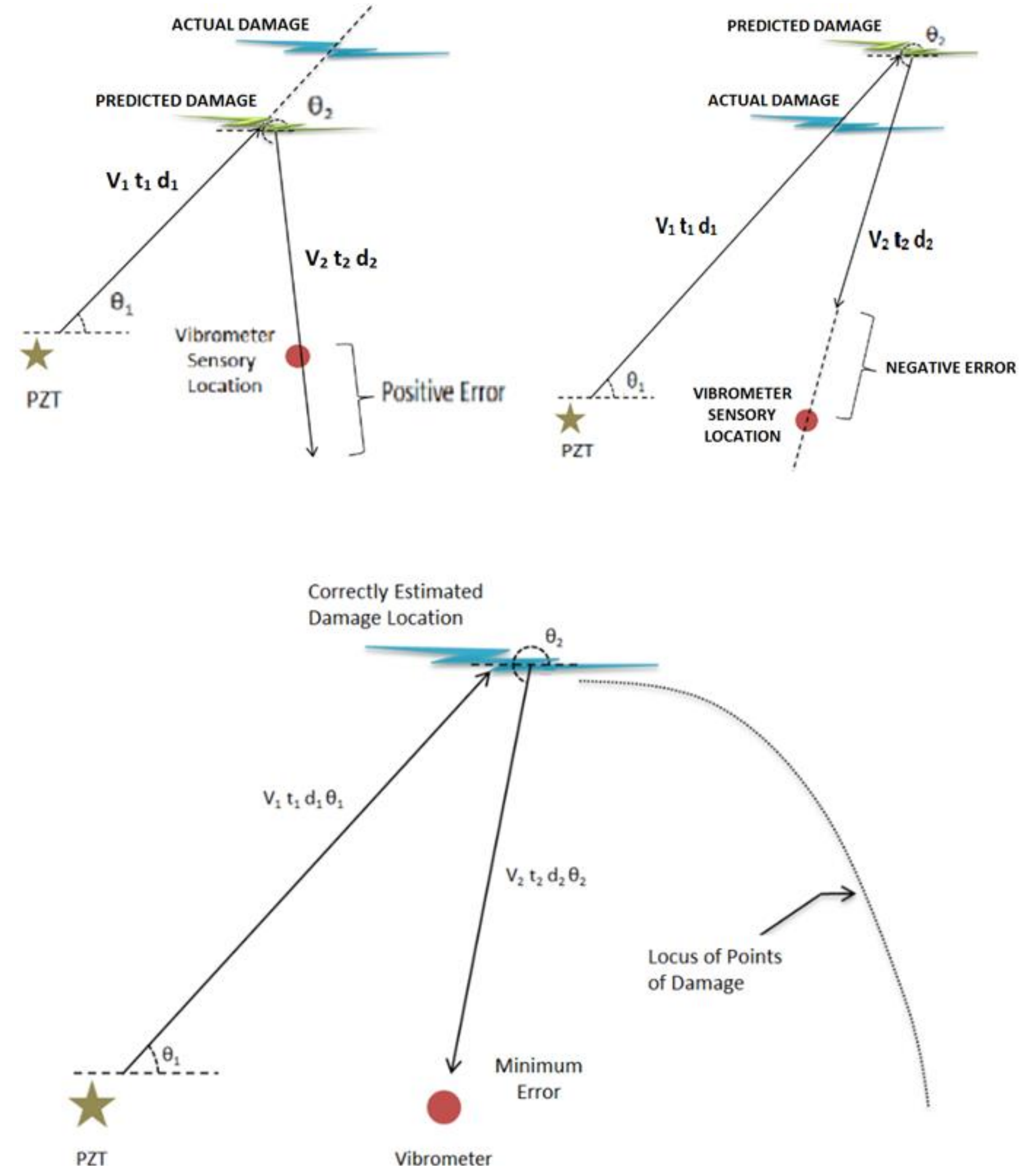

Figure 2.14 The error minimization algorithm to determine time of flight of the wave

Underestimating t_1 causes an over-prediction of d_2 (top-left) and overestimating t_2 causes an under-prediction of d_2 (top-right). Correct prediction of damage location (bottom) minimizes error between the estimated and actual vibrometer sensor position. The diagram also shows a locus of points of correctly estimated damage locations, which are obtained by varying θ_1

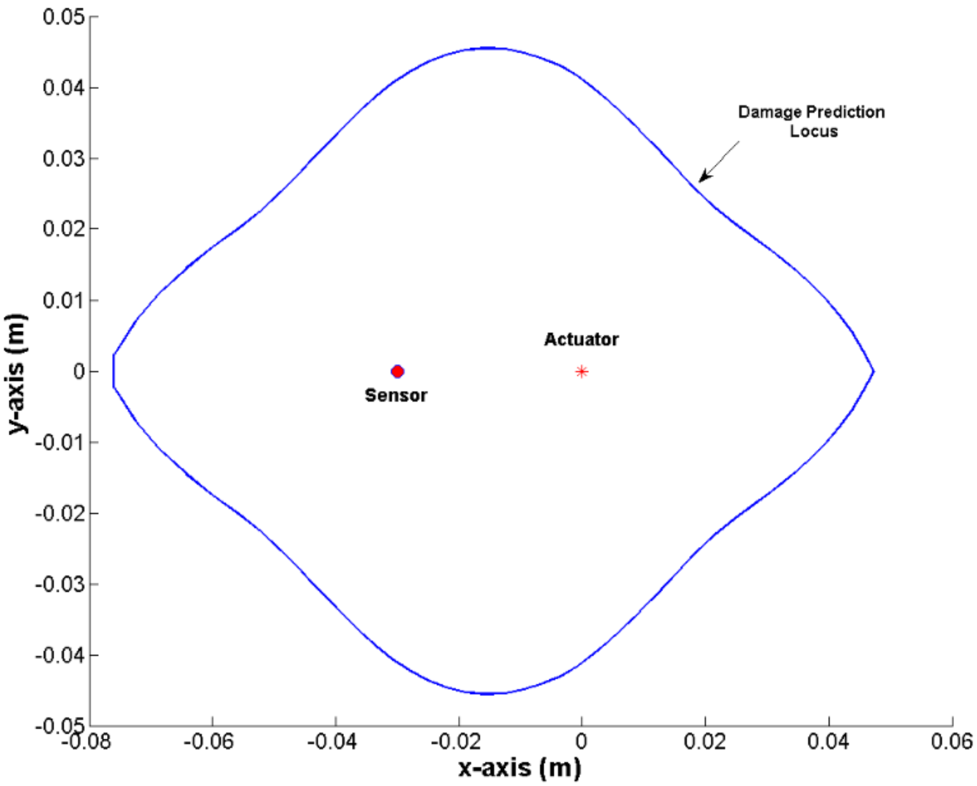

Figure 2.15 Locus of estimated damage location points generated using MATLAB. Code attached in Appendix A

2.8.2 Triangulation

Every sensory location created one locus of points. Since there was no information regarding the direction of damage, a single locus could not be used to locate the damage. The solution to this problem was to use multiple sensory locations to generate multiple loci. The point of intersection or overlap of two or more loci indicates a high probability of damage. Two loci that were obtained from sensory locations which are symmetrically situated around the PZT location, gave rise to two possible damage locations as seen in Fig. 2.16. Therefore a third sensory location was used. Fig. 2.17 shows two locations that are symmetric about the x-axis and one location that is offset towards the right.

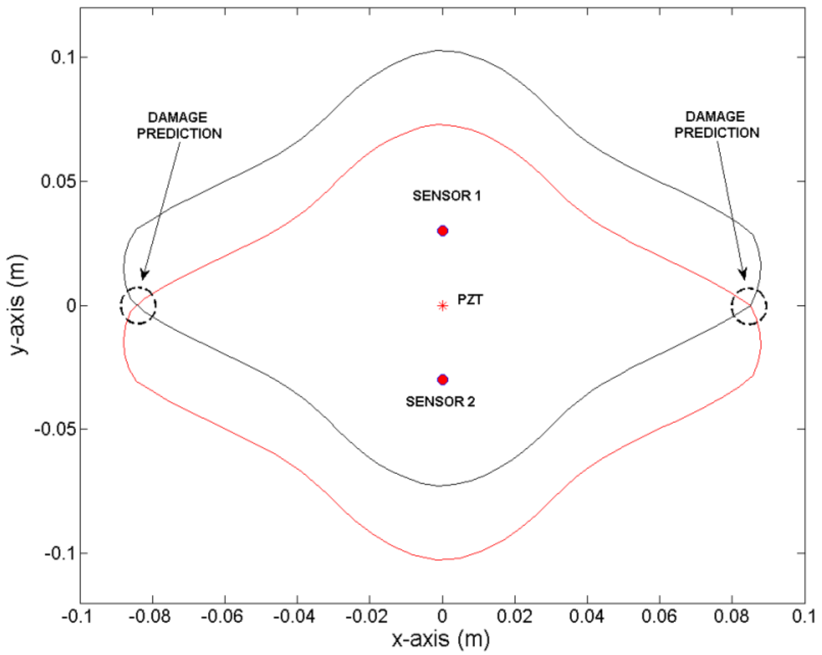

Figure 2.16 Damage prediction from two symmetrically located sensor points

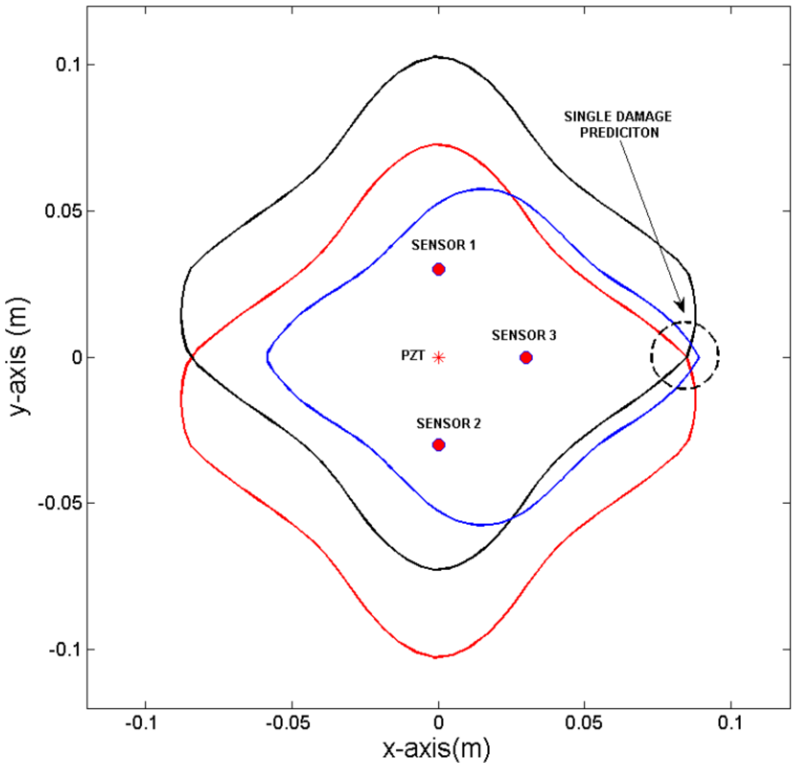

Figure 2.17 Damage prediction using triangulation from three sensor locations

2.8.3 Damage Index

The objective of creating a damage index (DI) was to automate the prediction of damage location using the loci instead of trying to predict it using human interpretation. Since the generation of the DI value is computationally expensive for a very fine grid, only the area of the locus plot that lies within the structure was evaluated.

As an example, a 40cm long and 8cm wide structure was divided into very fine grid points. The DI algorithm determined the shortest distance between the grid point and each individual locus. The sum of these distances was assigned as the DI value of that grid point. This algorithm is shown in the form of an equation as shown below.

$$DI_{x,y} = \sum_{i=1}^{n} d_i \tag{2.1}$$

$DI_{x,y}$ is the damage index value generated at coordinates (x,y), n is the number of sensory points used in the triangulation and d_i is the minimum distance between the grid point located at (x,y) and the i^{th} locus. Fig. 2.18 shows the DI plot of the example loci in Fig. 2.17 for the 40cm x 8cm lap joint structure.

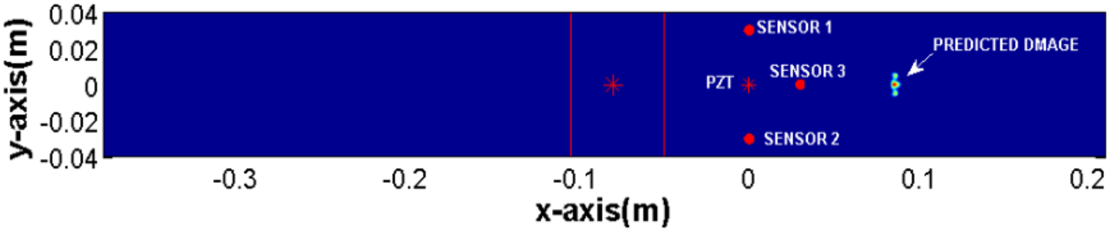

Figure 2.18 Damage index plot generated using MATLAB.

The loci in Fig. 2.17 are used to compute the DI at each grid point.

CHAPTER III

LAMB WAVE BASED SHM OF LAP JOINT - NUMERICAL STUDIES

In order to investigate the ability of the methodology to successfully locate damage with the instruments available, a numerical study consisting of both 2D and 3D models was conducted using the commercially available finite element solver ABAQUS. The 2D model was an inexpensive method to simulate wave propagation characteristics along the length of the model, visually see reflections of the wave and test the time of flight method. The 3D model was expensive in terms of time, but was an excellent validation technique for the triangulation methodology. It also more accurately replicated our experiments since it is possible to create a more realistic model that simulated wave propagation along both the length and width of the structure.

3.1 2D Finite Element Simulations

The 2D model was constructed to qualitatively and quantitatively understand the wave propagation characteristics, and to validate the 'Time of Flight' portion of the methodology proposed in Chapter II. The low cost associated with these simulations allowed multiple cases to be run, facilitating the study of the effect of varying the model, its boundary conditions, material properties, excitation signal, damage location and elements used.

3.1.1 Preprocessing - Geometry

The geometry assumed for the analysis was two [0/0/0/0] unidirectional laminates 15cm long with a 0.64mm thick adhesive layer between a 5cm lap joint. The thickness of each lamina was assumed to be 0.45mm. The material section of the plate modeled in this simulation was assumed to be isotropic for simplicity's sake. The Young's modulus assigned to the plate was the modulus of the lamina in the fiber direction (125 GPa) with a Poisson's ratio of 0.31 and a density of 1525 kg/m^3. The adhesive was Henkel Hysol EA 9309.3NA, a two part epoxy resin with an isotropic Young's modulus of 127 MPa, Poisson's ratio of 0.3 and a density of 1200 kg/m^3.

3.1.2 Boundary Conditions and Loads

As seen in Fig. 3.1, the left face of the upper composite plate was constrained completely in both displacement and rotation. The boundary condition is referred to as "Encastre" in ABAQUS. The excitation signal was a 5.5 cycle, 65 KHz tone burst and was excited as a uniformly distributed pressure on the upper surface of the lower plate as seen in Fig. 3.1. The tone burst signal is as shown in Fig. 3.2. The MATLAB code used to generate the tone burst is in Appendix B.

Figure 3.1 FEA model of the adhesive lap joint

The adhesive joint was between two 15cm long, infinitely wide AS4 3501-6 [0/0/0/0] laminates. The composite section is in grey and adhesive in yellow. The Encastre boundary conditions and dynamic tone burst loads are also visible.

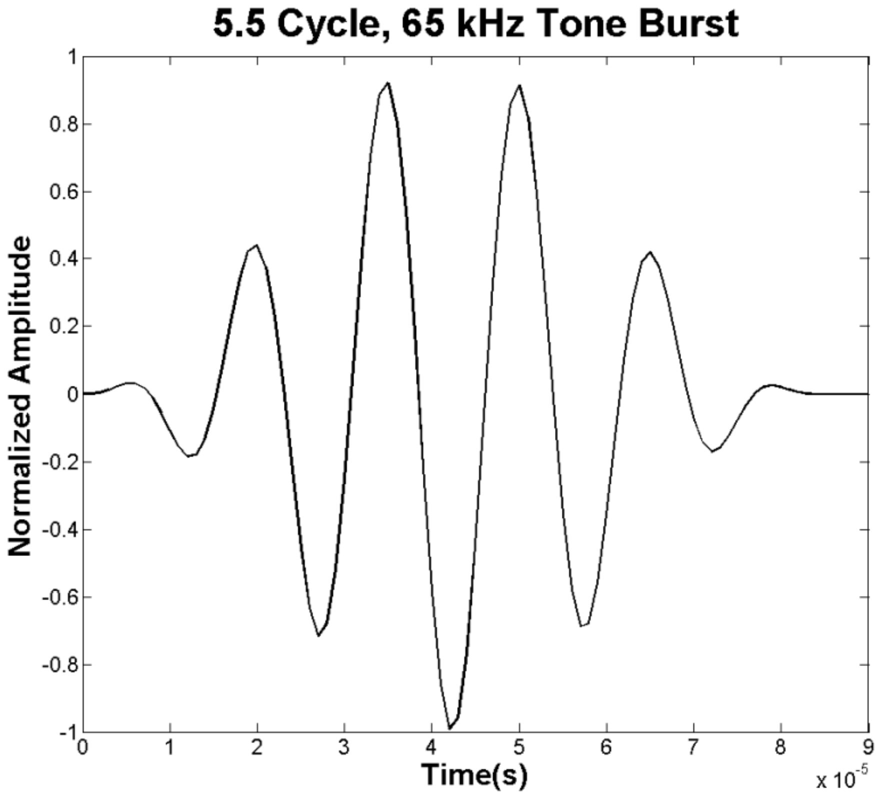

Figure 3.2 5.5 cycle 65 kHz tone burst excitation signal.

3.1.3 Mesh and Elements Used

The mesh was sized so that there were at least five elements in the thickness direction of each layer. The maximum distance been any two adjacent nodes was thus set to 0.15mm. The elements used were 2D deformable, plain strain linear quadrilaterals with reduced integration. Approximately 26000 elements were generated on the structure and a dynamic implicit type analysis was run to observe the wave generation and propagation through the structure. The mesh generated around the damage is as shown in Fig. 3.3.

3.1.4 Modelling Damage

Damage was modelled as a crack or void – no material in the section. The size of the damage was 1.27cm and the position of the damage was in the middle of the adhesive layer. Fig. 3.4 shows the size and position of the damage in the joint.

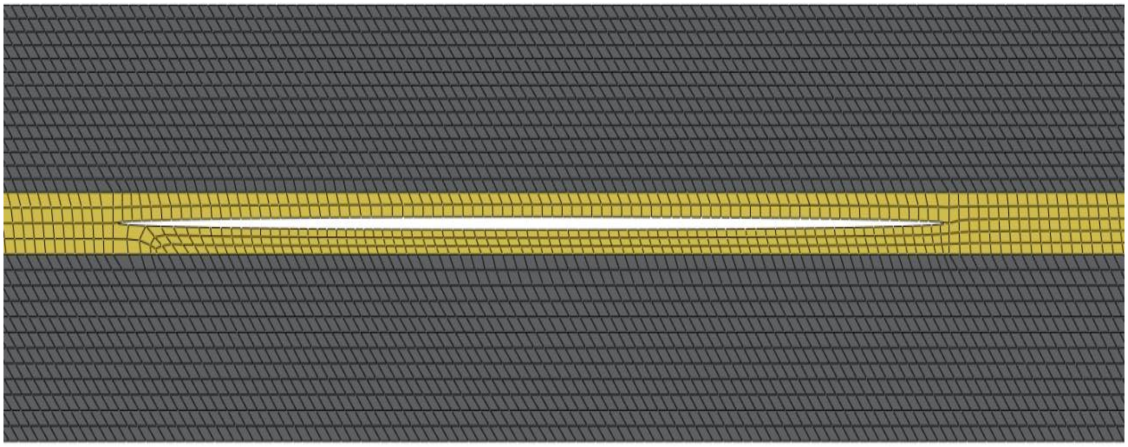

Figure 3.3 A zoomed in image of the mesh generated around the damaged region

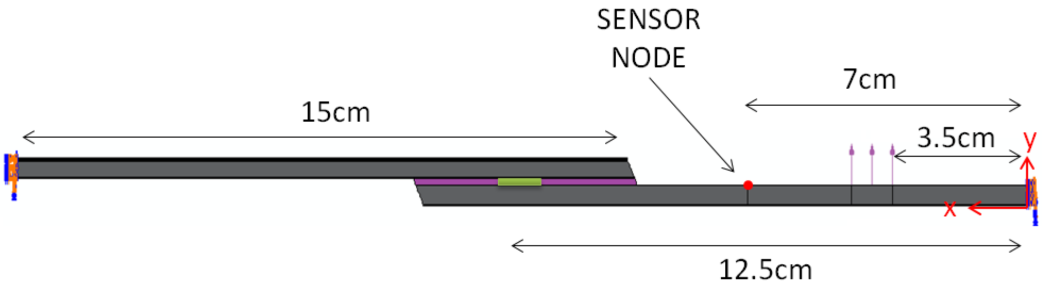

Figure 3.4 The geometry of the lap joint with damage modeled in the adhesive layer. Image not to scale.

3.1.5 Wave Propagation

As seen in Fig. 3.5, the simulations clearly showed the A_0 wave generated and traversing the lower plate. The wave propagated through the entire structure with little attenuation as there was no user defined damping employed in the simulation. The simulated waves are straight crested waves since the 2D model assumes an infinitely wide plate (thus the use of plain strain elements).

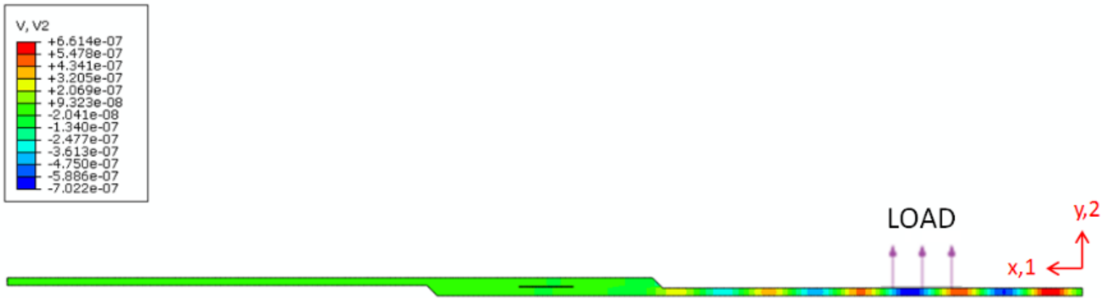

Figure 3.5 Wave propagation in the 2D model.

The wave propagates in both the left and right directions from the excitation section.

The wave velocity calculated from the simulation was validated using DISPERSE (Lowe & Pavlakovic, 2013) as seen in Fig. 3.6. The wave velocity was calculated by determining the time of flight of the wave to reach a certain checkpoint and was estimated to be approximately 2,650 m/s. The software also validated that the wave was indeed the A_0 mode. This was expected since the excitation was in the transverse direction.

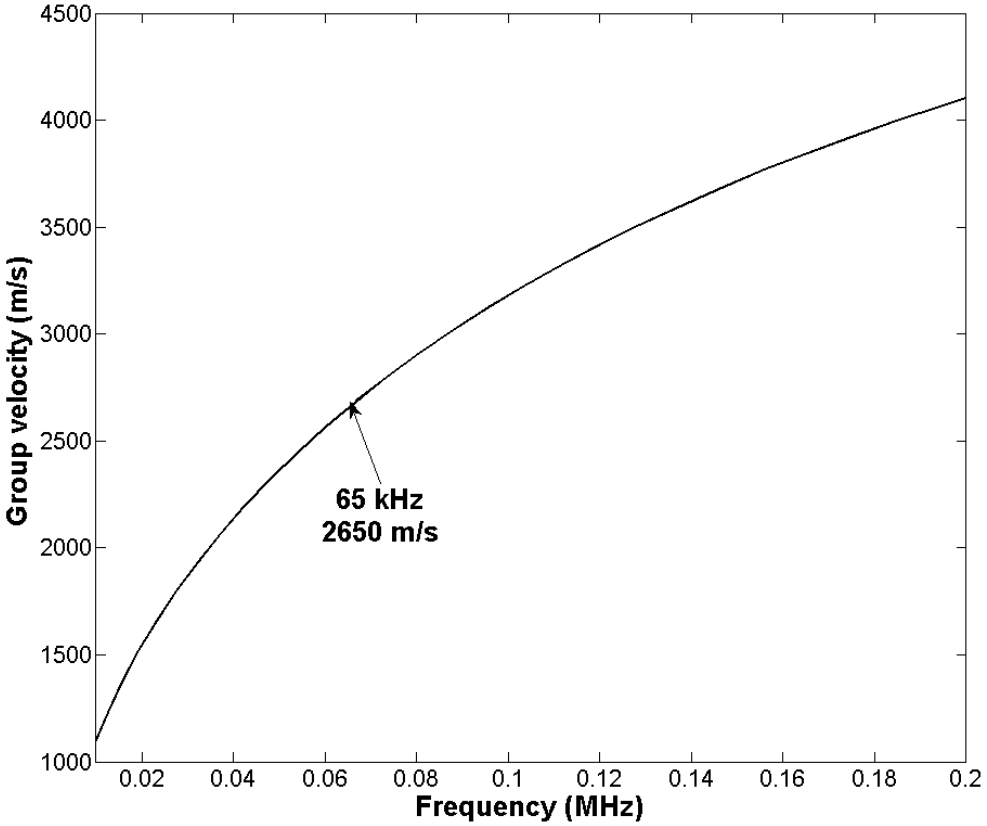

Figure 3.6 Dispersive properties of the A_0 wave in the 1.8mm thick [0/0/0/0] composite plate generated using DISPERSE.

The predicted group velocity corresponding to the excitation frequency of 65 kHz is 2,600 m/s

3.1.6 Comparison of Structural Responses

The response of the structure was recorded at the sensor node as seen in Fig. 3.4. The structural response waveforms of the baseline and damaged specimens to the tone burst excitation were then superimposed one over the other to determine at what point in time the waveform from the damaged specimen began to deviate from the waveform of the baseline specimen. This time instant was assumed to be the total time of flight of the wave from the load/excitation point to the damage and back to the sensor node.

The time of flight of the wave to and from the damage, multiplied by the velocity of the A_0 wave is the sum of the distance between the applied load and the damage, plus the distance between the damage and the sensor point. This distance as seen in Fig. 3.4 is 14cm. Fig. 3.7 shows the baseline and damaged structural response waveforms and the time of flight estimate. The time of flight recorded for the Lamb wave that reflected off the damage was 5.2 x 10^{-5} seconds. The predicted distance was 13.78cm as determined in Eqn. 3.1.

$$d = V * tof = 2650 * 5.2 * 10^{-5} = 13.78cm \tag{3.2}$$

d is the predicted distance between the PZT to the damage and back to the sensor, *V* is the velocity of the A_0 wave and *tof* is the time of flight of the Lamb wave to travel from the excitation point to the damage and back to the sensor. The predicted distance derived from the time of flight is extremely close to the actual distance modeled in ABAQUS. The difference between the actual and predicted responses can be reduced further by increasing the deviation between the two structural responses. This can be achieved by increasing the excitation frequency, but the PZTs have an excitation limitation of approximately 100 kHz.

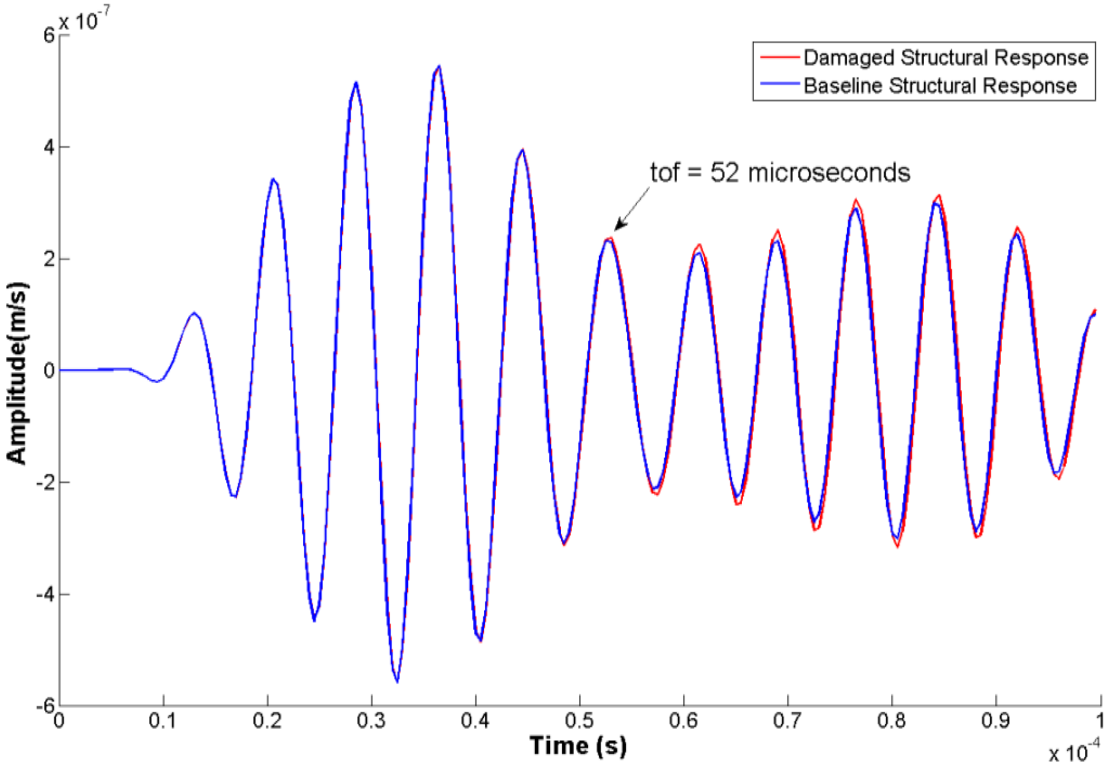

Figure 3.7 Determining time of flight of the lamb wave to and from the damage site.

As seen in Fig. 3.7, the difference between the baseline and damaged waveforms is very small, but as will be discussed in Section 4.5 which deals with the repeatability of experiments, the difference in amplitude at the time at which the damaged waveform starts to deviate from the baseline is greater than the operational scatter of the vibrometer (sensing element).

3.2 3D Finite Element Simulations of a Lap Joint to Triangulate Damage

The 3D model created was more detailed than the 2D model. The major differences in the details added were:

1. The composite laminate was modeled using a composite section based lamina definition as opposed to an isotropic section.
2. The PZT element was included in the simulation. The PZT element behaves like an additional material boundary giving rise to a more complex structural response which more closely models the physical structure.
3. The excitation signal was excited using the PZT element leading to more realistic circular crested Lamb waves as opposed to straight crested Lamb waves in the 2D simulations

The 3D model was also used to validate the entire triangulation methodology beginning from determining the time of flight of the damage reflection, creating damage loci and finally, generating the DI plot. The case presented below is to demonstrate the capability of the methodology to detect damage beyond the lap joint.

3.2.1 Geometry

The geometries considered for the simulations were two 25cm long, 7.5cm wide $[0/90/0/90]_s$ unidirectional laminates with a 5.08cm lap joint. The thickness of each lamina was assumed to be 0.45mm and the thickness of the adhesive layer was assumed to be 0.635mm. The material section for this simulation was assumed to be a thin composite lamina based on ABAQUS's composite section library. The material properties considered for the AS4 8552 unidirectional plies are in table 3.1. The adhesive assumed was Henkel Hysol EA 9309.3NA, a two part epoxy resin with an isotropic Young's modulus of 127 MPa, Poisson's ratio of 0.3 and a density of 1200 Kg/m^3. Fig. 3.8 shows the geometry of the lap joint along with the boundary conditions and loads.

Table 3.1 Material properties of unidirectional composite lamina

Property	Value
E_{11}	125.48 GPa
E_{22}	8.41 GPa
ν_{12}	0.31
G_{12}	4.22 GPa
G_{13}	4.22GPa
G_{23}	4.22 GPa
ρ	1525 kg/m^3

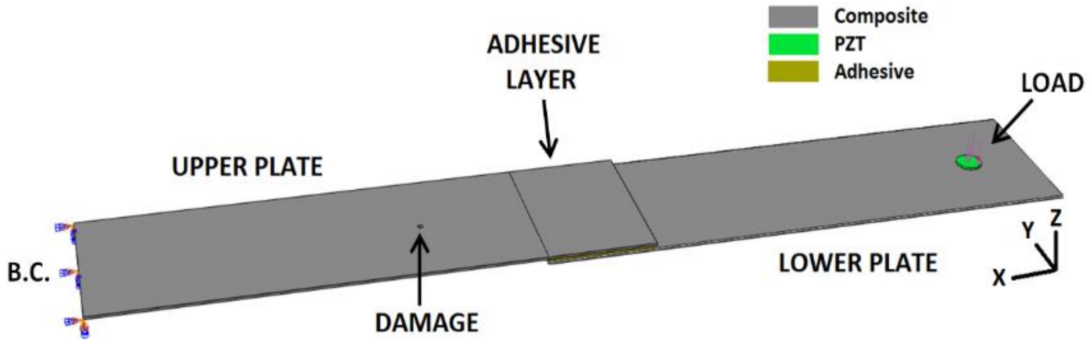

Figure 3.8 The layout of the 3D model.

The ‘Encastre’ boundary conditions are visible on the left and the load application is visible on the PZT.

3.2.2 Boundary Conditions and Loads

As seen in Fig. 3.8, the left face of the upper composite plate was constrained completely in both displacement and rotation. The boundary condition is referred to as “Encastre” in ABAQUS. The excitation signal was a four cycles, 40 kHz tone burst and was excited as a transverse pressure on the upper face of the PZT element as seen in Fig. 3.8. The MATLAB code used to generate the tone burst is in Appendix B.

3.2.3 Mesh and Elements Used

The composite plates were modeled using linear 3D deformable 2D shell elements. Shell elements have no thickness and are used to model structures whose one dimension is less than 1/10 of the other smallest dimension. A conventional shell element by default is modeled so that it lies in the middle of the apparent thickness of the plate. To correctly model the plates so that the elements were on the surface, the upper plate elements were offset to the bottom of the plate and vice versa. Fig. 3.9 shows the cross-section of the 3D structure in which the 'thickness' of the shell elements has been rendered.

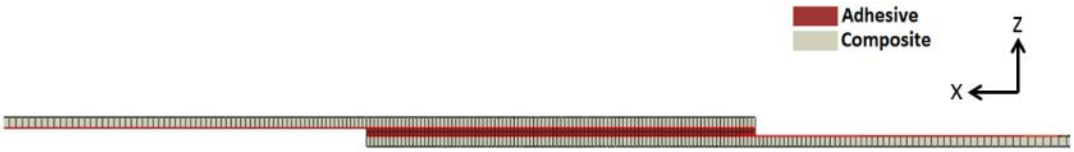

Figure 3.9 The cross-section of the lap joint.

The rendered thickness of the plates is visible in grey and the adhesive in red.

The adhesive and PZT were modeled using linear, 3D stress elements. Care was taken to ensure that the adhesive layer was at least two elements thick. This was because of the technique used to assemble the model. The adhesive layer was attached to the composite plates using master-slave type 'tie' surface constraints. These constraints tie the displacements of the slave nodes to those of the master nodes by making the slave nodes displace and rotate exactly as the master nodes do. If the adhesive layer was only one element thick, the lower nodes of the adhesive layer would move with the lower plate and the upper nodes of the adhesive would move with the upper plate. This would imply that the elements of the adhesive layer were essentially just mimicking the properties of the composite plates and not the properties of the isotropic adhesive that they have been assigned. They would essentially have modeled a perfect interface between the two plates. This is why the adhesive layer needed to be at least two layers thick.

The PZT on the other hand only had its lower surface constrained to the composite and was thus modeled using only a single layer of elements. The model was composed of 31,263 shell elements with 31608 nodes per composite plate, 30,000 3D stress elements with 45350 nodes in the adhesive layer and 44 3D stress elements with 110 nodes in the PZT. Fig. 3.10 shows the PZT and adhesive layer 3D meshes.

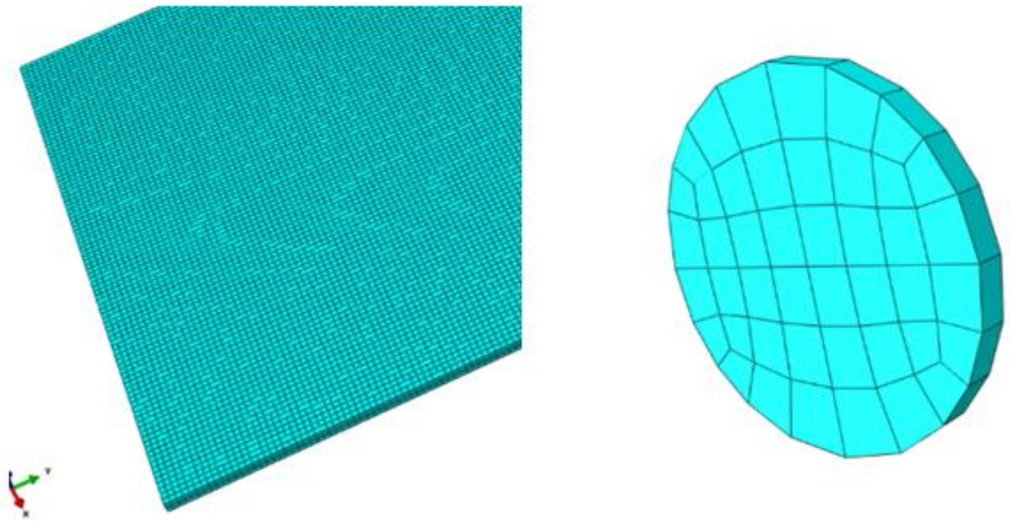

Figure 3.10 The mesh of the adhesive layer (left) and the PZT element (right). The meshes are not to scale.

3.2.4 Modeling Damage

Damage was modeled as a circular void (no material in the section) in the upper plate. The size of the damage was 2.5mm in diameter and the position of the damage was in the upper plate, 5cm away from the lap joint along the x-axis. This simulation was to prove that the system was capable of sensing damage even beyond the lap joint. Fig. 3.11 shows the location of the damage in the plate. The damage was created 30cm away from the right edge of the model along the x-axis.

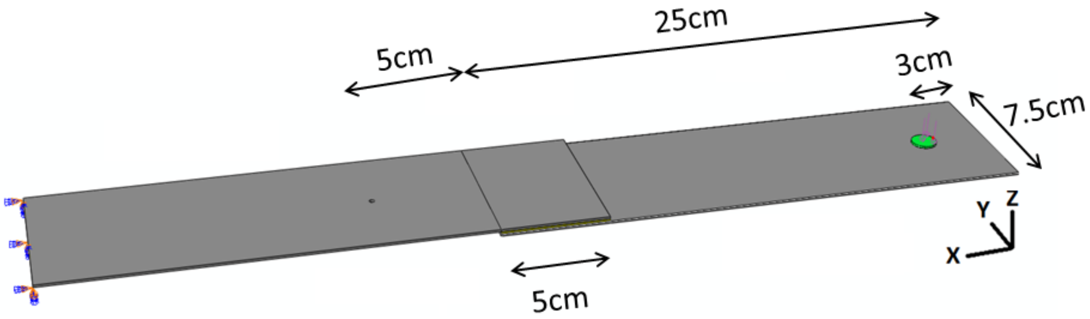

Figure 3.11 The relative distances between each part of the assembly.

3.2.5 Post-Processing

The simulation was executed using a dynamic explicit solver in ABAQUS. The A_0 wave generated by the PZT propagated in all directions, but due to the slowness characteristics and geometry of the structure, the wave propagating along the x-axis was the strongest and fastest wave. Since the excitation is transverse to the plane of the plate (z-axis is called axis3 in ABAQUS), the ABAQUS simulations are plotted using the variable *V3*. *V3* is the out of plane velocity recorded at the nodes. Figs. 3.12 to 3.14 show the propagation of Lamb waves in the baseline model as they are generated by the PZT, propagate through the lower plate and experience partial reflection back into the lower plate, and partial transmission to the upper plate, at the lap joint boundary.

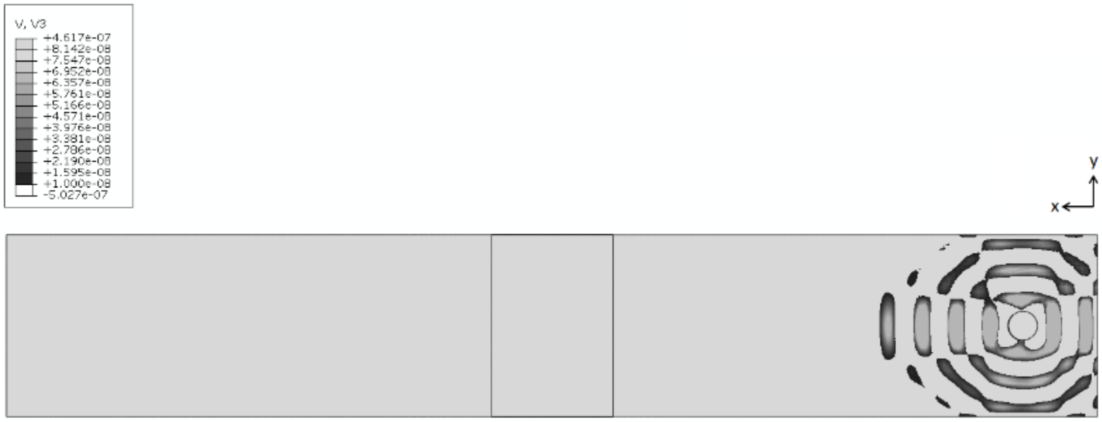

Figure 3.12 Wave propagation in the composite plate

The A_0 wave generated by the PZT travels in all directions. The strength and speed of the wave along the x-axis is greatest.

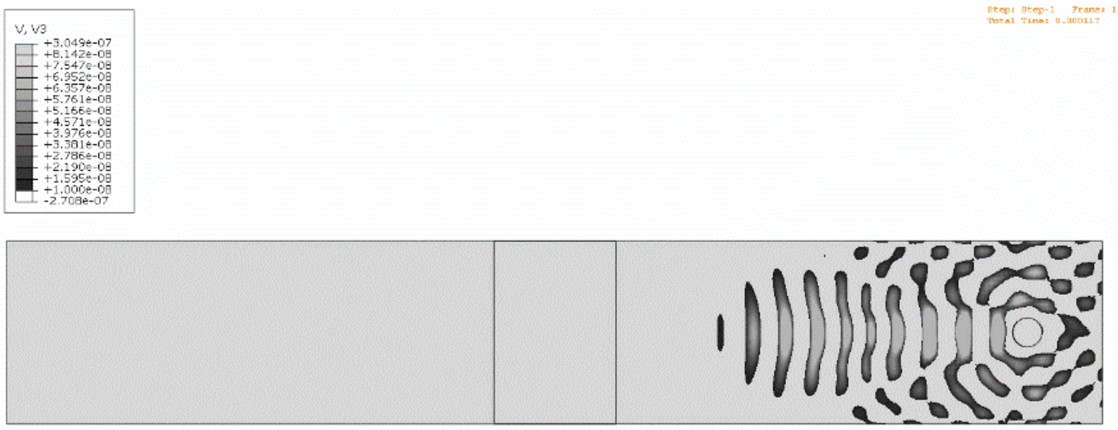

Figure 3.13 The A_0 wave generated by the PZT travelling in the lower composite plate.

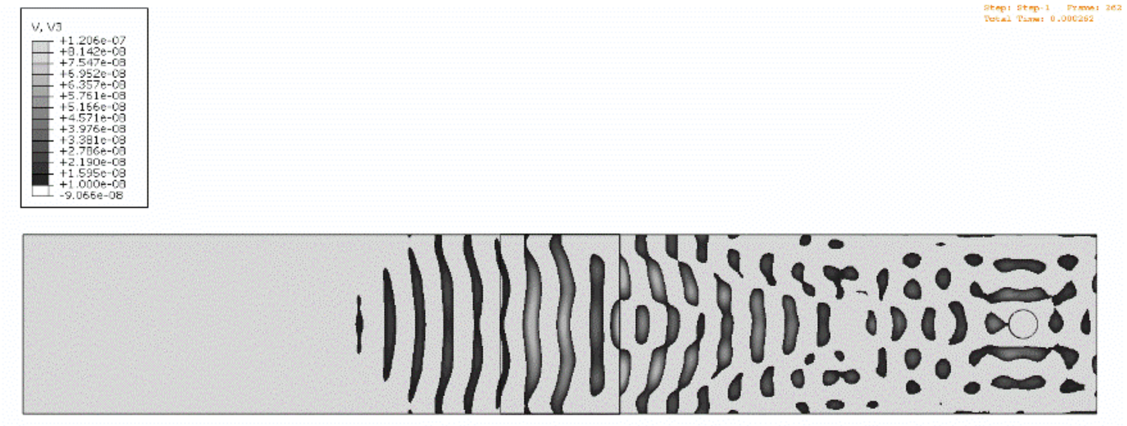

Figure 3.14 Transmission of Lamb wave through the adhesive lap joint

The A_0 wave has transferred a part of its energy through the adhesive into the top plate (left). The rest of the energy is reflected back into the lower plate towards the PZT (right).

3.2.6 Extracting Time of Flights

The time of flight of the wave from the PZT to the damage and back from the damage to the sensory location was extracted from three sensory locations around the PZT. The three sensory locations as shown in Fig. 3.15 are at nodes 158, 92 and 202. The variation of transverse velocity of the nodes (V3 or out of plane velocity) over time was recorded at these three nodes to record the response of the structure. These three nodes were chosen as they mimic the approximate interrogation locations that would be chosen in the experiments.

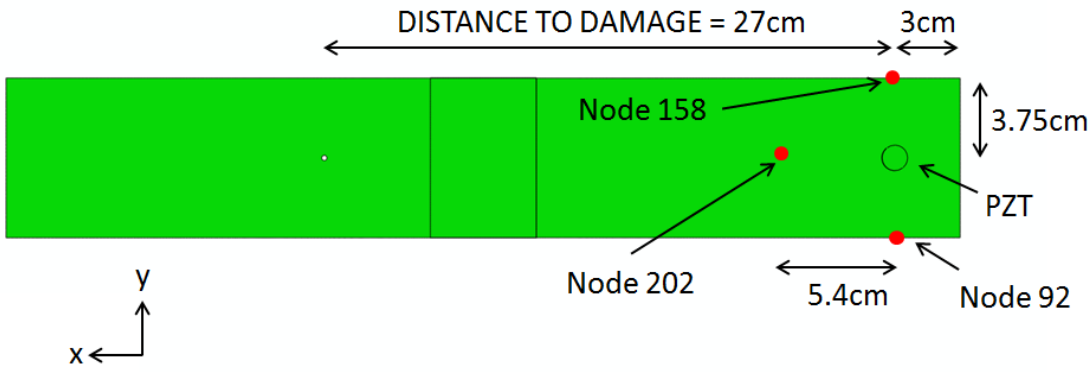

Figure 3.15 Three sensory nodes 158, 202 and 92 on the model.

The time of flight of the Lamb wave from the PZT to the damage and back to each of these sensor points is determined to conduct damage triangulation

The structural response to the four wave 40 kHz tone burst is shown in Figs. 3.16 to 3.21. The healthy and damaged structural responses recorded in terms of the transverse velocity at the three sensor points are superimposed to determine the initial time of deviation between the two responses. This initial time of deviation is the time of flight of the wave from the PZT to the damage and back to the respective node (sensor position). The times of flight recorded at each node and its (x, y) coordinates with respect to the PZT (origin) are tabulated in table 3.2.

Table 3.2 The times of flight evaluated for each sensor node

Sensor No.	Node No.	X,Y Coordinates of node w.r.t. PZT (cm)	Time of Flight (s)
1	92	0 , -3.75	0.00057
2	158	0 , 3.75	0.00057
3	202	5.3 , 0	0.00051

The time of flight of the wave recorded at node 202 is less than those recorded at nodes 92 and 158 because the distance travelled by the wave as it propagated from the PZT to the damage and back to node 202 is less than that for nodes 158 and 92.

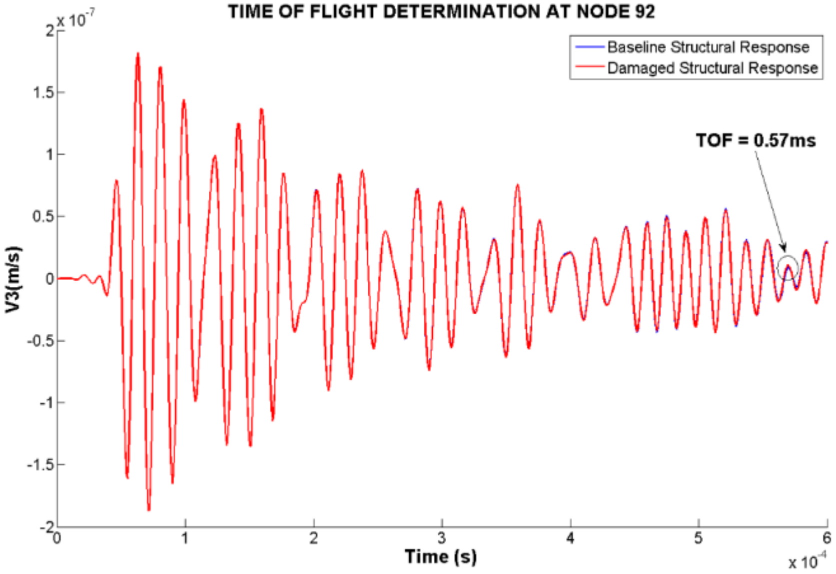

Figure 3.16 The baseline and damaged structural response recorded at node 92

The waveforms are superimposed on each other to determine the first point of deviation between the two waveforms. Fig. 3.17 shows a blown up section of this plot in which the start of deviation is visible at 0.57ms.

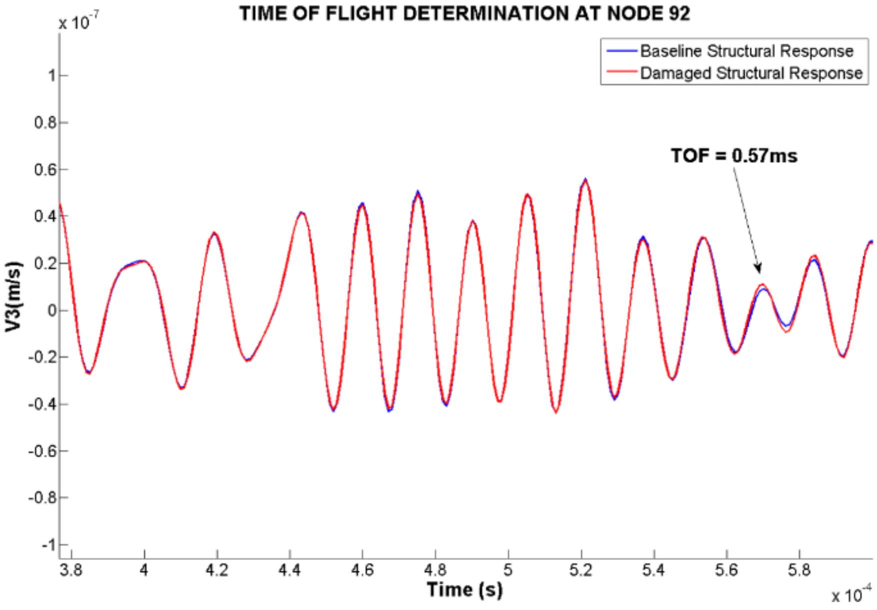

Figure 3.17 Blown up section of the structural responses recorded at node 92

Fig. 3.17 indicates that the damaged waveform begins deviating from the baseline response at 0.57 milliseconds

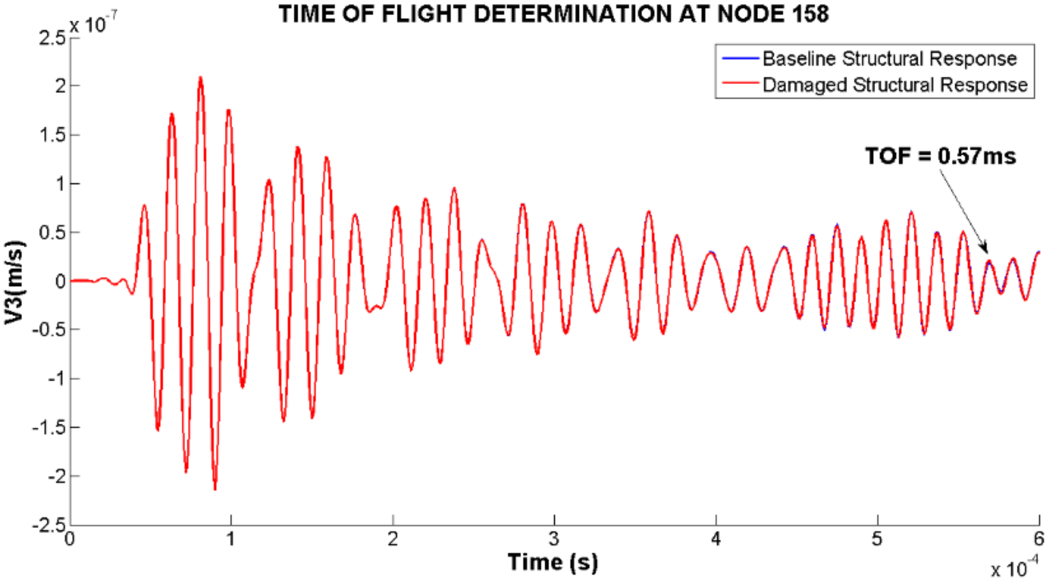

Figure 3.18 The baseline and damaged structural response recorded at node 158

The waveforms are superimposed on each other to determine the first point of deviation between the two waveforms. Fig. 3.19 shows a blown up section of this plot in which the start of deviation is visible at 0.57ms.

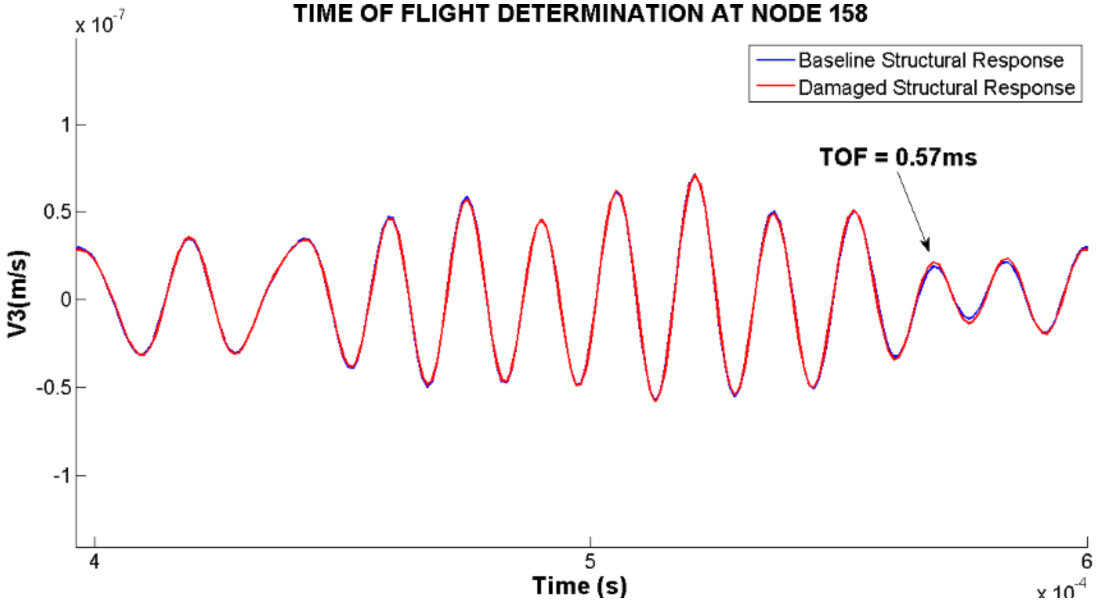

Figure 3.19 Blown up section of the structural responses recorded at node 158

Fig. 3.19 indicates that the damaged waveform begins deviating from the baseline response at 0.57 milliseconds

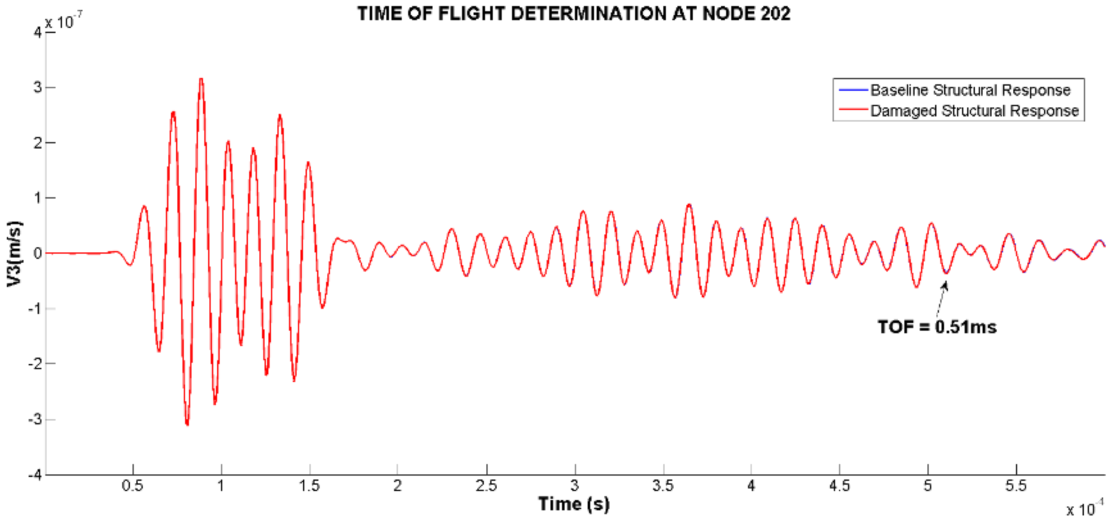

Figure 3.20 The baseline and damaged structural response recorded at node 202

The waveforms are superimposed on each other to determine the first point of deviation between the two waveforms. Fig. 3.21 shows a blown up section of this plot in which the start of deviation is visible at 0.51ms.

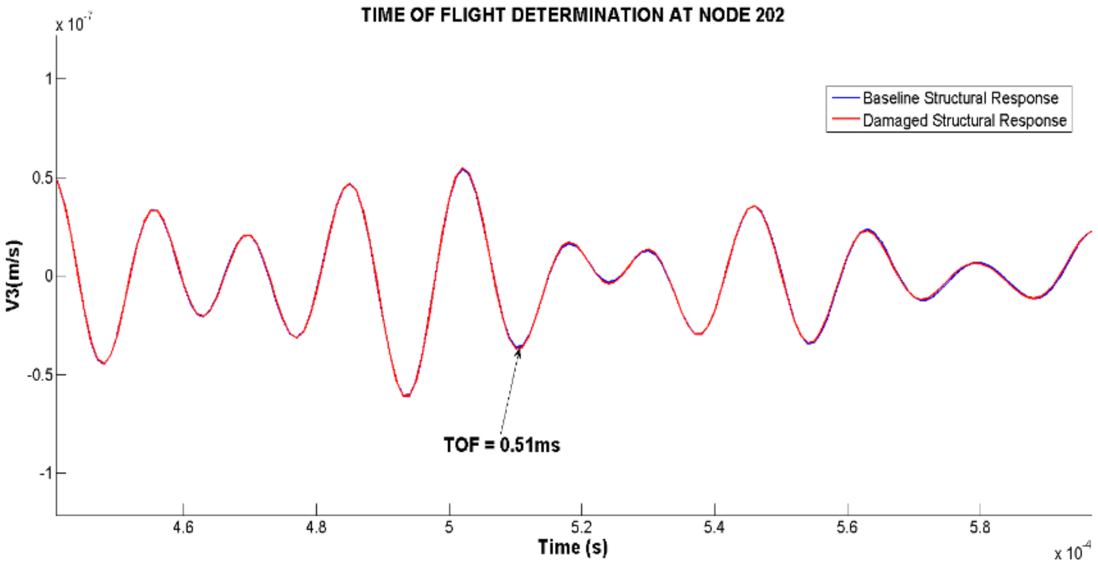

Figure 3.21 Blown up section of the structural responses recorded at node 202

Fig. 3.21 indicates that the damaged waveform begins deviating from the baseline response at 0.51 milliseconds

3.2.7 Triangulation

The damage location was triangulated using data from the three sensor nodes by following the algorithm specified in chapter II. The inputs to the damage triangulation program were the times of flight of the wave from the PZT to the damage and back to the respective sensor (node), the coordinates of the three sensors nodes with respect to the PZT, and the velocity profile of the Lamb wave in the modeled laminate. The program, written in MATLAB, is attached in Appendix A. The program generated the triangulation data in the form of three damage prediction loci, each of which corresponded to one sensor-PZT pair. The region in which the three loci collectively approach each other the closest is where the probability of the reflection from the damage is highest. The damage prediction loci are plotted in Fig. 3.22. The area in the loci plot that included the physical model was subdivided into a number of grid points at which a damage index value was computed based on the proximity of the grid point to each of loci. The grid point at which all the three curves are the closest to it was determined to be the damage location. The damage index plot showing the point of highest probability of damage is plotted in Fig. 3.23.

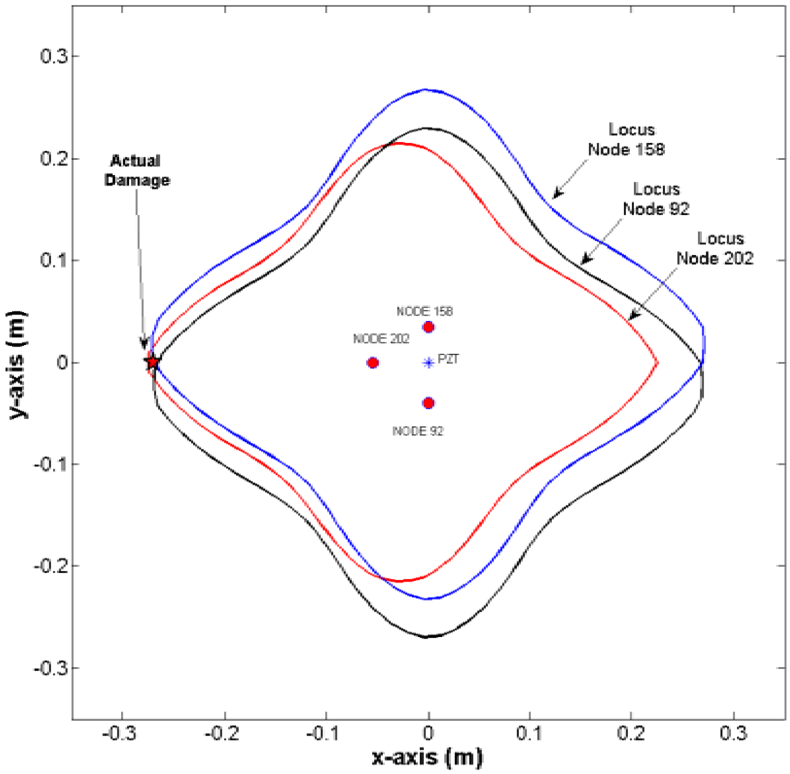

Figure 3.22 Damage loci plot for the FEA model.

The three damage loci generated from the nodes 92, 158 and 202 were used to triangulate the damage site.

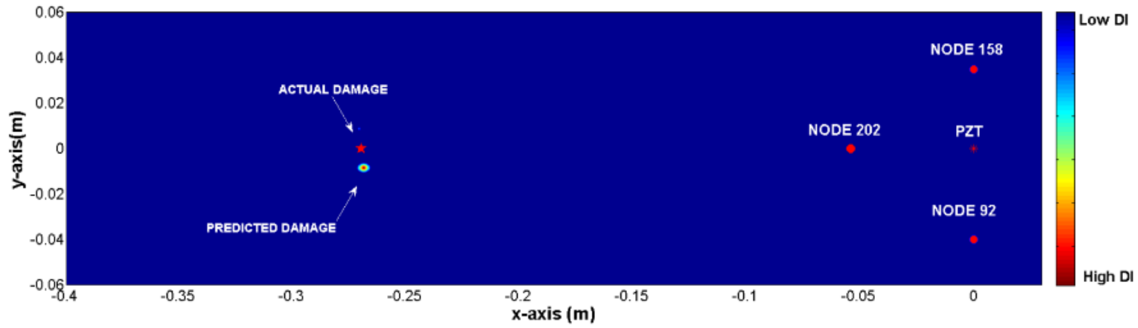

Figure 3.23 Damage index plot.

The point at which the three loci approach each other the closest has the highest DI value. The predicted damage is less than 2cm away from the actual damage.

CHAPTER IV

LAMB WAVE BASED SHM OF A LAP JOINT - EXPERIMENTAL STUDIES

The goal of the experimental study was to validate the methodology described in chapter II and its effectiveness in identifying the presence, locating and quantifying the extent of damage in an adhesively bonded composite lap joint. Two composite plates were fabricated out of carbon fiber unidirectional prepreg in-house. An adhesive lap joint was created between the two plates and a PZT actuator was mounted to one of the plates.

This chapter describes the:

- Fabrication of the composite structure
- Instruments used as a part of the actuation and sensing of lamb waves.
- Tuning of the excitation signal
- Damage infliction method
- Repeatability of experiments
- Detection of damage by comparing waveforms
- Assigning a damage index to quantify extent of damage
- Damage triangulation using the time of flight and damage index methods.

4.1 Fabrication of the Adhesively Bonded Composite Lap Joint

The two plates in the lap joint were constructed identically using a Hexcel HexPly carbon fiber based unidirectional prepreg. The fiber is AS4 in a 35% 8552 epoxy matrix.

The material properties of the prepreg are in table 4.1. The layup was the same as the one considered to create the 3D FEA model i.e. [0/90/0/90]s. The total thickness of the eight ply laminate was 1.27mm. The plate was 30cm long and 7.5cm wide. The adhesive used to create the 5.08cm long lap joint is Henkel Hysol EA 9309.3NA, a two part epoxy resin with an isotropic Young's modulus of 2.23 GPa, Poisson's ratio of 0.42 and a density of 1200 kg/m^3. Fig. 4.1 shows the two plates adhesively bonded together to create a lap joint. The laminates were cured using a vacuum bagging process in a temperature controlled curing oven. The cure cycle for the 8552 epoxy matrix is shown in Fig. 4.3.

Table 4.1 Material properties of cured AS4 / 8552 prepreg

PROPERTY	VALUE
E_{11}	125.48 GPa
E_{22}	8.411 GPa
$G_{12} = G_{13} = G_{23}$	4.23 GPa
ν_{12}	0.31
ρ	1525 kg/m^3

Figure 4.1 The adhesively bonded composite lap joint

Figure 4.2 The 5.08cm (2 inch) long lap joint

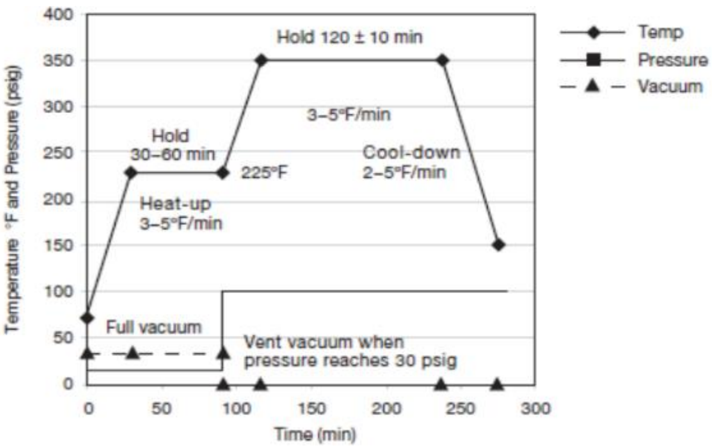

Figure 4.3 Recommended cure cycle for the 8552 epoxy matrix

(Hexcel Corporation, 2013)

4.2 Instrumentation and Hardware to Generate and Sense Lamb Waves

4.2.1 Signal Generation

The signal’s waveform was generated using a MATLAB code that is available in Appendix B. The program generates a sinusoidal tone burst by the user defining the number of cycles that the tone burst is expected to have, and the excitation frequency.

The MATLAB generated tone burst is defined in terms of ‘x, y coordinates’ with amplitude along the ordinate and time along the abscissa as seen in Fig. 4.6.

These coordinates were input into a waveform editor (Keysight, 2015) to further smoothen it since the discretization of the original signal was not sufficient to accurately model the tone burst if joined by linear interpolation, especially near the peaks. The editor was also used to generate a waveform file that was suitable to be stored in the memory of the waveform generator.

4.2.2 Signal Excitation

BenchVue (Keysight, 2015) was used to set the frequency and amplitude of the excitation waveform, along with the frequency at which the excitation occurred. The latter frequency is referred to as the ‘burst frequency’.

The waveform generator, an Agilent 33220A was used to create a variable voltage electronic signal. The signal was repeated every 500ms using a rising edge trigger. 500ms was deemed, through experiments, as a sufficient amount of time for the structural response from the previous excitation to subside completely.

The signal, which had a peak to peak voltage of 10 volts, was passed to a 20x voltage amplifier that boosted the signal voltage to 200 volts peak to peak. The amplified signal was transmitted to a 1.3cm diameter circular PZT element which deformed due to the piezoelectric effect and led to the formation of asymmetric Lamb waves.

4.2.3 Lamb Wave Sensing

Lamb waves were sensed using a laser vibrometer. The greatest advantage of using a laser vibrometer as a sensing element as opposed to a PZT was that it did not need to be mounted permanently to the structure. The vibrometer sensing location could be changed quickly to interrogate any part of the structure to record its response. The trigger from the signal generator was used as a recording trigger for the laser vibrometer. The vibrometer thus started recording data at exactly the same instant that the signal was excited. The response was averaged over 50 readings to remove noise. The scatter of the structural response recorded by the vibrometer from individual recordings is discussed in section 4.5. The data was recorded at a sampling rate of 2.56 MHz. The length of the recording was 1.6ms, which was deemed long enough to capture the relevant features of the structural response required to conduct damage identification. Figs. 4.4 and 4.5 show the process of generating, exciting and sensing as well as the actual setup as it looked when a response was being captured.

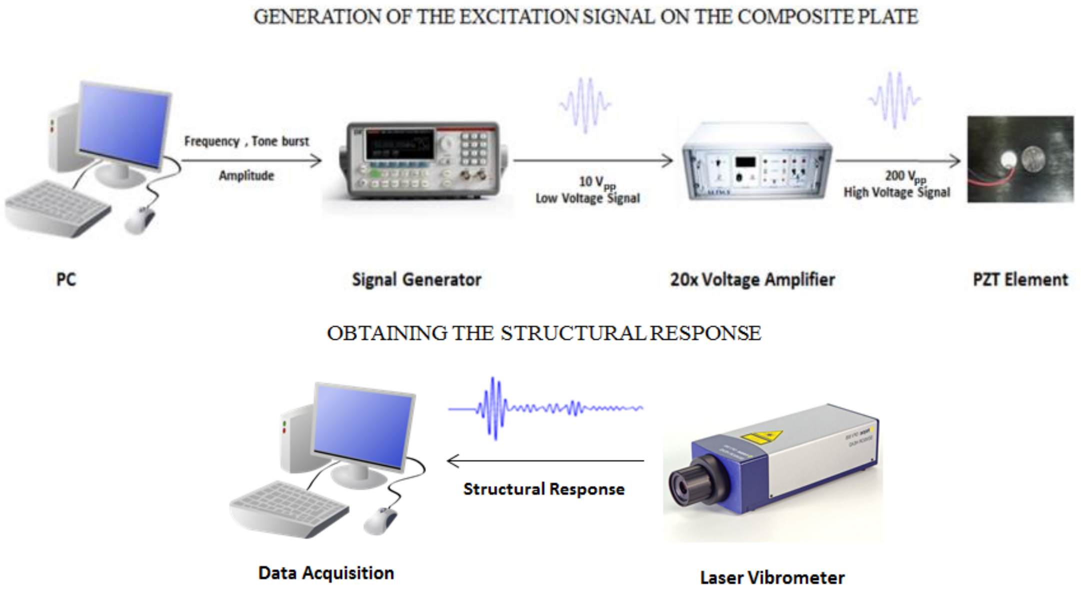

Figure 4.4 The generation, excitation and sensing of Lamb wave propagation

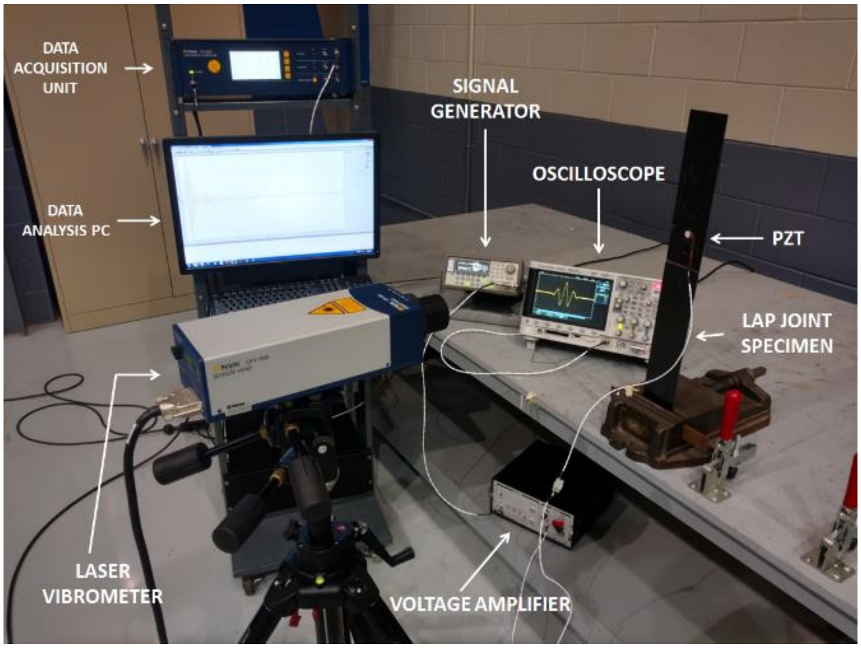

Figure 4.5 The experimental setup

The setup is used to generate the excitation signal, amplify it, excite the PZT and sense the resulting Lamb wave propagation

4.3 Tuning the Lamb Wave Signal

The excitation signal used in the experiments was a 5.5 cycle sinusoidal tone burst as seen in Fig. 4.6. Depending on the shape and size of the PZT, the amplitude of the Lamb wave modes vary with the excitation frequency. The maximum amplitude of the structural response recorded by the laser vibrometer is plotted as a function of the excitation frequency. The “sweet spot” or “tuned frequency” is the frequency at which the maximum amplitude of A_0 wave is greatest. Fig. 4.7 shows that the PZT is considered tuned at a frequency of 65 kHz for the 5.5 cycle tone burst.

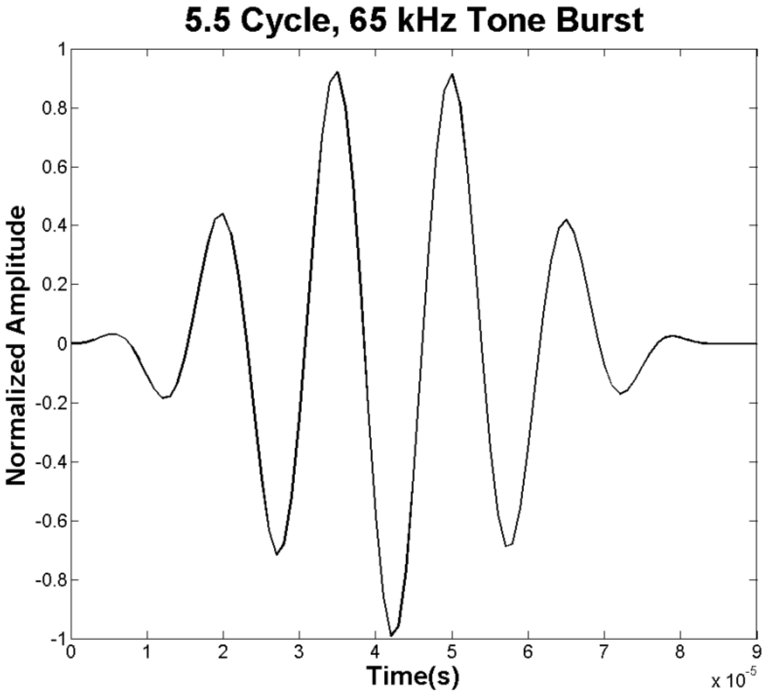

Figure 4.6 The excitation tone burst generated for experiments

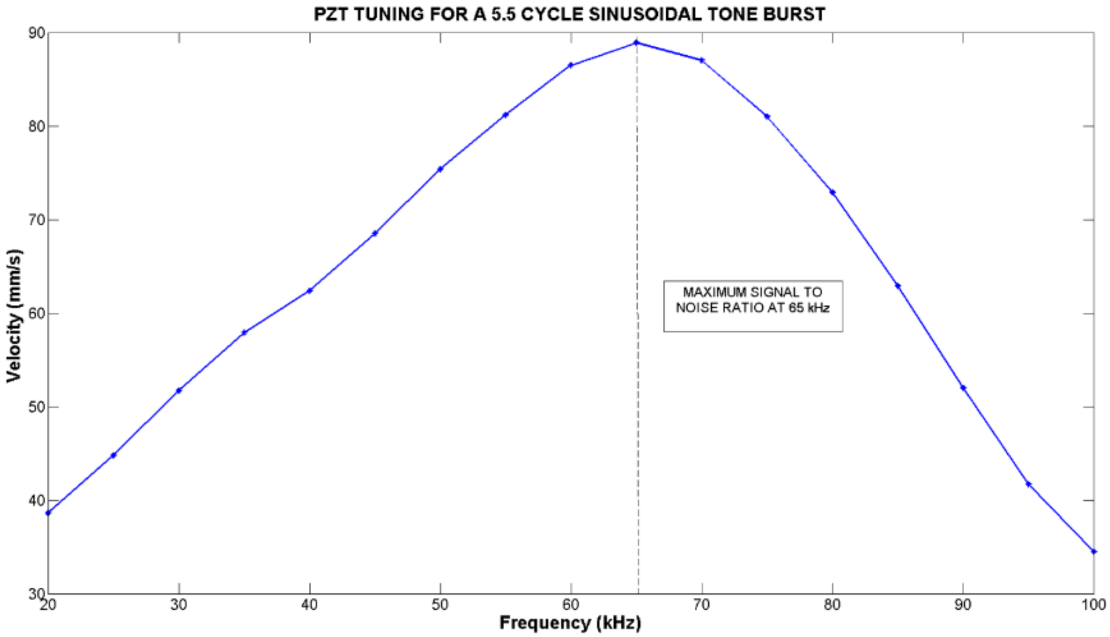

Figure 4.7 Tuning of the PZT indicates an A_0 sweet spot at 65kHz

4.4 Damage Infliction

Damage to the composite lap joint was inflicted using two methods. The first method was to simulate damage in the lap joint by creating an artificial material boundary with an aluminum coin. The second method was to inflict impact damage on the structure using a drop tower. The impact damage was inflicted at two points on the structure denoted as Site A and Site B as seen in Fig. 4.24. Site B, which lies in the middle of the adhesive lap joint, is also the site where the extent of damage was evaluated by dropping the impactor on it three times.

4.4.1 Damage Infliction Using a Circular Metal Plate

A coin shaped circular aluminum plate stuck on the surface of composite plate was used to create a material boundary as seen Fig. 4.8. This coin behaves as an artificial damage site since it reflects A_0 waves (highly sensitive to surface damage) in a very similar manner to actual surficial damage. The coin was adhered to the composite surface using 3M 467 MP, a double sided, flexible temporary adhesive.

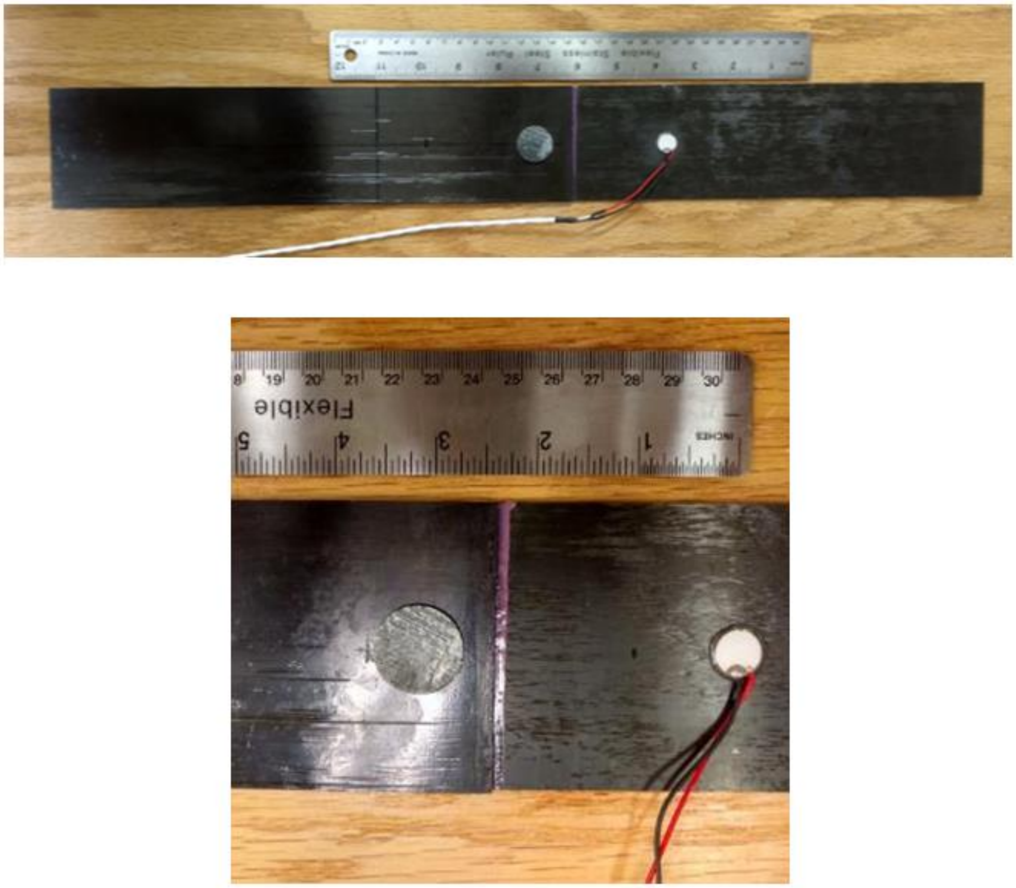

Figure 4.8 The simulated damage on the composite lap joint

The coin is placed in the lap joint on the upper plate. The PZT is on the lower plate (top). A close-up of the lap joint shows the relative distance of 8cm (3.5 inches) between the PZT and the coin (bottom).

4.4.2 Damage Infliction Using a Drop Tower Impactor

Actual damage was inflicted on the structure using a drop tower as seen in Fig. 4.9. The impactor has a 6.35mm diameter hemispherical head, weighs 910 grams and is made of steel. The aim was to inflict barely visible impact damage (BVID) on the lap joint specimen. The impactor was dropped from varying heights on a sample specimen piece to determine the correct height at which BVID damage was attained. The BVID could be sensed by touch, but was not discernible to the naked eye. The impactor was thus dropped from a height of 40cm. The energy expelled in the drop test is thus:

$$Energy = m * g * h = 0.91 * 9.81 * 0.4 = 3.57\, Joules \tag{4.3}$$

m is the mass of the impactor, g is the acceleration due to gravity and h is the height from which the impactor was dropped.

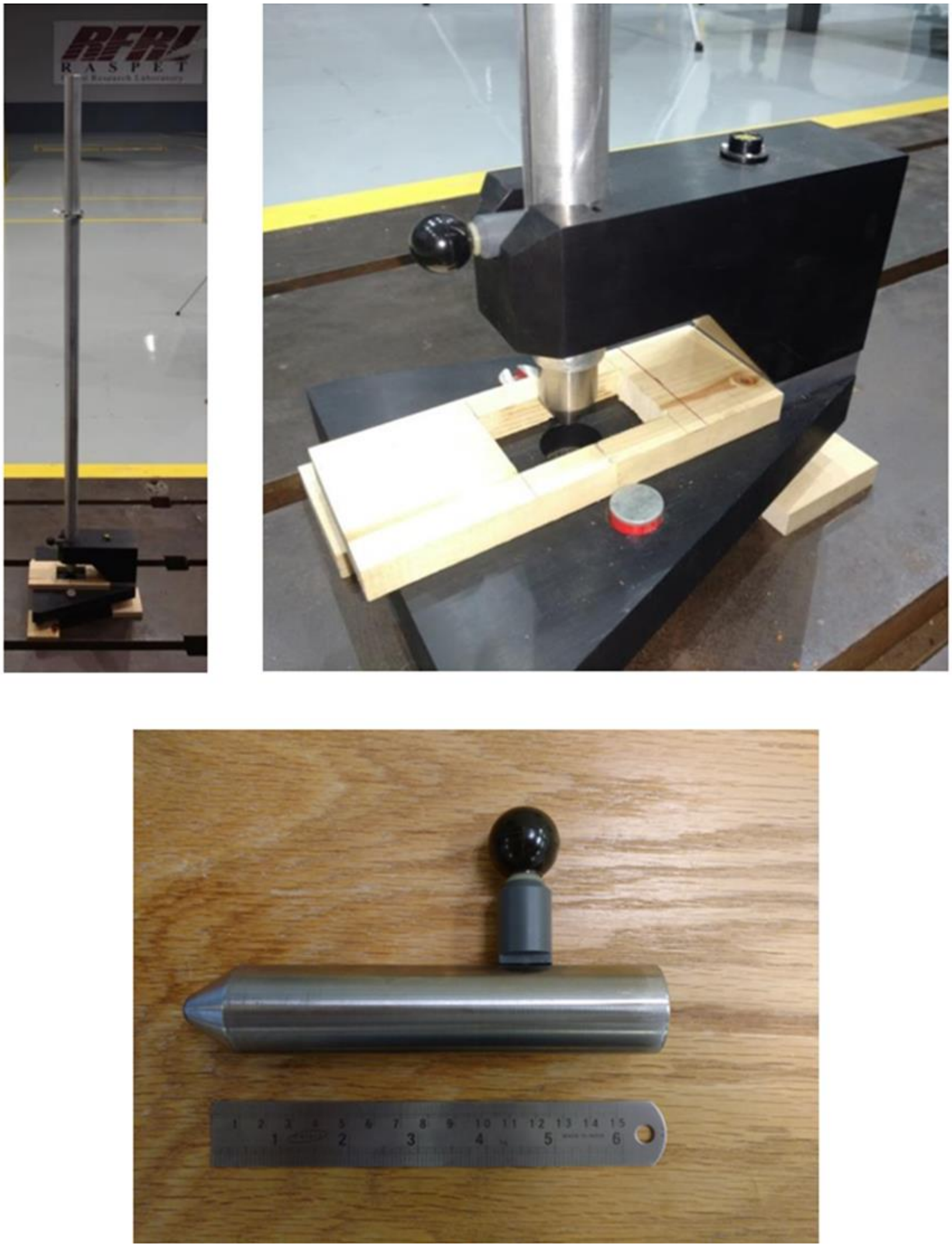

Figure 4.9	The drop test impactor

The machine (top-left) and the impactor sitting above the base (top-right). The impactor (bottom) weighs 910 grams (2 lbs.).

4.5 Repeatability of Experiments

The time of flight method works by identifying the initiation of deviation of the damage structural response from the healthy structural response. To ensure that noise was not mistaken as a deviation, a point on the structure was interrogated ten times to ascertain the uncertainty that could be attributed to noise. Figs. 4.10 and 4.11 show that the scatter in experimental data is extremely small. As seen in Fig. 4.11, the normalized scatter in amplitude recorded at one of the troughs was 0.78 x 10^{-4}. Therefore any consistent deviation between the normalized baseline and damaged structural response waveforms could be attributed to a reflection from the damage.

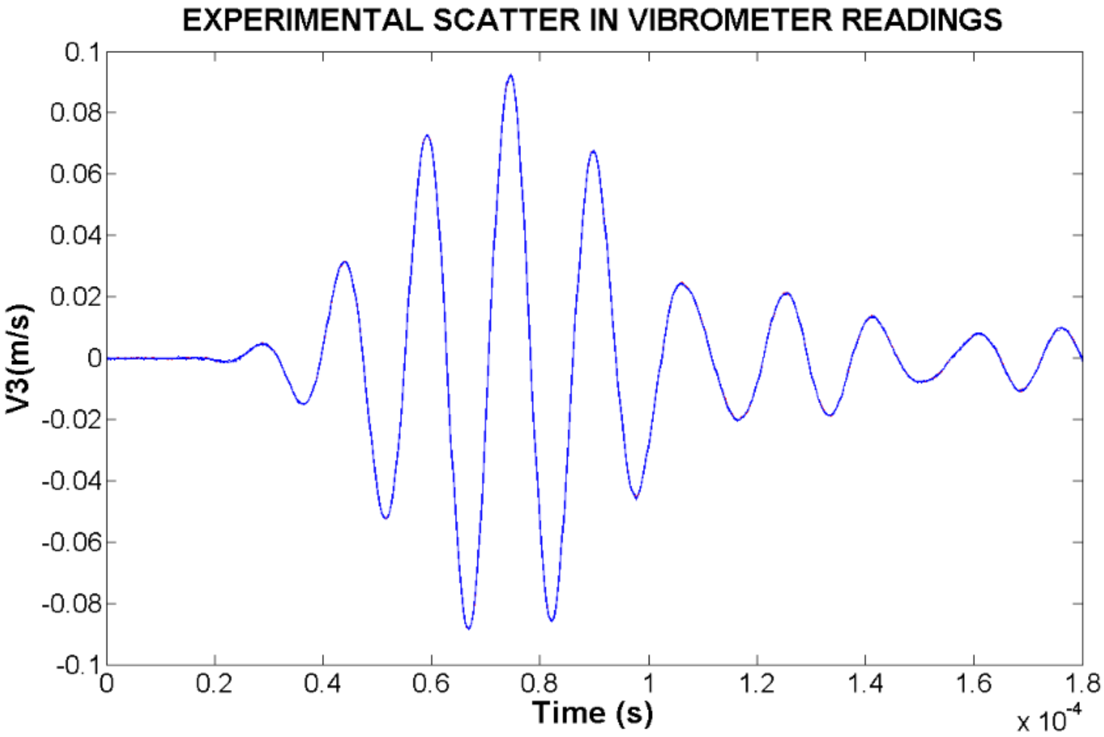

Figure 4.10 Experimental scatter

The responses of 10 vibrometer readings are superimposed to determine the scatter of noise in the readings. The plot shows that there is negligible amount of scatter between readings.

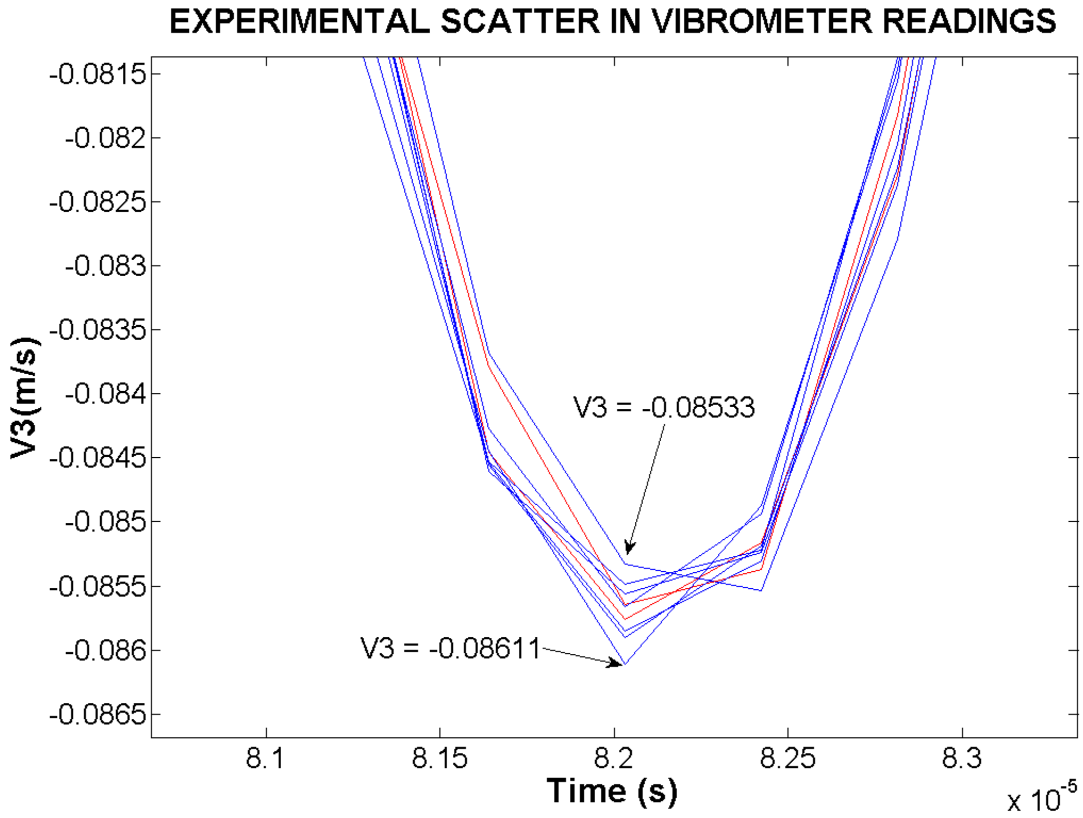

Figure 4.11 Close up of one of the troughs in Fig. 4.10

The scatter is calculated as the vertical distance between the two most scattered signals.

4.6 Damage Detection

The first goal of SHM is to successfully detect the onset of damage. A set of experiments was conducted to ascertain whether it was possible to detect if the lap joint had been damaged or not. The method employed was to sense the waveform on the plate without the PZT, beyond the lap joint region as shown in Fig. 4.12. The lap joint was damaged three times on the same spot using the drop tower with the impactor dropped from 0.4m. The third time it was damaged, the lap joint experienced catastrophic failure. Both the upper and lower plates exhibited visible delaminations. The adhesive holding the lap joint together failed.

The structural response waveform of the damaged specimen is expected to deviate from the baseline waveform as soon as the waves are sensed by the vibrometer. This is because the damage lies on the shortest path between the PZT and sensor. The wave-front generated by the PZT travels through the damage and reaches the sensory point before any reflections do. The experimental results in Fig. 4.13 show the structural responses from the damaged specimen deviate as soon as the wave is sensed by the vibrometer.

As the amount of damage in the lap joint increased, the amount of energy transmitted back towards the PZT by the damage increased. This resulted in a drop in the amplitude of the first wave packet that passed through the sensory point. The damage after the third impact was so severe that it caused extremely high signal attenuation in the upper plate with most of the energy of the wave being reflected back towards the PZT. The wave is first sensed at approximately $1\text{x}10^{-4}$ seconds. The time span of the first wave packet t_S can be determined as the ratio of the number of cycles in the excitation signal N_C and its frequency f. Fig. 4.13 plots only the first wave packet.

$$Duration\ of\ first\ wave\ packet = \frac{N_c}{f} = \frac{5.5}{65000} = 0.085\ milliseconds \qquad (4.2)$$

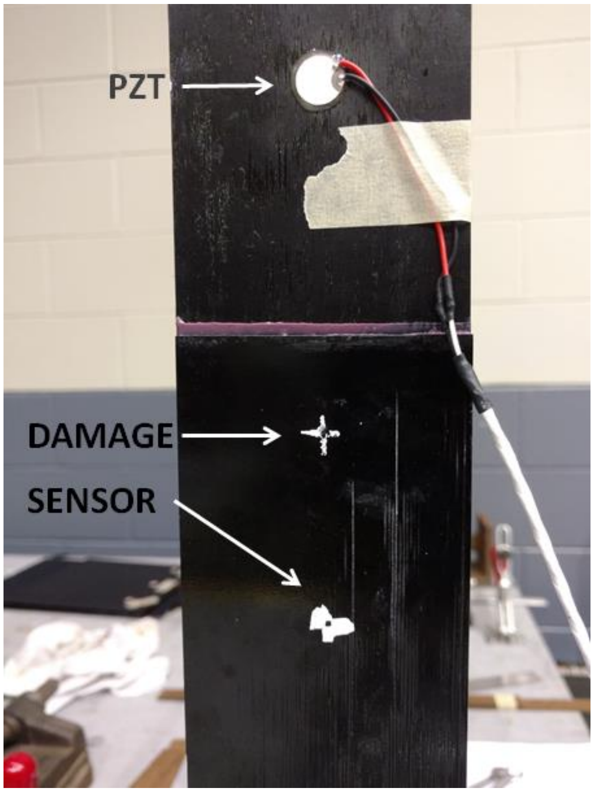

Figure 4.12 The layout of the damage, PZT and sensory location for the damage detection experiments

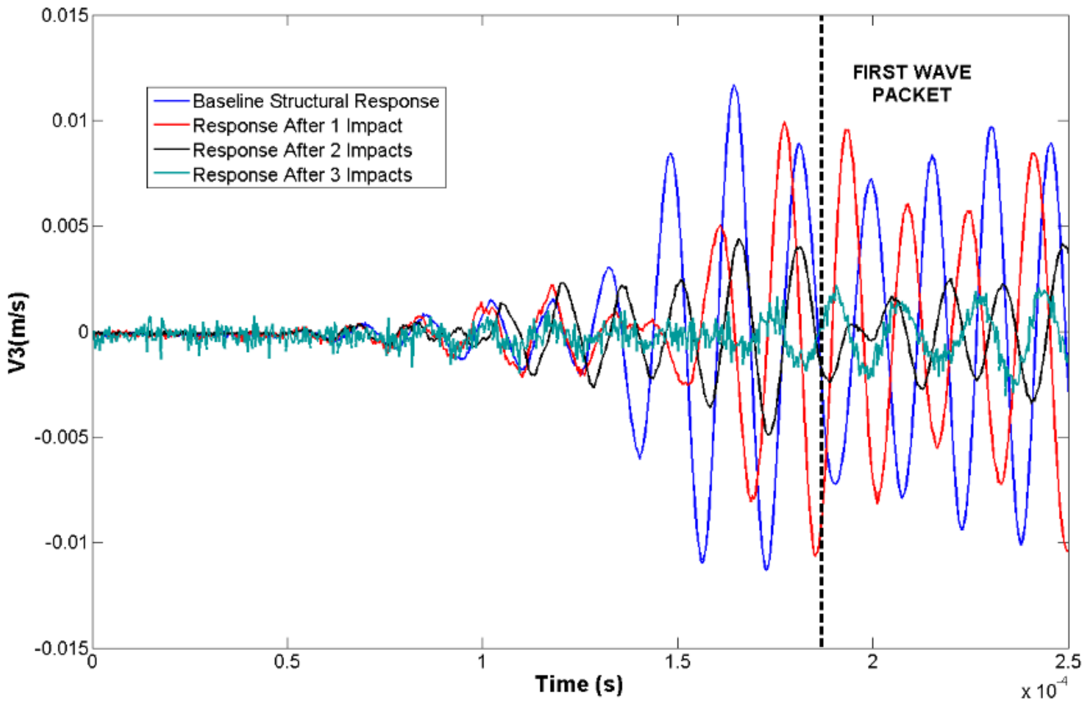

Figure 4.13 Structural response after consecutive impacts

The damaged waveforms begin to deviate from the healthy waveform as soon as the wave is sensed by the vibrometer. The plot also indicates that as damage increases, the amount of energy transmitted through the lap joint to the sensor decreases. This is indicated by the reduction in amplitude of the first wave packet after consecutive impacts.

4.7 Estimating Size of Damage

Estimating the size of damage is important since it can be a direct indicator of the remaining useful life of the structure. The attenuation and change in phase of the signal of the first wave packet received beyond the damage, is an indirect method of estimating the size of the damage. Only the first wave packet is considered because interference between reflections bouncing off material boundaries could later on cause high strength waves to be sensed by the vibrometer.

A damage index methodology (Jha & Watkins, 2012) is used to quantify the amount of damage in the structure. This DI originally developed for use with the time reversal method of estimating damage, has been employed to quantify the attenuation and phase change to the structural response brought about by damage to the structure. The larger the difference between the baseline and damaged structural responses, the greater the DI value. Eqn. 4.3 is used to determine the damage index value.

$$DI = \sqrt{\frac{\sum_N \left(D(t)-H(t)\right)^2}{\sum_N H(t)^2}} \tag{4.3}$$

D(t) is the amplitude of the damaged structure's response, *H(t)* is the amplitude of the healthy structure's response and *N* is the number of data points captured in the first wave packet. The DI obtained for each of the impacts is shown in Fig. 4.14. It should be noted that this damage index to predict extent of damage, is different from the damage index computed to triangulate the damage site.

Fig. 4.14 shows that there is a correlation exists between the DI value and the extent of damage in the joint. This DI value can thus very easily be correlated to the size of damage in the structure if there is a means of knowing the size of the inflicted damage. This can be done with the aid of an instrument such as a C-scan. The C-scan machine available at RFRL was not suitable for use with the lap joint specimens due to their rough surface finish.

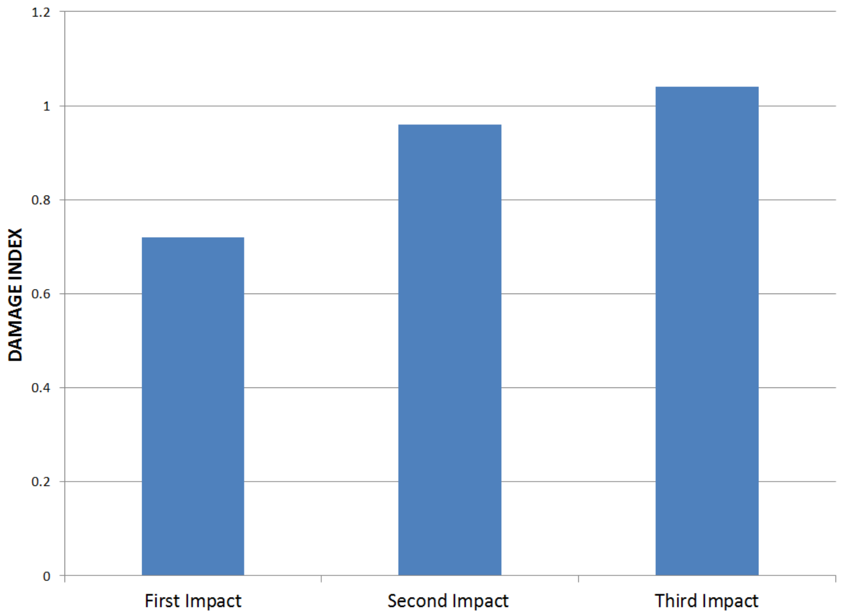

Figure 4.14 Damage index plotted against the no. of impacts.

The bar chart shows a progressive increase of damage index from a value of 0.74 to 1.04 with each consecutive impact.

According to the damage index equation, the value of DI should approach unity as the plate gets more and more damaged. After the third impact, the lap joint suffered catastrophic failure with large delaminations and partial disbond of the adhesive layer. The damage index value after the third impact is 1.04. A DI value greater than unity signifies that not only is the damaged response very small in amplitude, but also that it is out of phase with the baseline response.

Figure 4.15 Catastrophic failure of the lap joint.

The image shows an almost complete disbond of the upper plate from the lower plate.

4.8 Location of Damage

Damage was located using the time of flight method outlined in chapter II. A baseline reading was recorded prior to damaging the specimen, and the baseline and damaged structural responses were subsequently compared to determine the time of flight of the wave from the PZT to the sensory location after reflection from the damage. Fig. 4.16 shows the position of the coin (damage) on the structure along with the position of the three sensor locations which have designated as Points 1 to 3. Figs. 4.17 to 4.22 show the time of flight determination for the three sensory points. Figs. 4.23 and 4.24 show the damage prediction loci plot and the damage index plot for the simulated damage. The separation between the PZT and the coin is ~3inches (8cm).

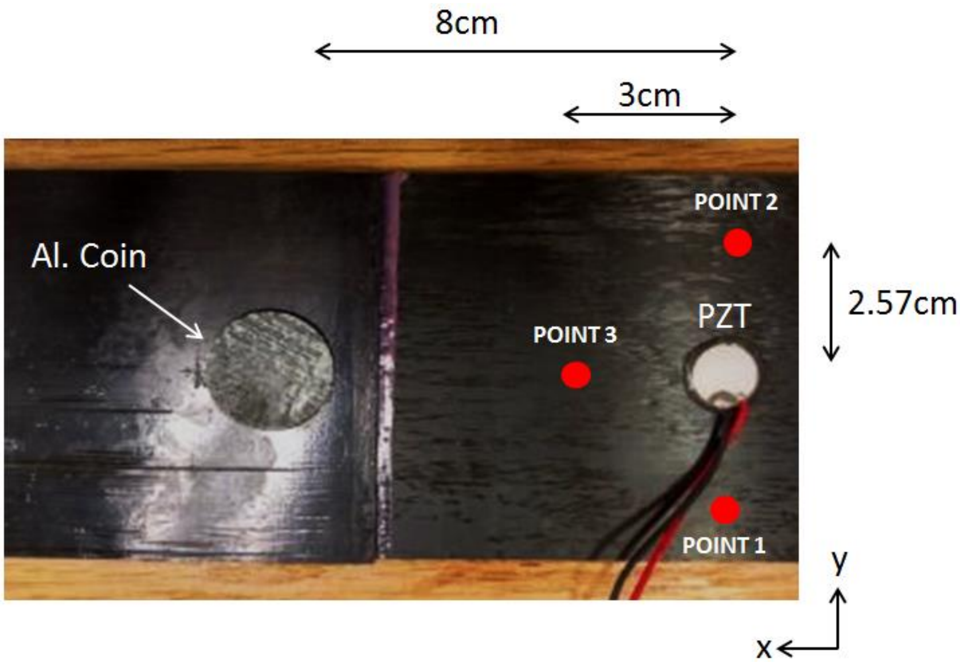

Figure 4.16 The position of the sensor locations (Points 1 to 3) and the position of the aluminum coin w.r.t. the PZT.

4.8.1 Simulated Damage – Structural Response at Point 1

The (x, y) coordinates of the sensor location with respect to the PZT are (0cm, -2.57cm). The superposition of the baseline and damaged structural response waveforms shows the damaged waveform deviating from the baseline at 0.211ms as seen in Figs. 4.17 and 4.18. This time marks the total time of flight of the wave from the PZT to the damage and the reflected wave from the damage to the sensor.

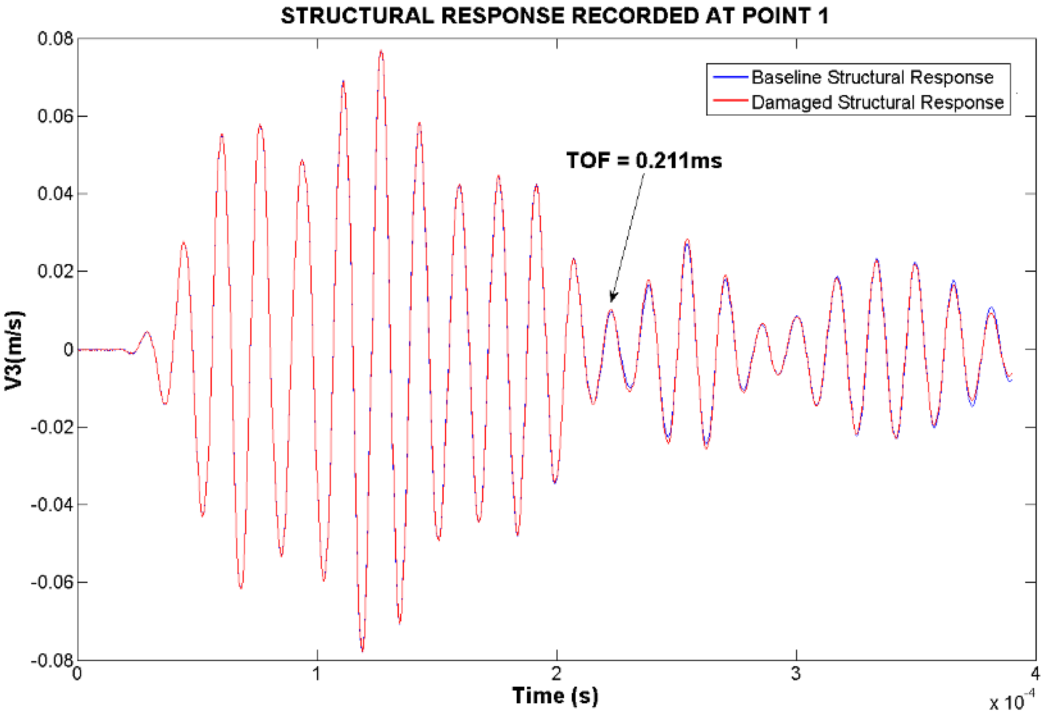

Figure 4.17 Response comparison at point 1

Comparison of baseline and damaged structural responses indicates deviation of the damaged response from the baseline response at 2.11×10^{-4} seconds. This is the time of flight of the wave from the PZT to the damage and back to the sensor location at Point 1.

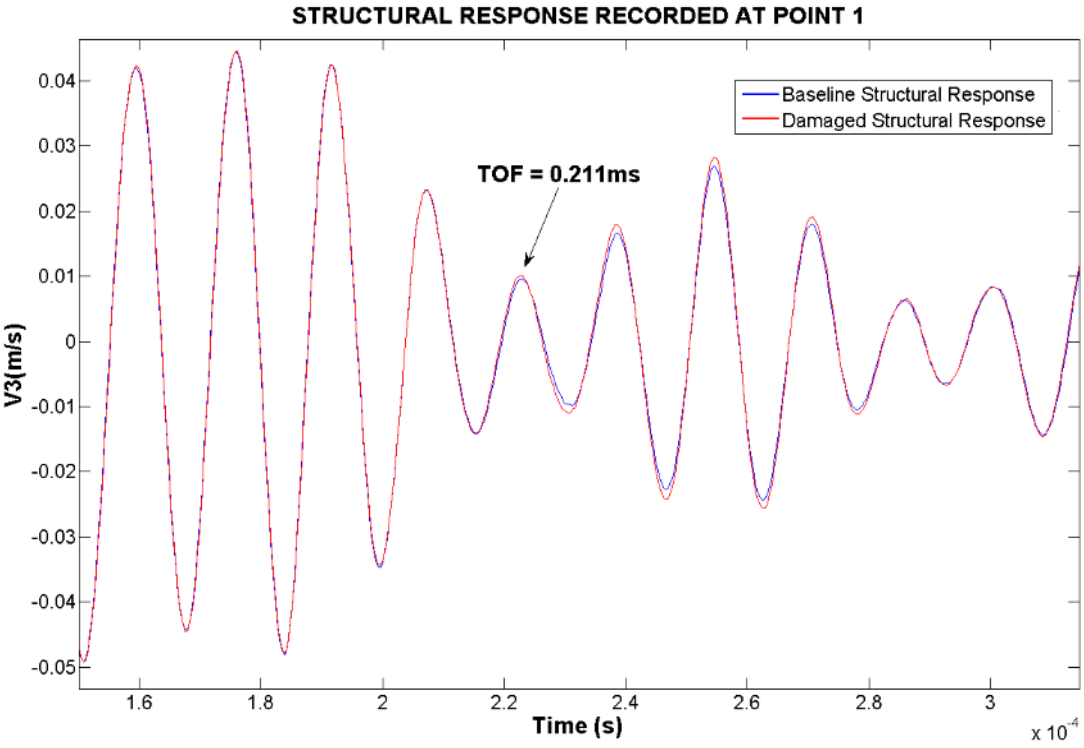

Figure 4.18 The blown up image of Fig. 4.17

The first point of deviation is at 2.11x10^{-4} seconds. The first point at which the damaged response deviates from the baseline response is marked in the image

4.8.2 Simulated Damage - Structural Response at Point 2

The (x,y) coordinates of the sensor location with respect to the PZT are (0cm, 2.57cm). These coordinates are in the (x,y) plane which is in the plane of the composite plates as seen in Fig. 4.16. The vibrometer structural response recorded at these coordinates is plotted in the two figures below. The damaged waveform shows a deviation at 1.91x10^{-4} seconds from the baseline response waveform. This deviation marks the total time of flight of the Lamb wave from the PZT which is at (0, 0) to the damage, and the reflected wave from the damage to the sensor coordinates.

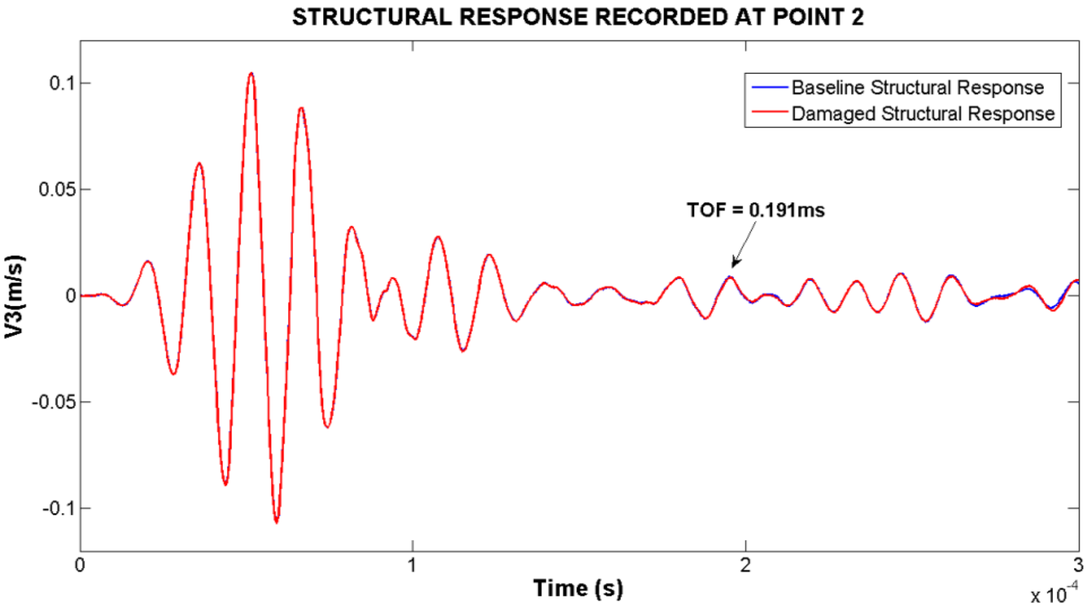

Figure 4.19 Comparison of baseline and damaged structural responses at point 2

The plot indicates start of deviation of the damaged response from the baseline response at 1.91×10^{-4} seconds. This is the time of flight of the wave from the PZT to the damage and back to the sensor location.

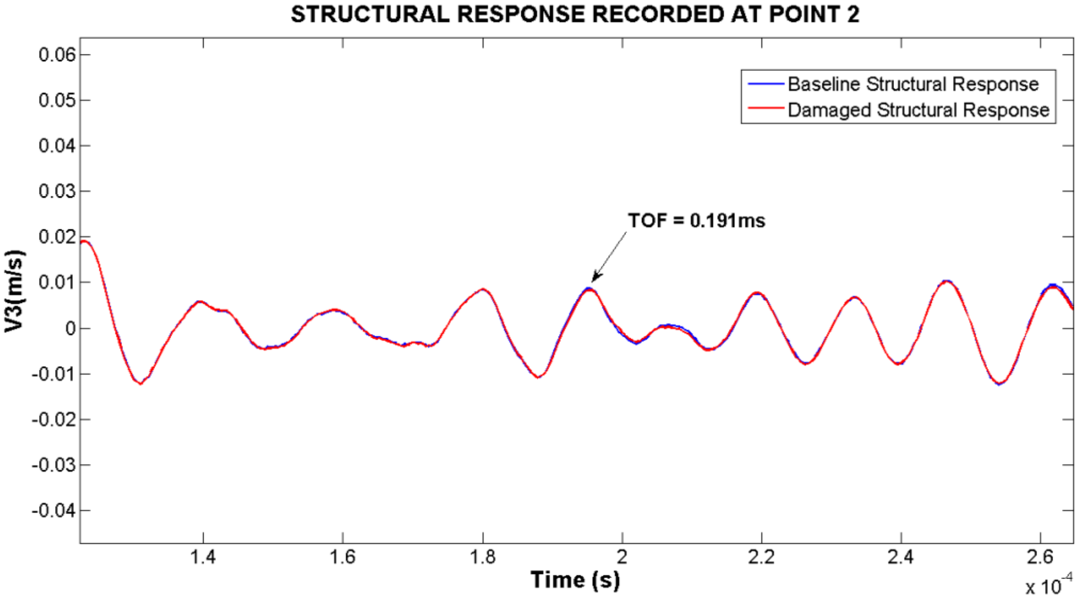

Figure 4.20 The blown up image of Fig. 4.19

The first point of deviation is at 1.91×10^{-4} seconds. The first point at which the damaged response deviates from the baseline response is marked in the plot

4.8.3 Simulated Damage – Structural Response at Point 3

The baseline and damaged structural responses were recorded at coordinates (3cm, 0cm). These coordinates are w.r.t the PZT and in the (x,y) plane. The vibrometer structural response recorded at these coordinates is plotted in the two figures below. The damaged waveform shows a deviation at 1.28×10^{-4} seconds from the baseline response waveform. This deviation marks the total time of flight of the Lamb wave from the PZT which is at (0, 0) to the damage, and the reflected wave from the damage to the sensor. This time is considerably shorter than those recorded at Point 1 and 2 because the wave has to travel a shorter distance between the damage site and sensor Point 3.

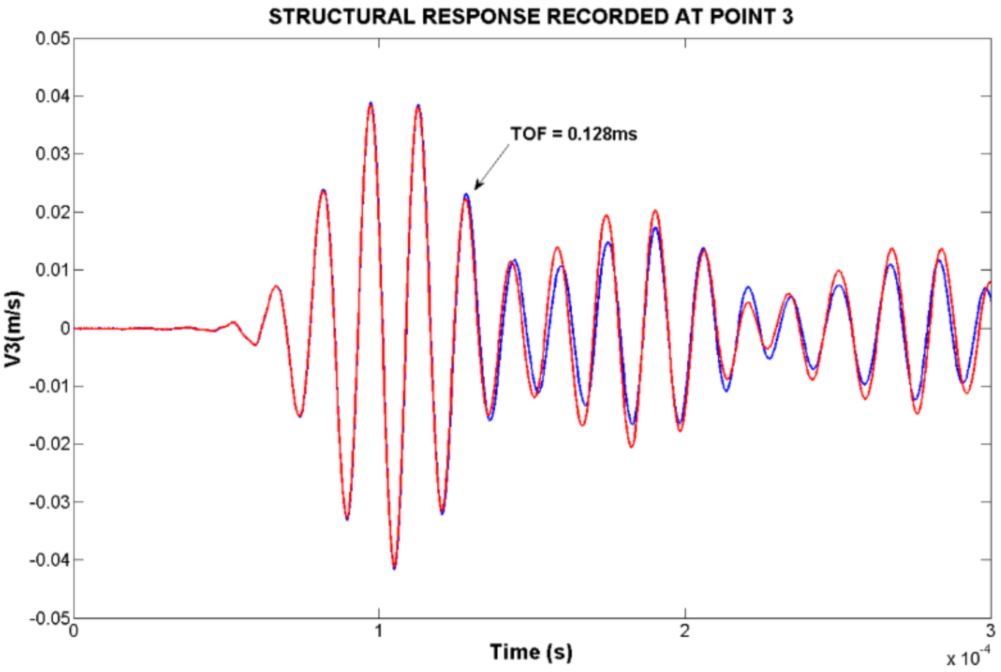

Figure 4.21 Comparison of baseline and damaged structural responses at point 3.

The plot indicates start of deviation of the damaged response from the baseline response at 1.28×10^{-4} seconds. This is the time of flight of the wave from the PZT to the damage and back to the sensor location.

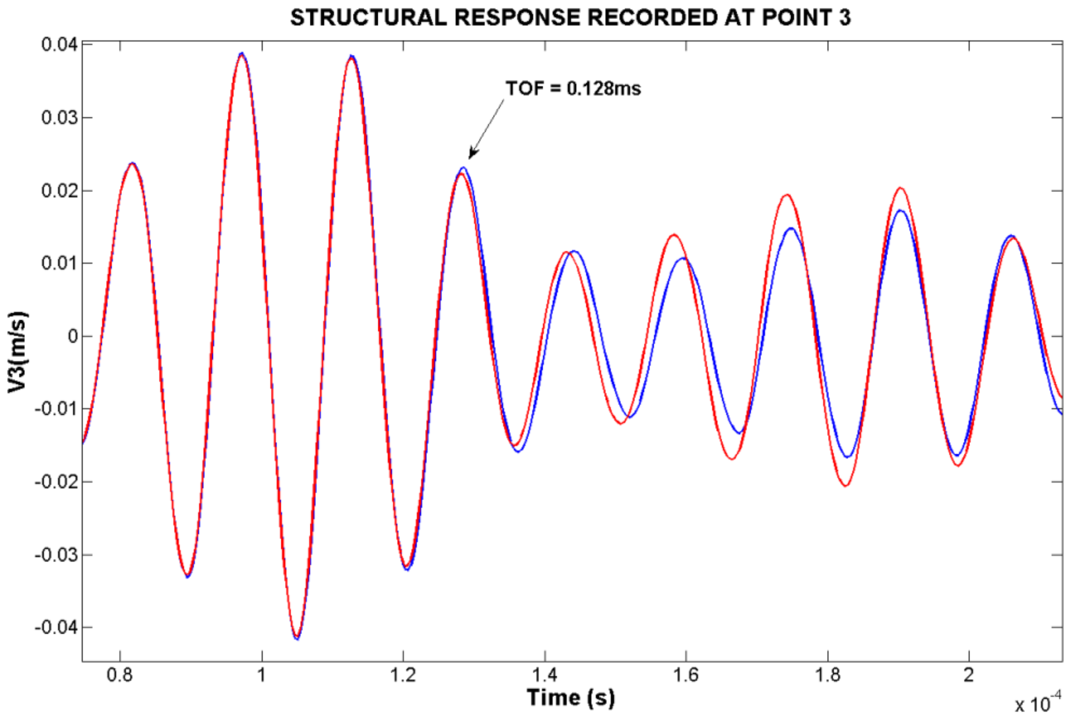

Figure 4.22 The blown up image of Fig. 4.21

The blown up plot indicates the first point of deviation at 1.28×10^{-4} seconds. The first point of deviation is marked in the image

The actual damage site is 8cm to the left of the PZT and is marked as a bright red star in the damage loci plot (Fig. 4.23). The time of flight along with the (x, y) coordinates of the sensor point w.r.t. the PZT are used to generate a single damage prediction locus. The three sensors give rise to three unique loci which are used to triangulate the damage location. As can be observed in Fig. 4.22, the three loci approach each other the closest in the region around the actual damage site.

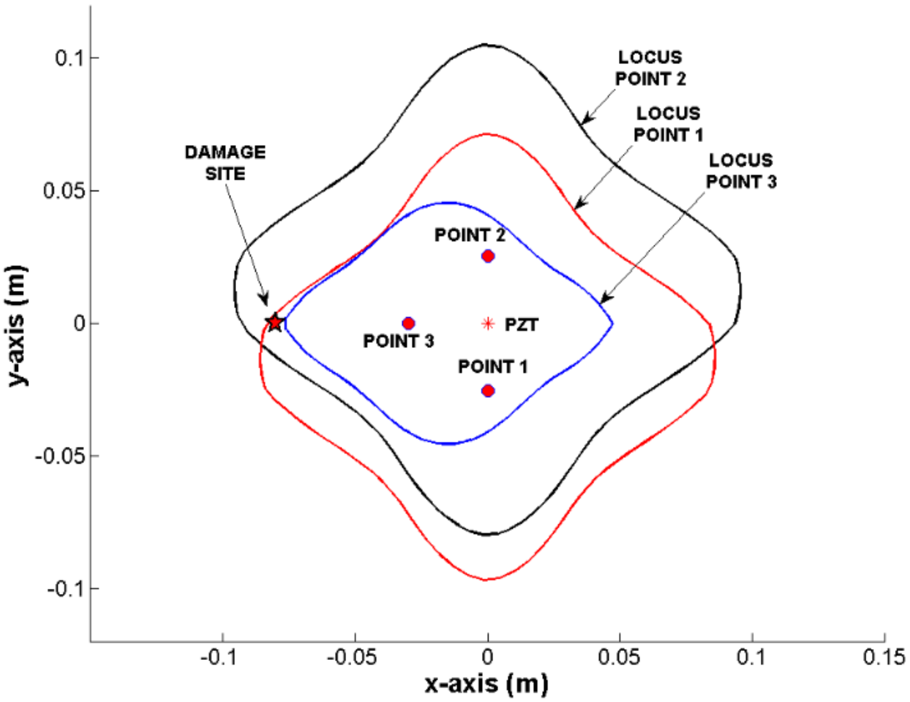

Figure 4.23 Generation of loci from the time of flight methodology for the coin simulated damage

The damage locus plot covers an unnecessarily large area which extends beyond the region of the physical lap joint structure. To reduce computational burden, only the area covered by the physical structure was considered for the DI plot. The area was divided into a 1000 by 1000 grid and the DI was evaluated at each grid point. The grid point at which the four loci approach each other the closest is the point of predicted damage. Fig. 4.24 shows that the predicted damage (point of highest DI) is within 2cm of the actual damage site (red star).

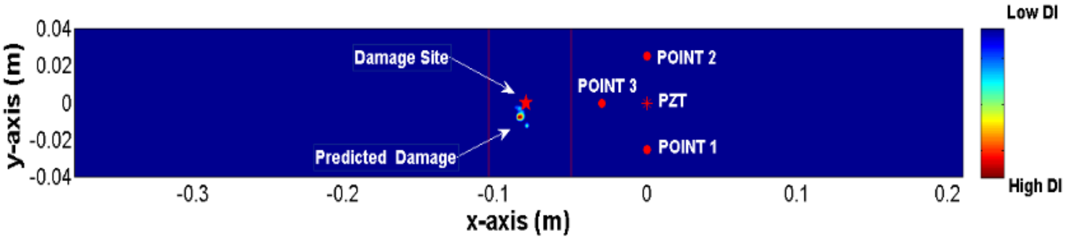

Figure 4.24 Damage index plot predicting damage to lie within 2cm of the actual damage site

The structure was subsequently damaged at two points A and B using the drop tower as described in section 4.4. The results presented in this section are after the impactor was dropped first on damage site A and then damage site B from a height of 40cm. Fig. 4.24 shows the relation between the damage sites, the PZT and the sensor locations. Site A is located 12.7cm away from the PZT on the lower plate and site B is located 8cm away from the PZT on the upper plate. The drop tower induced damage is barely visible to the naked eye, but can be sensed by touch.

Figure 4.25 The sites of actual damage A and B.

Site A is located 12.7cm away from the PZT on the lower plate and site B is located 8cm away from the PZT on the upper plate. The plot also shows the relative position of the four sensor points which are located at a radial distance of 2.57cm from the PZT at 270°, 90°, 0° and 180° respectively.

Sections 4.8.4 to 4.8.6 plot the baseline and damaged structural response to the Lamb wave propagation through the composite lap joint at sensor positions located at Points 1, 2 and 3 for damage at site A. These sensor points are as shown in Fig. 4.25. They are each at a radial distance of 2.57cm from the PZT and are at 270°, 90° and 0° to the x-axis respectively. These plots are used to determine the time of flight of the wave from the PZT to the damage at site A and back to the respective sensor positions. Similarly, sections 4.8.5 to 4.8.7 plot the baseline and damaged structural response for damage at Site B to determine the times of flight of the Lamb wave.

4.8.4 Experiment with Actual Damage at Site A – Structural Response at Point 1

The (x, y) coordinates of the sensor location with respect to the PZT are (0cm,-2.57cm). The structural response recorded at these coordinates is plotted in the two figures below. Fig. 4.26 shows that the initial damaged structural response closely matches the baseline response. A blown up section of Fig. 4.26 is plotted in Fig. 4.27 and shows that the damaged waveform begins to deviate from the baseline waveform at $2.48\text{x}10^{-4}$ seconds. This is the time of flight of the wave from the PZT to the damage at site A and back to the sensory location ‘Point 1’.

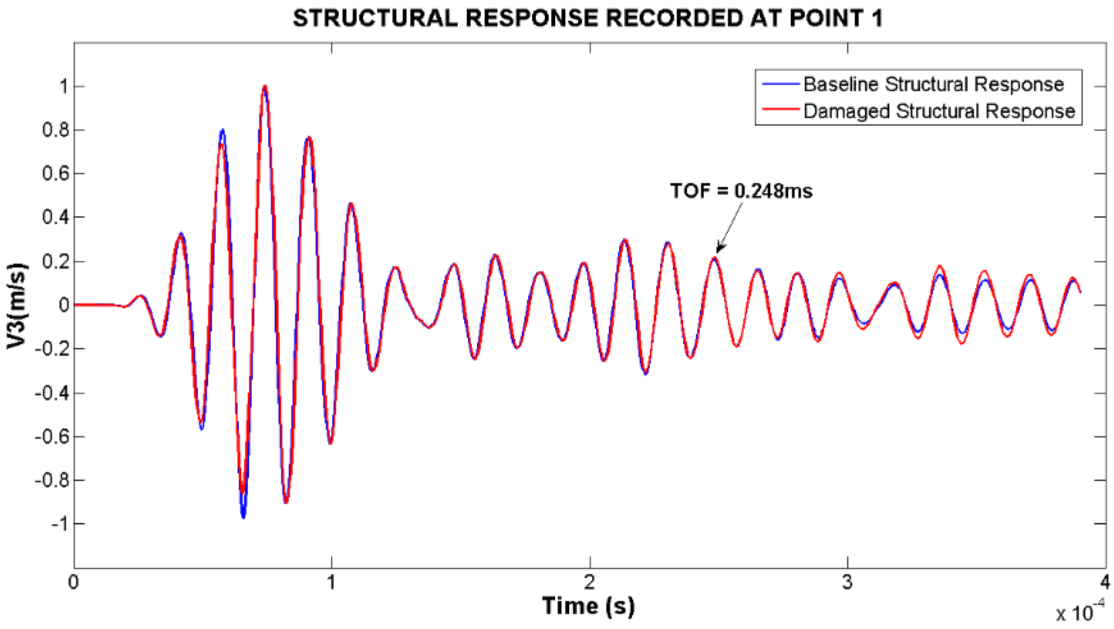

Figure 4.26 Comparison of baseline and damaged structural responses

The plot indicates start of deviation at $2.48\text{x}10^{-4}$ seconds. This is the time of flight of the wave from the PZT to the damage and back to the sensor location.

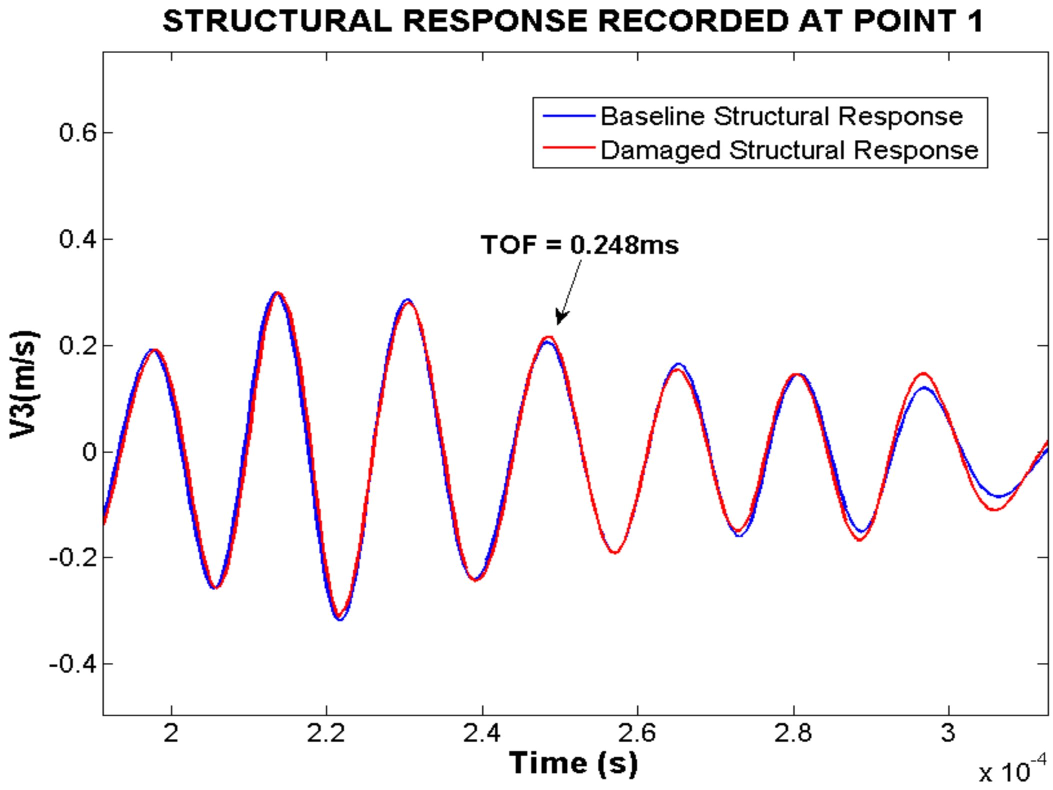

Figure 4.27 Zoomed structural response indicates deviation at 2.48x10^{-4} seconds

4.8.5 Experiment with Actual Damage at Site A –Structural Response at Point 2

The time of flight evaluation at the sensor location ‘Point 2’ is conducted in a manner similar to that outlined in section 4.8.4. The damaged waveform, as seen in Figs. 4.28 and 4.29, is seen to begin deviating from the baseline structural response at 2.56x10^{-4} seconds.

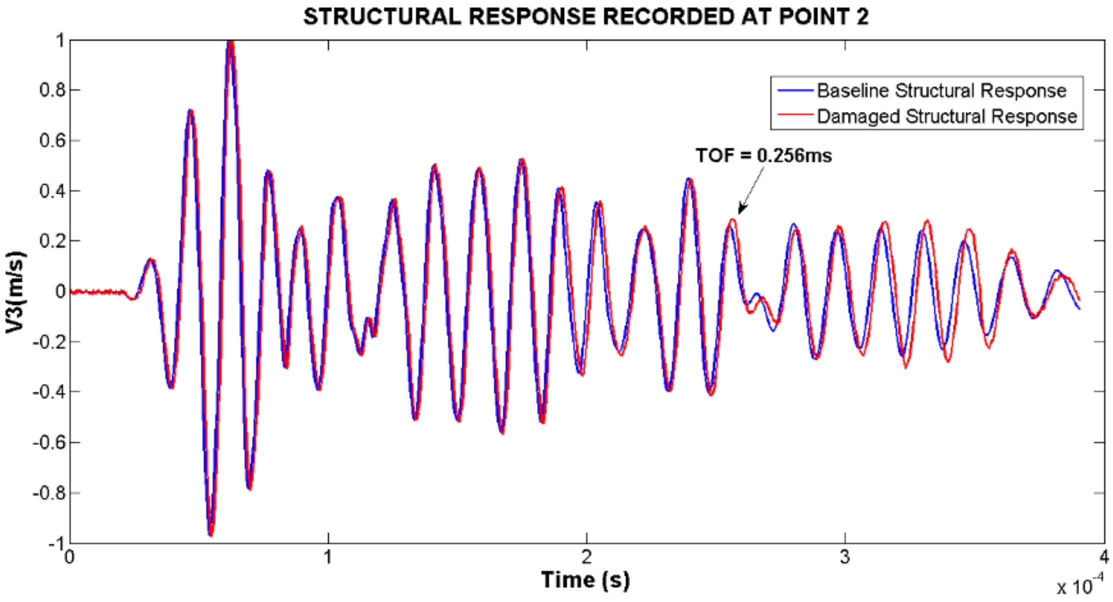

Figure 4.28 Comparison of baseline and damaged structural responses at point 2.

The plot indicates start of deviation of the damaged response from the baseline response at 2.56x10^{-4} seconds. This is the time of flight of the wave from the PZT to the damage and back to the sensor location. The structural response of the damaged structure was slightly out of phase with the baseline because the vibrometer was not correctly positioned at Point 2.

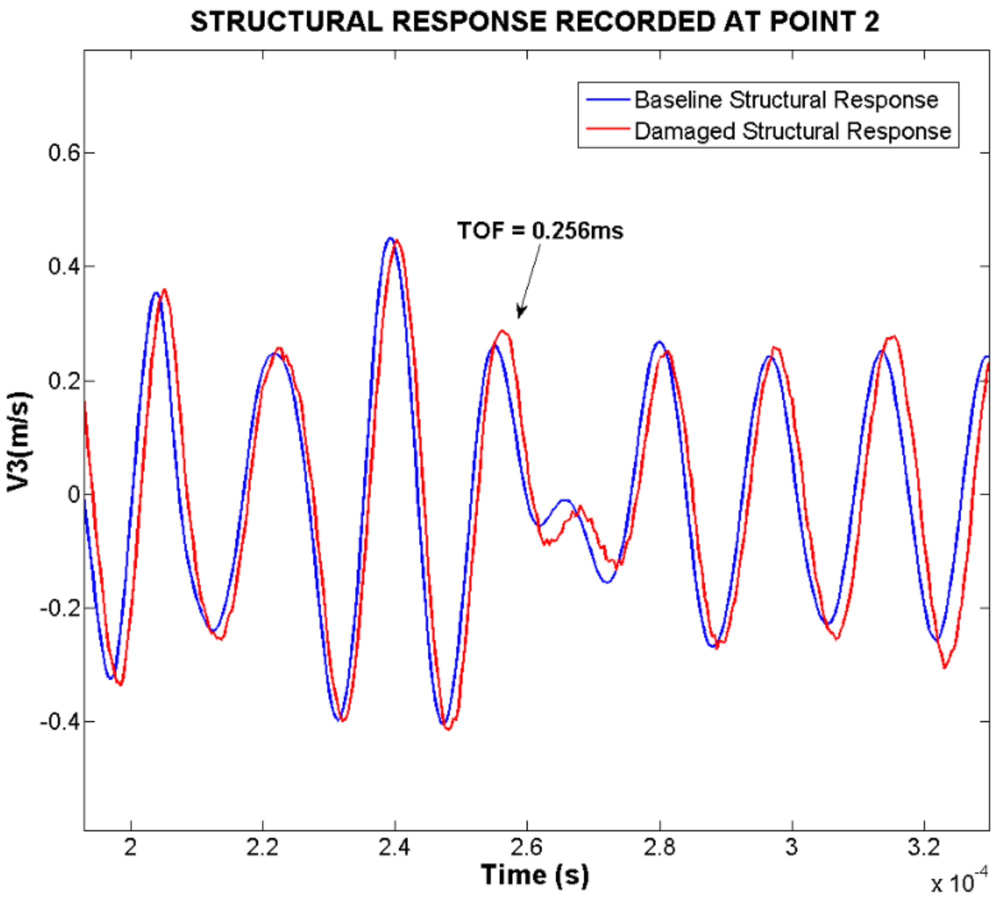

Figure 4.29 The blown up image of Fig. 4.28

The plot indicates the first point at which the damaged response beings to deviate from the baseline response at 2.56x10^{-4} seconds. The first point of deviation is marked in the plot

4.8.6 Experiment with Actual Damage at Site A –Point 3

The time of flight evaluation at the sensor location ‘Point 3’ is conducted in a manner similar to that outlined in section 4.8.4. The damaged waveform, as seen in Figs. 4.30 and 4.31, is seen to begin deviating from the baseline structural response at 2.28x10^{-4} seconds.

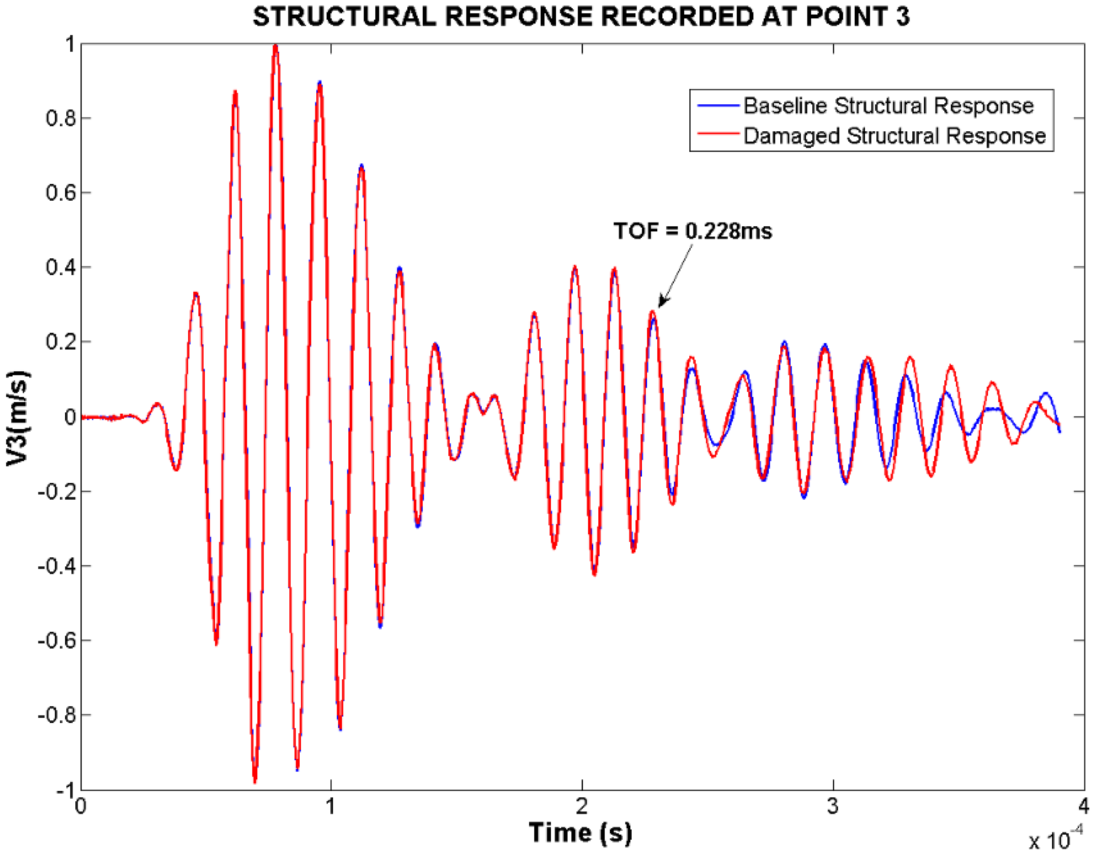

Figure 4.30 Comparison of healthy and damaged structural responses at point 3.

A blown up section of this plot is plotted in Fig. 4.31 to determine the exact time at which the damaged structural response begins to deviate from the baseline response. Fig. 4.31 indicates the start of deviation at 2.28×10^{-4} seconds

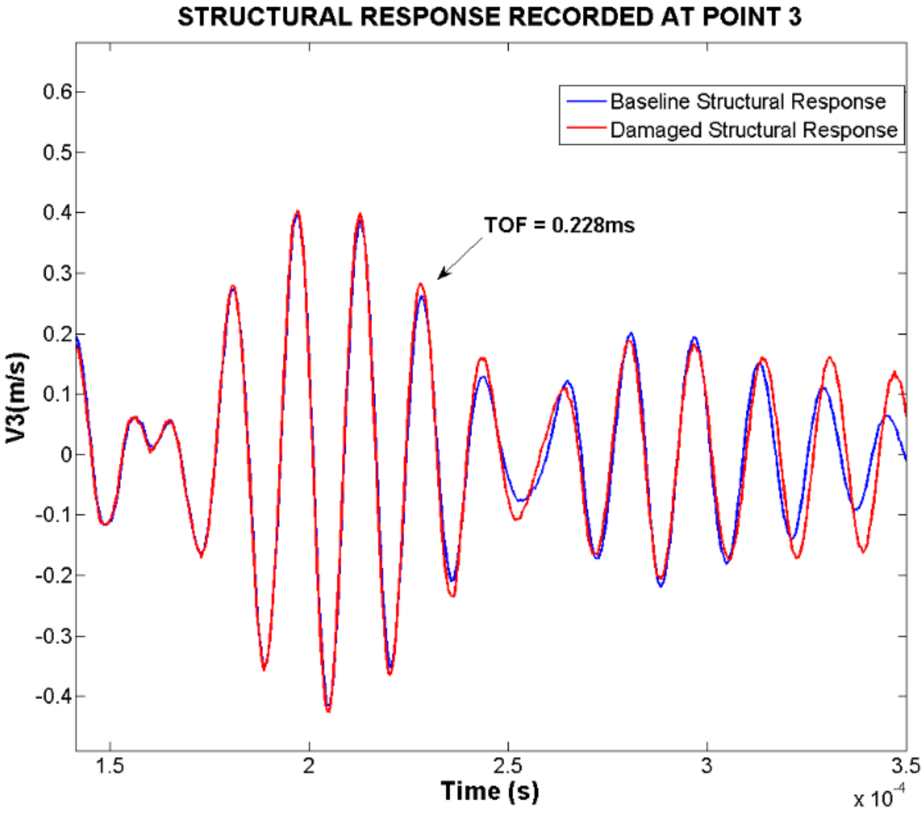

Figure 4.31 Blown up section of baseline and damaged structural responses indicates initiation of deviation at 2.28×10^{-4} seconds

4.8.7 Experiment with Actual Damage at Site B – Point 1

The (x, y) coordinates of the sensor location with respect to the PZT are (0cm, -2.57cm). The structural response recorded at these coordinates is plotted in the two figures below. Fig. 4.32 shows that the initial damaged structural response closely matches the baseline response. A blown up section of Fig. 4.32 is plotted in Fig. 4.33 and shows that the damaged waveform begins to deviate from the baseline waveform at 1.7×10^{-4} seconds. This is the time of flight of the wave from the PZT to the damage at site A and back to the sensory location 'Point 1'. Fig. 4.32 also shows that once the damaged waveform begins to deviate from the baseline waveform, it not only displays a deviation in amplitude, but also in phase.

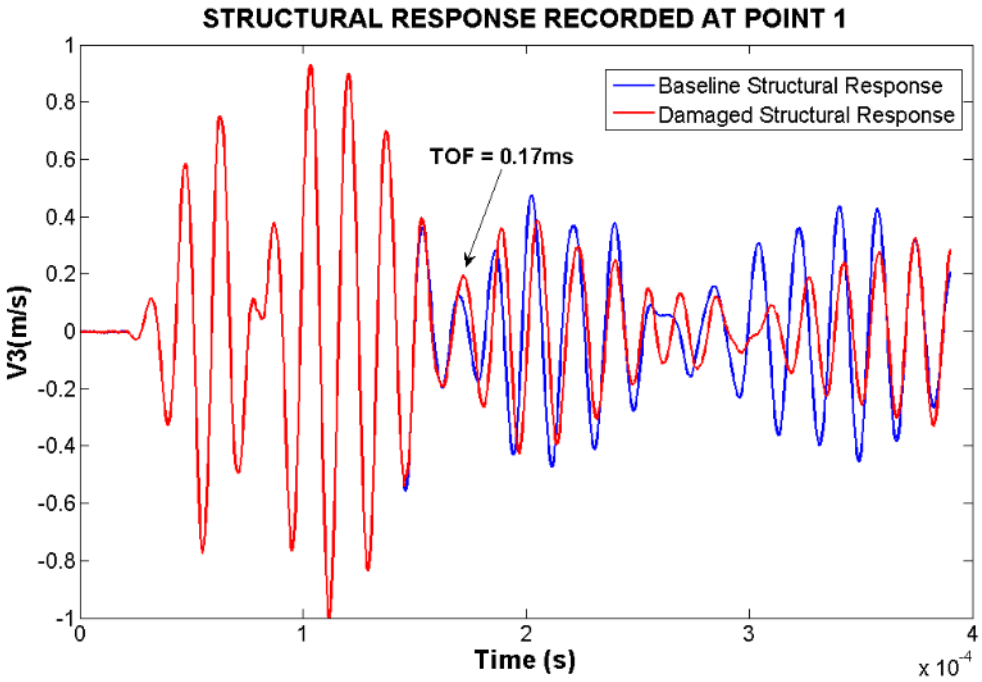

Figure 4.32 Comparison of healthy and damaged structural responses at point 1.

A blown up section of this plot is plotted in Fig. 4.33 to determine the exact time at which the damaged structural response begins to deviate from the baseline response.

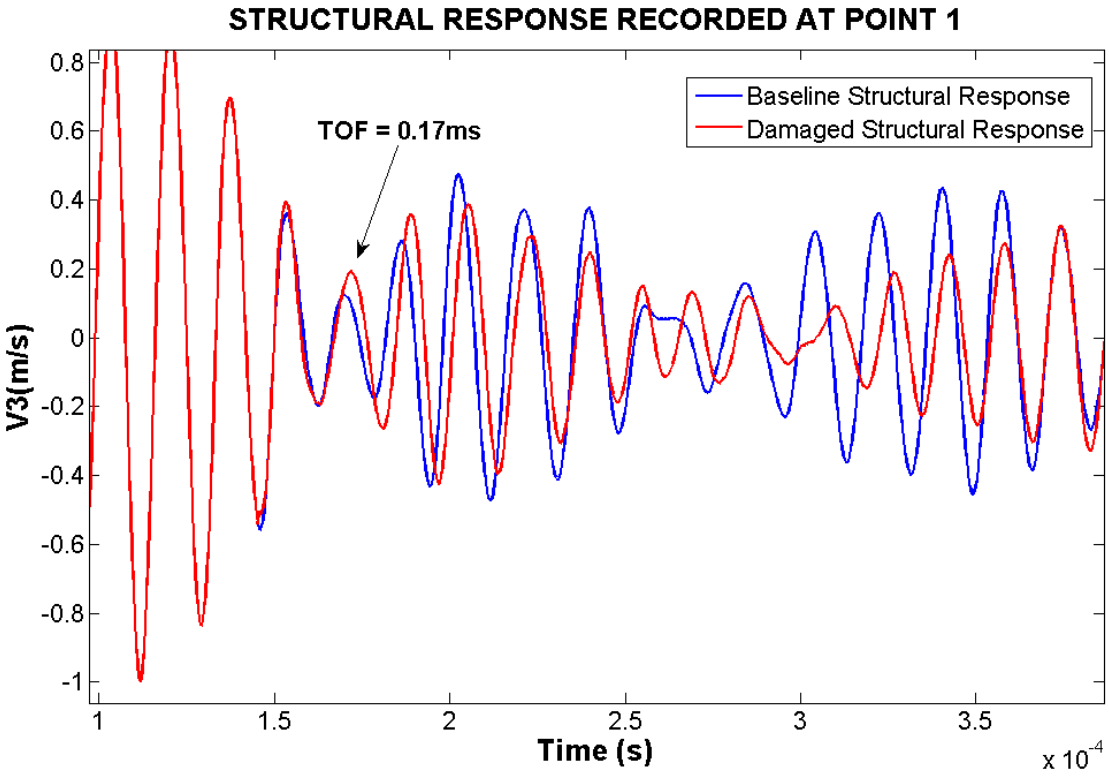

Figure 4.33 Blown up section of baseline and damaged structural responses indicates initiation of deviation at 1.7x10^{-4} seconds

4.8.8 Experiment with Actual Damage at Site B – Structural Response at Point 2

The (x, y) coordinates of the sensor location at ‘Point 2’ with respect to the PZT are (0cm, 2.57cm). The time of flight evaluation at the sensor location ‘Point 2’ is conducted in a manner similar to that outlined in section 4.8.7. The damaged waveform, as seen in Figs. 4.34 and 4.35, is seen to begin deviating from the baseline structural response at 1.87x10^{-4} seconds.

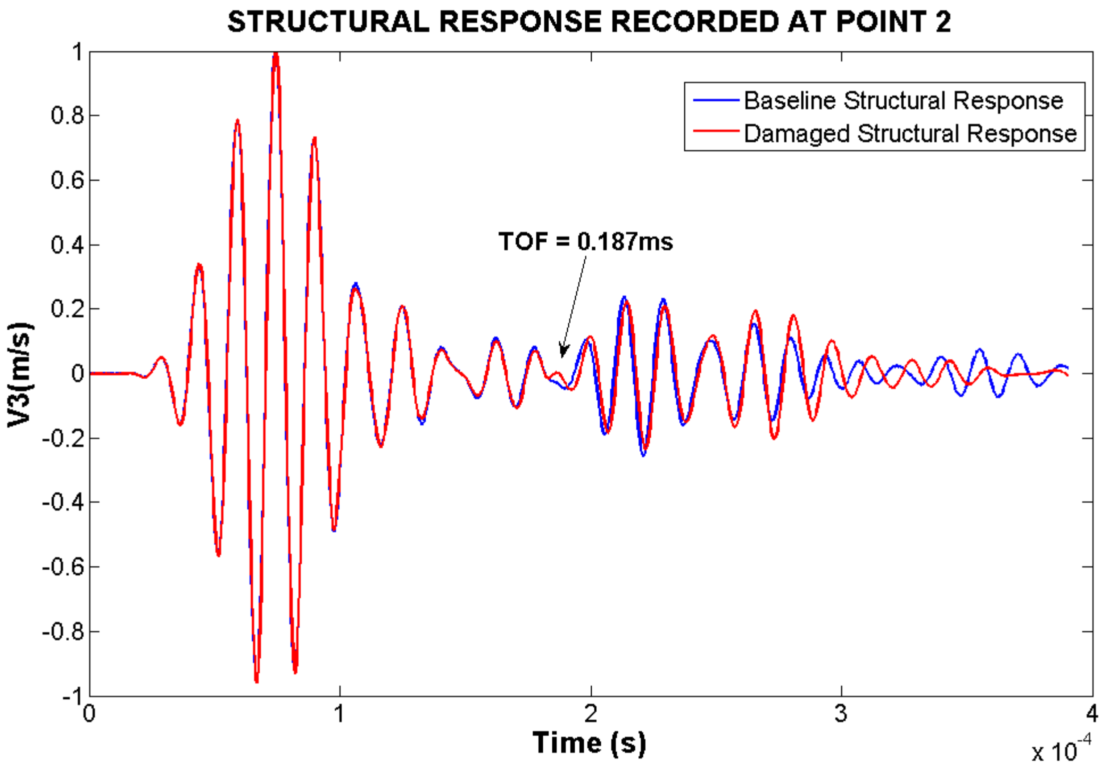

Figure 4.34 Comparison of healthy and damaged structural responses at point 2.

A blown up section of this plot is plotted in Fig. 4.35 to determine the exact time at which the damaged structural response begins to deviate from the baseline response. Fig. 4.35 indicates the start of deviation at 1.87x10^{-4} seconds

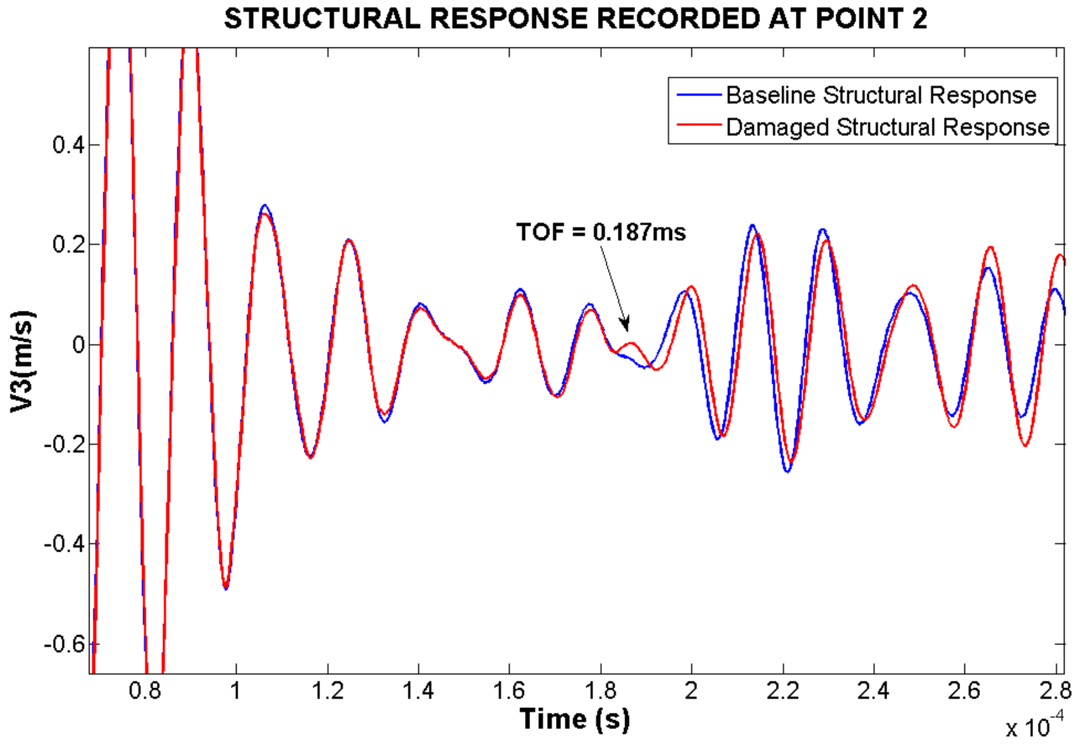

Figure 4.35 Blown up section of baseline and damaged structural responses

The plot clearly indicates initiation of deviation between the responses at 1.87x10^{-4} seconds

4.8.9 Experiment with Actual Damage at Site B – Point 4

The (x, y) coordinates of the sensor location at 'Point 4' with respect to the PZT are (2.57cm, 0cm). The time of flight evaluation at the sensor location 'Point 4' is conducted in a manner similar to that outlined in section 4.8.7. The damaged waveform, as seen in Figs. 4.36 and 4.37, is seen to begin deviating from the baseline structural response at 1.53x10^{-4} seconds.

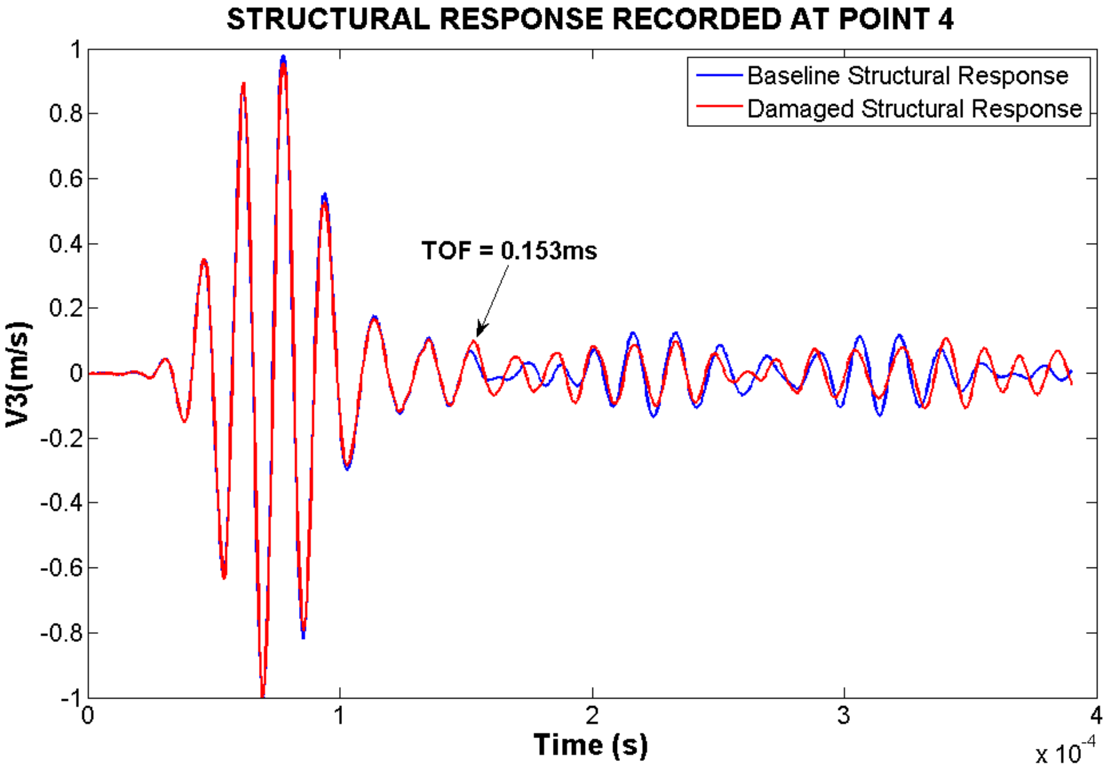

Figure 4.36 Comparison of healthy and damaged structural responses at point 4.

A blown up section of this plot is plotted in Fig. 4.37 to determine the exact time at which the damaged structural response begins to deviate from the baseline response. Fig. 4.37 indicates the start of deviation at 1.53×10^{-4} seconds

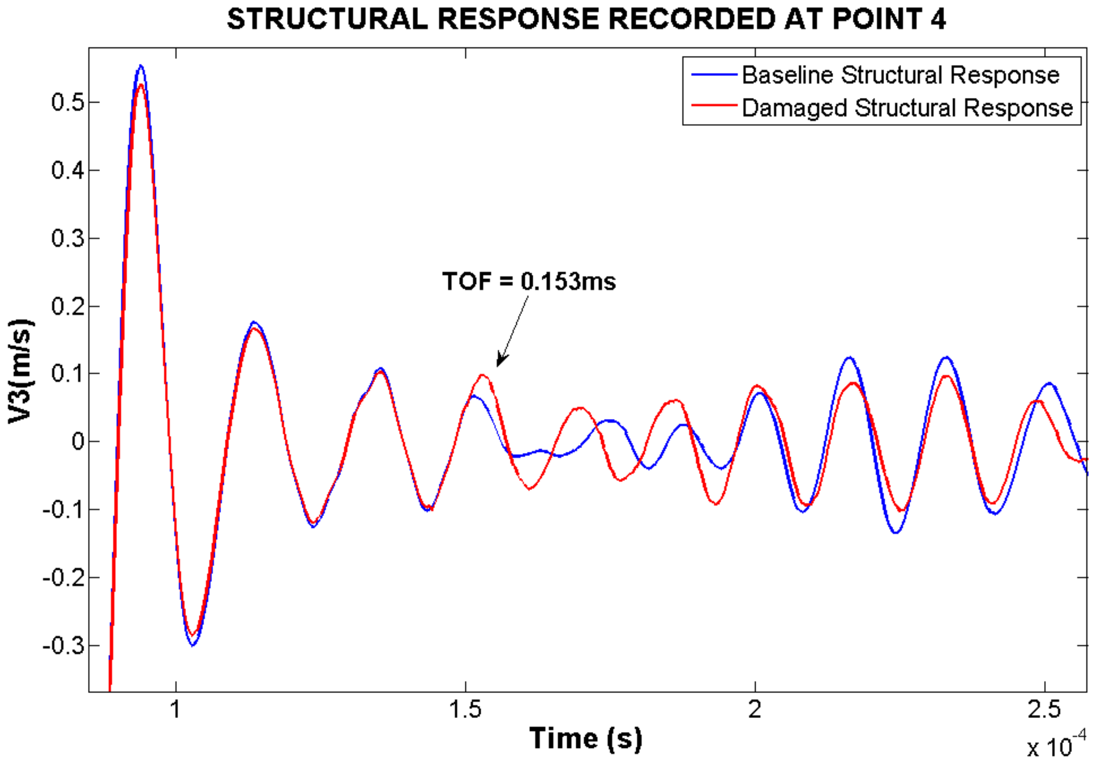

Figure 4.37 Blown up section of baseline and damaged structural responses at point 4

The plot indicates initiation of deviation at 1.53x10^{-4} seconds

4.9 Loci Plot and Damage Index Plot Generation for Damage Prediction at Site A

The coordinates of the sensor position w.r.t. the PZT and the times of flight determined in sections 4.8.4 to 4.8.6 are tabulated in table 4.2.

Table 4.2 Sensor coordinates and times of flight recorded at each sensor location.

Sensor	(x, y) Coordinates w.r.t. PZT (cm)	Time of flight (x10^{-4} seconds)
Point 1	0, -2.57	2.48
Point 2	0, 2.57	2.56
Point 3	-2.57, 0	2.28

These are the inputs to the locus generation and damage index plot creation MATLAB program

These coordinates and times of flight are entered as inputs in the locus generation MATLAB program (Appendix A) to create a plot that shows all three loci superimposed one on top of the other as shown in Fig. 4.38. It is also apparent in Fig. 4.38 that the region in which the three loci approach each other the closest is very close to the actual damage site (marked as a red star).

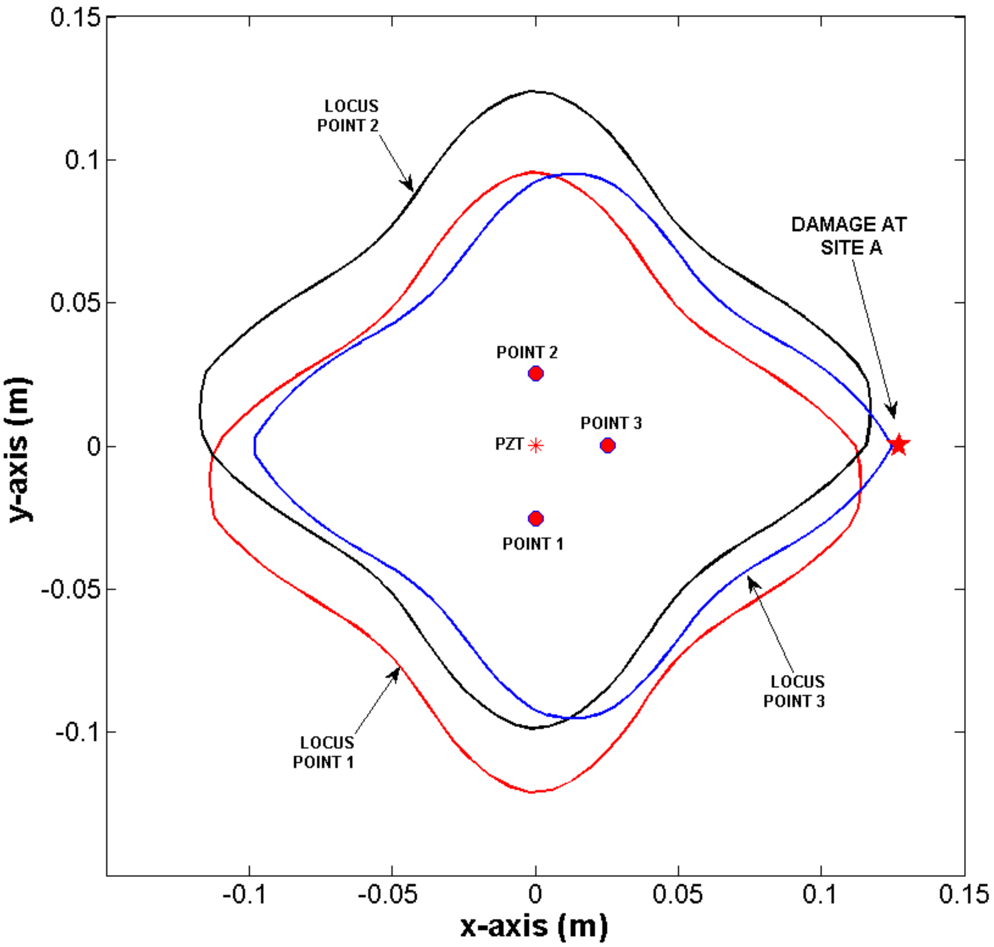

Figure 4.38 Generation of loci from the time of flight methodology for the drop test inflicted damage at Site A

Since evaluating the damage index at a grid point is computationally expensive, only that area of the loci plot that falls within the region of the physical structure is evaluated. The damage index plot in Fig. 4.39 shows that the damage location methodology successfully predicts the location of damage to within 2cm of the actual damage at site A. The difference between the actual and predicted damage sites could be because the drop tower caused damage such as a delamination or fiber-matrix disbond that spread as far as the predicted damage site. This could not be confirmed due to the surface of the composite laminate not being smooth enough to enable the use of a C-scan machine to evaluate the size and extent of the damage inflicted by the drop tower.

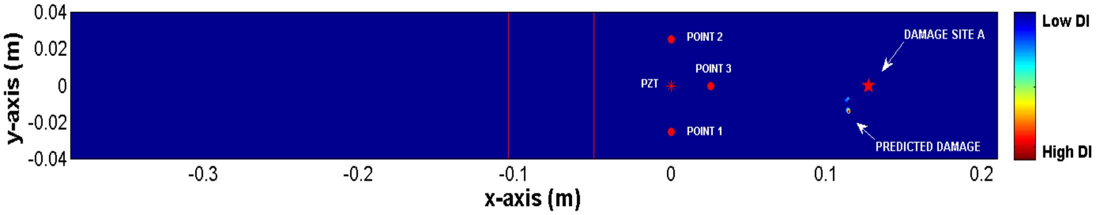

Figure 4.39 Damage index plot prediction of the drop test inflicted damage at Site A. The damage location prediction methodology successfully predicts damage to within 2cm.

4.10 Loci Plot and Damage Index Plot Generation for Damage Prediction at Site B

Site B lies in the middle of the lap joint. Thus the damage inflicted by the drop tower extended to the composite laminates as well as to the adhesive layer. The exact size and shape of the damage could not be ascertained due to the inability of the available C-scan machine to function on a surface that was not perfectly smooth. The coordinates and times of flight recorded at each sensor position are tabulated in table 4.3.

Table 4.3 Sensor coordinates and times of flight recorded at each sensor location.

Sensor	(x, y) Coordinates w.r.t. PZT (cm)	Time of Flight (x10^{-4} seconds)
Point 1	0, -2.57	1.7
Point 2	0, 2.57	1.87
Point 4	2.57, 0	1.53

These are the inputs to the locus generation and damage index plot creation MATLAB program

These coordinates and times of flight are entered as inputs in the locus generation MATLAB program (Appendix A) to create a plot that shows all three loci superimposed one on top of the other as shown in Fig. 4.40. It is also apparent in Fig. 4.40 that the region in which the three loci approach each other the closest is very close to the actual damage site (marked as a red star).

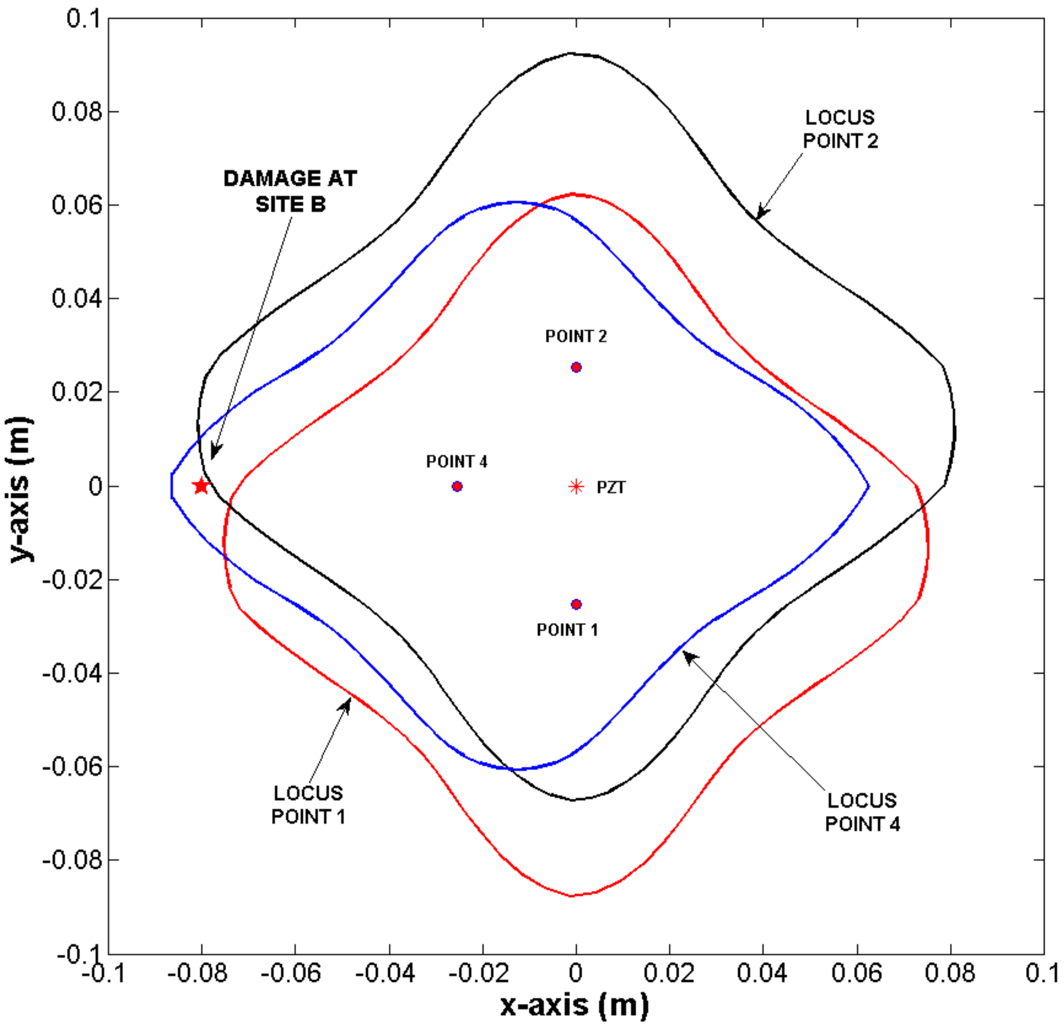

Figure 4.40 Generation of loci from the time of flight methodology for the drop test inflicted damage at Site B.

The plot shows that the region in which the three loci approach each other the closest is very close to the actual damage site.

The damage index plot in Fig. 4.41 shows that the damage location methodology successfully predicts the location of damage to within 2cm of the actual damage at site B. The difference between the actual and predicted damage sites could be because the drop tower caused damage such as a delamination or a disbond in the adhesive layer that spread as far as the predicted damage site. This could not be confirmed due to the surface of the composite laminate not being smooth enough to enable the use of a C-scan to evaluate the size and extent of the damage inflicted by the drop tower.

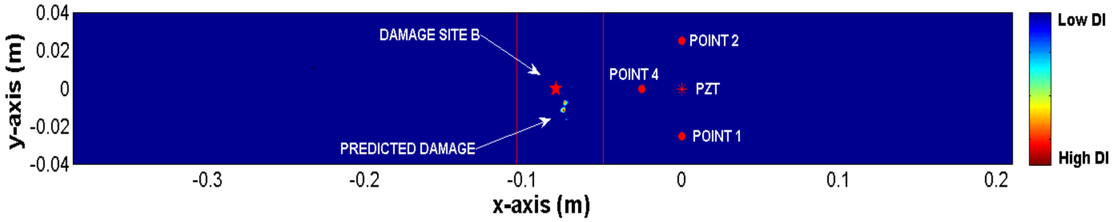

Figure 4.41 Damage index plot prediction of the drop test inflicted damage at Site B

The loci and damage index plots in Figs. 4.38 to 4.41 demonstrate the ability of the damage triangulation methodology to accurately predict the location of the damage. The SHM triangulation system was able to predict the front or the edge of the damage that was closest to the PZT-sensor pair and the damage index plots show a visual representation of where the damage was predicted to lie.

CHAPTER V

CONCLUSIONS

The methodology proposed to conduct SHM in adhesively bonded composite lap joints has been validated using both numerical and experimental methods. The finite element numerical methods indicated that damage as small as 1.27cm in diameter can be sensed and triangulated. The triangulation method adopted a set of loci formed using the relative position of the sensor w.r.t. the actuator, and times of flight of Lamb waves from the actuator to the damage and back to a sensor. The algorithm, though numerically very demanding, was able to predict the location of damage to within 2cm. The algorithm to assign a damage index number to grid points on the structure was also able to successfully demonstrate a visual representation of the damage location prediction. This therefore took away the ambiguity attached to human interpretation of the loci plot.

Lamb wave based experiments conducted on a physical, adhesively bonded composite lap joint structure that was laid up and cured in-house, proved that damage, both simulated (using a coin) and actual (inflicted by the drop test) could be sensed in both the upper and lower plates using sensors and actuators placed on either one of the plates. The Lamb waves, unlike the undamped FEA simulations, experienced attenuation, but features to determine the time of flight of the Lamb wave from the actuator to the damage and back to the sensor could still be determined.

The triangulation technique worked as theorized in the methodology. Damage prediction locus generated by each time of flight reading from a PZT-sensor pair was created by the triangulation algorithm. The point of closest approach of multiple such loci generated by multiple PZT-sensor pairs was the region of predicted damage. A damage index was formulated to visually represent the damage prediction site. This visual representation showed that the methodology to triangulate the location of damage, accurately predicted the damage site to within a 2cm radius of the actual damage site.

A secondary damage index, proposed to predict the size of damage, gave a rudimentary indication of the extent of damage in the joint by computing the loss in transmission strength of Lamb waves across the lap joint. The first three levels of SHM, i.e. the detection, triangulation and prediction of the size of damage were thus successfully achieved.

Tuning the Lamb wave frequency was discovered to be extremely important. At very low frequencies, only a very small part of the wave gets reflected from the damage and damage is thus more difficult to sense. Alternately, high frequency waves attenuate too quickly due to the greater damping by the material and therefore result in a reduction of the radius of sensitivity to damage. Thus, the un-tuned wave with a lower signal-to-noise ratio showed a significantly smaller deviation of the damaged response from the baseline response, as compared to the tuned wave.

5.1 Future Work

There was some difficulty in precisely repositioning the vibrometer. A change in sensing element from the laser vibrometer to another permanently mounted technology such as a PZT or a FBG optic fiber system would allay this problem. FBG systems are especially suitable since they can be embedded in the composite layup without causing noticeable deterioration of the laminate strength. They are also light, can be multiplexed and certain systems have a sampling rate high enough to sense Lamb wave propagation (Micron Optics, 2015).

The damage index computed to predict the size of damage was not compared to the actual size of the damage. This is because the composite laminates produced in the lab did not have the required surface finish to enable the use of a hand-held ultrasonic c-scan machine. Future work to create samples with sufficiently smooth surface finish would enable the use of a C-scan machine, thus enabling the correlation of the damage index values to actual damage size/extent.

BIBLIOGRAPHY

Airbus. (2013, November 25). *The Success Story of Airbus*. (Airbus) Retrieved October 5, 2015, from www.airbus.com: http://www.airbus.com/company/history/the-narrative/fly-by-wire-1980-1987/

Airbus. (2015, October 19). *www.airbus.com*. Retrieved from www.airbus.com: http://www.airbus.com/aircraftfamilies/passengeraircraft/a350xwbfamily/technology-and-innovation/

Balasubramaniam, K., Vishnuvardhan, J., Muralidharan, A., & Krishnamurthy, C. (2009). Structural Health Monitoring of Anisotropic Plates Using Ultrasonic Guided Wave STMR Array Patches. *NDT & E International*, 193-198.

Bar-Cohen, Y. (2000). Emerging NDE Technologies and Challenges at the Beginning of the Third Millenium. *Materials Evaluation*, 17-30.

Betz, D., Thursby, G., & Staszewski, W. J. (2007). Structural Damage Location with Fiber Bragg Grating Rosettes and Lamb Waves. *Structural Health Monitoring*, 299-308.

Chang, S. F.-K. (2000). Impact identification of stiffened composite panels. *Smart Materials and Structures*.

Chang, S., & Fu-Kyo. (2000). Impact Identification of Stiffened Composite Panels. *Smart Materials and Structures*, 370-379.

Crider, J. S. (2007). Damage Detection Using Lamb Waves for Structural Health Monitoring. Air Force Institute of Technology.

Daniel C. Betz, G. T. (2007). Structural Damage Location with Fiber Bragg Grating Rosettes and Lamb Waves. *Structural health monitoring*, 299-308.

Farrar, C., & Worden, K. (2007). An Introduction to Structural Health monitoring. *Philosophical Transactions of the Royal Society*, 303-315.

Freissinet, S. (2011, October 23). *1001crash*. (Boeing) Retrieved October 12, 2015, from www.1001crash.com: http://www.1001crash.com/index-page-composite-lg-2.html

Fritzen, C. P. (2005). Vibration-Based Structural Health Monitoring - Concepts and Applications. *Key Engineering Materials*, 3-20.

Gangadharan, R., Gopalakrishnan, S., Bhat, M. R., & Murthy, C. R. (2010). A Geodesic-Based Triangulation Technique for Damage location in Metallic and Composite plates. *Smart Materials and Structures*, 115010.

GAO, G. A. (2011). Aviation Safety: Status of FAA's Actions to Oversee the Safety of Composite Airplanes. Report to Congressional Requesters.

Gaso, M. I., March-Iborra, C., Montoya-Baides, Á., & Arnau-Vives, A. (2009). Surface Generated Acoustic Wave Biosensors for the Detection of Pathogens: A Review. *Sensors*, 5740-5769.

Giurgiutiu. (2008). Structural Health Monitoring With Piezoelectric Wafer Active Sensors. Elsevier.

Giurgiutiu, V. (2005). Tuned Lamb Wave Excitation and Detection with Piezoelectric Wafer Active Sensors for Structural Health Monitoring. *Journal of Intelligent Material Systems and Structures*, 291-305.

Giurgiutiu, V., Bao, J., & Zhao, W. (2003). PiezoelectricWafer Active-Sensor Embedded Ultrasonics in Beams and Plates. *Experimental Mechanics*, 428–449.

Guo, H., Xiao, G., Mrad, N., & Yao, J. (2011). Fiber Optic Sensors for Structural Health Monitoring of Air Platforms. *Sensors*, 3687-3705.

Haq, M., Khomenko, A., Udpa, L., & Udpa, S. (2013). Fiber Bragg-Grating Sensor Array for Health Monitoring of Bonded Composite Lap-Joints. *Conference Proceedings of the Society for Experimental Mechanics* (pp. 189-195). Experimental Mechanics of Composite, Hybrid, and Multifunctional Materials.

Harris, C., Starnes Jr., J. H., & Shuart, M. J. (2002). Design and Manufacturing of Aerospace Composite Structures, State-of-the-Art Assesment. *Journal of Aircraft*, 545-560.

Hexcel Corporation. (2013). *HexPly® 8552 Epoxy Matrix.* Hexcel Corporation.

Hunter, G. W., Ross, R. W., Berger, D. E., Lekki, J. D., Mah, R. W., Perey, D. F., . . . Smith, S. W. (2013). *A Concept of Operations for an Integrated Vehicle Health Assurance System.* NASA/TM - 2013-217825: NASA.

Jha, R., & Watkins, R. (2012). A Modified Time Reversal Method for Lamb Wave Based Diagnostics of Composite Structures. *Mechanical Systems and Signal Processing*, 345-354.

Karpenko, O., Koricho, E., Khomenko, A., Dib, G., Haq, M., & Udpa, L. (2014). Multitechnique Monitoring of Fatigue Damage in Adhesively Bonded Composite Lap Joints. *41st Annual Review of Progress in Quantitative Nondestructive Evaluation* (pp. 219-228). Quantitative Nondestructive Evaluation Conference.

Kessler, S., Spearing, M., & Soutis, C. (2002). Damage Detection in Composite Materials Using Lamb Wave Methods. *Smart Materials and Structures*, 269-278.

Keysight, T. (2015, October 5). *BenchVue Software*. Retrieved from Agilent: http://www.keysight.com/en/pc-2472896/benchvue-software?cc=US&lc=eng

Keysight, T. (2015, October 5). *IntuiLink Waveform Editor for Function/Arbitrary Waveform Generators*. Retrieved from www.keysight.com: http://www.keysight.com/main/software.jspx?id=1000000918:epsg:sud&lc=eng&cc=US

Krautkramer. (1998). Emerging Technology – Guided Wave Ultrasonics. *NDTnet*, 3-9.

Krishnan Balasubramaniam, J. V. (2009). Structural health monitoring of anisotropic plates using ultrasonic guided wave STMR array patches . *NDT & E International*, 193-198.

Lamb, H. (1917). On Waves in an Elastic plate. *The Royal Society*, 114-128.

Li, D. S., & Gaitonde, M. (1998). Predicting Strength of Adhesively Bonded Composite Joints. *Science, Technology and Applications* (pp. 69-75). European Conference on Composite Materials.

Lowe, M., & Pavlakovic, B. (2013). *Disperse.*

Michaud, V., Canala, L. P., Sarfarazb, R., Violakisc, G., Botsis, J., & Limberger, H. G. (2014). Monitoring Strain Gradients in Adhesive Composite Joints by Embedded Fiber Bragg Grating Sensors. *Composite Structures*, 241-247.

Micron Optics. (2015, October 5). Retrieved from www.Senginia.com: http://www.sengenia.com/pdfs/sm690.pdf

NDT Resource Center. (2015). Retrieved from www.nde-ed.org

NDT, R. C. (2015). *NDT Resource Center*. Retrieved October 3, 2015, from www.nde-ed.org

Neumair, M. (1998). Requirements on Future Structural Health Monitoring Systems. *Proceedings of the 7th RTO Meetings*.

Ng, K. (1999). Integrated Diagnostics and Prognostics of Rotation Machinery. Office of Naval Research Report.

Nieuwenhuis, J., & Neumann, J. (2005). Generation and Detection of Guided Waves using PZT. *IEEE Trans Ultrasonics, Ferroelectrics and Frequency Control*, 52-63.

Piezo, A. (2015, 9 24). *Ultrasonic Air Transducers.* Retrieved from www.americanpiezo.com: https://www.americanpiezo.com/images/stories/content_images/pdf/apc_10-1011.pdf

Purekar A.S., P. D. (2001). Interrogation of Plate Structures using Phased Array Concepts. *International COnference on Adaptive Structures and Technologies.* University of Maryland.

Purekar, A., & Pines, D. (2001). Interrogation of Plate Structures using Phased Array Concepts. *12th International Conference on Adaptive Structures and Technologies*, (pp. 275-288).

Quaegebeur, N., Micheau, P., & Masson, P. (2011). Structural Health Monitoring of Bonded Composite Joints using Piezoceramics. *Smart Materials, Structures and NDT in Aerospace.* NDT in Canada.

Raspet, F. R. (2015, Oct 4). *Raspet Flight Research Laboratory*. Retrieved from www.raspet.msstate.edu: http://www.raspet.msstate.edu/about/

Reade, L. (2010, January). *A change of heart.* Retrieved from Aero-Mag: http://www.aero-mag.com/_img/pics/pdf_1262963572.pdf

Red, C. (2014, April 9). *Composites World*. (Composites Forecasts and Consulting) Retrieved October 16, 2015, from www.compositesworld.com: http://www.compositesworld.com/blog/23

Rose, J. (1995). Recent Advances in Guided Wave NDE. *IEEE Ultrasonics Symposium*, 761-770.

Rytter, A. (1993). Vibration Based Inspection of Civil Engineering Structures. Ph.D Dissertation. Aalborg University.

Seale, Smith, & Prosser. (1998). Lamb Wave Assessment of Fatigue and thermal Damage in Composites. *Journal of the Acoustical Society of America*, 2416–2424.

Singh, S., & Saha, S. (1984). Electrical Properties of Bone: A Review. *Clinical Orthopedics and Related Research*, 249-271.

Thomson, D., & Chimenti, D. (2002). *Review of Progress in Quantitative Nondestructive Evaluation.* American Institute of Physics.

Tsai, M., Morton, J., & Matthews, F. (1995). Experimental and Numerical Studies of a Laminated Composite Single Lap Joint. *29*, 1254-1275.

Zair, A. B. (2011). Numerical Simulations of Lamb Waves in Plates Using a Semi-Analytical Finite Element Method. Otto-von-Guericke Magdeburg University.

APPENDIX A

MATLAB CODE: GENERATION OF TRIANGULATION AND DAMAGE INDEX PLOTS

A.1 Main Function

```
      %{
      ---------------------------THE MAIN FUNCTION---------------------
------

      The main function accepts the location (dx,dy) of the sensor
relative to the position of the PZT which is assumed to be at the
origin, and the total time of flight (tof) of the wave initiating from
the PZT, travelling and then reflecting off the damage, and then being
sensed by the laser vibrometer.

      The function "vel_theta_fea" accepts the tof and the sensor
position to generate the locus along which damage is predicted to lie.

      The last part of the code is to assign a damage index value to a
grid the size of the composite structure being tested. The damage index
is plotted on a rainbow color distribution chart. All units in S.I.

      %}

      clear
      clc

      %----------------------Inputs for sensory location 1-------------
------

      dy_1=0;
      dx_1=-0.054;
      time_1=.00051;
      [theta1_1,d1_1]=vel_theta_fea(dy_1,dx_1,time_1);
      x_1 = d1_1.*cos(theta1_1);
      y_1 = d1_1.*sin(theta1_1);
      data1 = [x_1.' , y_1.'];
      figure;
      plot(x_1,y_1,'r');
      hold on;
      plot(0,0,'*')
      plot(dx_1,dy_1,'o');



      %----------------------Inputs for sensory location 2-------------
------

      dy_2=-0.04;
      dx_2=0;
      time_2=0.00057;
      [theta1_2,d1_2]=vel_theta_fea(dy_2,dx_2,time_2);
      x_2 = d1_2.*cos(theta1_2);
      y_2 = d1_2.*sin(theta1_2);
      data2 = [x_2.' , y_2.'];
      plot(x_2,y_2,'k');
```

```
      plot(dx_2,dy_2,'o');



      %----------------------Inputs for sensory location 3-------------
------

      dy_3=0.035;
      dx_3=0;
      time_3=0.00057;
      [theta1_3,d1_3]=vel_theta_fea(dy_3,dx_3,time_3);
      x_3 = d1_3.*cos(theta1_3);
      y_3 = d1_3.*sin(theta1_3);
      data3 = [x_3.' , y_3.'];
      plot(x_3,y_3,'b');
      plot(dx_3,dy_3,'o');
      line([0.2,-0.2],[0.04,0.04]);
      line([0.2,-0.2],[-0.04,-0.04]);
      axis equal tight
      plot (-0.27,0,'*')


      %{
      --------------------Generation of the Damage Index grid----------
------------------------------------------------------------------------
------

      The grid has the same dimensions as the composite structure
      %}

      x=linspace(-0.4,0.03,1000);
      y=linspace(-0.06,0.06,1000);


      for i=1:1000
          for k=1:1000
              xcoord = x(i);
              ycoord = y(k);
              min_d1 = 1;
              min_d2 = 1;
              min_d3 = 1;
              for j=1:100
                  dist1 = sqrt((xcoord-x_1(j))^2 + (ycoord-y_1(j))^2);
                  dist2 = sqrt((xcoord-x_2(j))^2 + (ycoord-y_2(j))^2);
                  dist3 = sqrt((xcoord-x_3(j))^2 + (ycoord-y_3(j))^2);
                  if dist1 < min_d1
                      min_d1=dist1;
                  end
                  if dist2 < min_d2
                      min_d2=dist2;
                  end
                  if dist3 < min_d3
                      min_d3=dist3;
```

```
                  end
                  DI_T(i,k) = min_d1+min_d2+min_d3;
              end
          end
      end

      %-----------Calibration of the DI value to increase contrast-----
------

      DI = DI_T.';
      min_DI = min(min(DI));
      for i=1:1000
          for j=1:1000
              if DI(i,j)>1.3*min_DI
                  DI(i,j) = 1.3*min_DI;
              end
          end
      end



      %--------------------------Plotting the DI chart-----------------
------

      xrep = repmat(x,1000,1);
      yrep = repmat(y.',1,1000);
      figure;
      colormap(flipud(colormap))
      pcolor(xrep,yrep,DI);
      shading interp;
      hold on
      plot(0.127,0,'r*','MarkerSize',12)

      axis equal tight
      plot(0,0,'r*')

      plot(dx_1,dy_1,'ro');
      plot(dx_2,dy_2,'ro');
      plot(dx_3,dy_3,'ro');

      line([-0.05 -0.05],[-0.04 0.04],'Color','r');
      line([-0.105 -0.105],[-0.04 0.04],'Color','r');
```

A.2 Function to Generate the Damage Location Locus for each Sensory Location

```
      %{
      -------------------Function: vel_theta_fea-----------------------
------
      -----------------------------------------------------------------
------

      This function is used to generate the damage location locus. The
slowness properties in this case have been generated using ABAQUS and
validated using Disperse. All units in S.I.

      %}


      function [theta1fin, d1fin] = vel_theta_fea(dy,dx,t)


      theta1 = [0 14.8 30 41.2116 44.93 52.82 63.14 74.55 81.464
90].*pi/180;
      diff = pi/2 - theta1;
      theta2 =pi/2 + fliplr(diff);
      theta3 = pi + theta1;
      theta4 = 3*pi/2 + fliplr(diff);
      V651 = [ 988.0240  849.0030  668.5105  648.8698  642.9256
655.4051  670.0435  777.7651  860.0412  873.0159 ];
      V652 = fliplr(V651);
      V653 = V651;
      V654 = V652;

      p1=polyfit(theta1,V651,5);
      p2=polyfit(theta2,V652,5);
      p3=polyfit(theta3,V653,5);
      p4=polyfit(theta4,V654,5);

      thet1 = linspace(0,2*pi);

      for i=1:100
          if thet1(i)>=0 && thet1(i) <= pi/2
              V1 = polyval(p1,thet1(i));
          elseif thet1(i)>pi/2 && thet1(i)<=pi
              V1 = polyval(p2,thet1(i));
          elseif thet1(i)>pi && thet1(i)<=1.5*pi
              V1 = polyval(p3,thet1(i));
          elseif thet1(i)>1.5*pi && thet1(i)<=2*pi
              V1 = polyval(p4,thet1(i));
          end

          min_val_d2(i)=1;
          for j=0:10000
              d1=j/10000;
              t1=d1/V1;
              t2=t-t1;
```

```
        xcoord = d1*cos(thet1(i));
        ycoord = d1*sin(thet1(i));
        slope = (dy-ycoord)/(dx-xcoord);
        dist = sqrt((dy-ycoord)^2 + (dx-xcoord)^2);
        thet2 = atan(slope);

        if thet2<0;
            thet2 = thet2 + 2*pi;
        end

        if thet2 >= 0 && thet2 <= pi/2
            V2 = polyval(p1,thet2);
        elseif thet2 > pi/2 && thet2 <= pi
            V2 = polyval(p2,thet2);
        elseif thet2 > pi && thet2 <= 1.5*pi
            V2 = polyval(p3,thet2);
        elseif thet2 > 1.5*pi && thet2 <= 2*pi
            V2 = polyval(p4,thet2);
        end
        d2 = V2*t2;
        if abs(dist-d2) < min_val_d2(i)
            min_val_d2(i) = abs(dist-d2);
            min_val_d1(i) = d1;
        end
    end
end
theta1fin = thet1;
d1fin = min_val_d1;
end
```

APPENDIX B

MATLAB CODE: GENERATION OF USER-DEFINED TONE BURST WAVEFORM

```
      %{
      ---------------------------TONE BURST GENERATION-----------------
------

      The function uses the user-defined frequency and desired number
of wavelengths in the tone bursts to generate the desired waveform. All
units in S.I.

      %}

      clear
      clc

      %---------------------------Inputs-------------------------------
------

      freq = 65000;
      tone = 5.5;

      %----------------------------------------------------------------
------

      y = sin(2*pi*freq*(0:1e3)*1e-6);
      figure;
      time = (linspace(0,10^-3,1001))';
      plot((0:200)*1e-6,y(1:201),'k');
      title('65 khz Sinusoidal
Waveform','FontWeight','bold','FontSize',20)
      xlabel('Time(s)','FontWeight','bold','FontSize',15)
      ylabel('Normalized Amplitude ','FontWeight','bold','FontSize',15)
      no_of_waves = freq/1000;
      no_of_points = ceil(tone*1000/no_of_waves);
      x = [hann(no_of_points);zeros(1001-no_of_points,1)];
      figure;
      plot(x(1:100),'k')
      title('Hanning Window','FontWeight','bold','FontSize',20)
      xlabel('Time(s)','FontWeight','bold','FontSize',15)
      ylabel('Normalized Amplitude ','FontWeight','bold','FontSize',15)
      figure;
      temp = y.*x';
      plot((0:300)*1e-6,temp(1:301),'k')
      h=y.*x';
      ht=h';
      title('5.5 Wave Tone Burst','FontWeight','bold','FontSize',30)
      xlabel('Time(s)','FontWeight','bold','FontSize',23)
      ylabel('Normalized Amplitude ','FontWeight','bold','FontSize',23)


      %-------------------------Output: Desired Waveform---------------
------
      waveform = [ht time];
```